NTNU – Trondheim
Norwegian University of
Science and Technology

Cellular Interaction with Polymeric Nanoparticles: The Effect of PEGylation and Monomer Composition

Sara Westrøm

Nanotechnology
Submission date: June 2013
Supervisor: Catharina de Lange Davies, IFY

Norwegian University of Science and Technology
Department of Physics

Abstract

It is of importance to understand which nanoparticle properties that govern the interactions between particles and cells, in order to develop a nanocarrier with the desired functionality. In this thesis, nanoparticles made of biodegradable poly(alkyl cyanoacrylate), with either butyl or octyl as the side chain, and with different polyethylene glycol (PEG) surface coatings, have been utilized. The objective was to determine whether variations in these properties influenced cellular uptake and toxicity in prostatic adenocarcinoma cells, as well as the release of a model drug, nile red.

Cellular uptake of nanoparticles was investigated *in vitro* using flow cytometry and confocal laser scanning microscopy. It was established that the encapsulated nile red marker could dissociate from the particles, thus making evaluation of cellular uptake difficult. No alterations in PEG type or chain lengths made nile red remain in the particles to such a degree that endocytosis of nanoparticles could be detected. Spectrophotometric analyses of nile red release from the nanoparticles and into cell medium demonstrated that $\sim$45% or more of originally encapsulated nile red was released after 3 hours. This confirmed high nile red release from the particles, and at the same time it showed that changes in PEGylation did not reduce the release to any extent. After estimating PEG chain surface densities, it was evident that all particles had very low PEG densities, providing an explanation to why nile red dissociated from the particles to such a high degree: the PEG layer did not shield a large enough part of the particle surface area to effectively hinder release of nile red.

Cytotoxicity after nanoparticle exposure was determined using an assay measuring the metabolic activity of cells. Toxicity was found to be strongly dependent on the length of the alkyl side chain in the monomer, where the longest chain, with the lowest degradation rate, was the least toxic. Altogether, this suggests toxicity induced by release of degradation products, but it can also be attributed to residual surfactant from the synthesis, as the observed cytotoxicity was higher than what is reported in literature for similar nanoparticles.

Sammendrag

Det er svært viktig å forstå hvilke egenskaper ved nanopartikler som styrer interaksjonene mellom partikler og celler for å utvikle en partikkel med ønsket funksjonalitet. I denne masteroppgaven har nanopartikler laget av biodegraderbar poly(alkyl cyanoakrylat), med enten butyl eller oktyl som sidekjede, og med ulike polyetylen glykol (PEG) lag på overflaten, blitt benyttet. Målsetningen var å bestemme hvorvidt variasjoner i disse egenskapene påvirket opptak og toksisitet i prostatiske adenocarcinom celler, i tillegg til frigjøring av en modell cytostatika, nilrød.

Opptak av nanopartikler i celler ble undersøkt *in vitro* ved hjelp av flow cytometri og konfokal laser skanning mikroskopi. Det ble fastslått at innkapslet nilrødt kunne dissosiere fra partiklene og dette gjorde evalueringen av cellulært opptak vanskelig. Ingen endringer i PEG type eller PEG kjedelengde resulterte i at nilrød forble i partiklene i stor nok grad til at endocytose av nanopartiklene kunne detekteres. Spektrofotometriske målinger av nilrødt frigjort fra nanopartiklene i cellemedium påviste at $\sim$45% eller mer av den opprinnelige mengden nilrødt innkapslet i partiklene kunne frigjøres i løpet av 3 timer. Dette bekreftet høy nilrød frigjøring fra partiklene, samtidig som det viste at endringer i PEGylering ikke påvirket frigjøringen i noen grad. Etter å ha estimert overflatetettheten av PEG kjeder ble det tydelig at alle partiklene hadde svært lave PEG tettheter, noe som ga en forklaring på hvorfor nilrød dissosierte fra partiklene i så stor grad: PEG laget beskyttet ikke en stor nok del av partikkeloverflaten for å effektivt hindre frigjøring av nilrødt.

Cytotoksisitet etter nanopartikkel eksponering ble bestemt ved å bruke et assay som målte cellenes metabolske aktivitet. Toksisiteten var svært avhengig av lengden på alkyl sidekjeden i monomeren, der den lengste kjeden, med lavest degraderingshastighet, var den minst toksiske. Alt i alt tydet dette på at toksisiteten var forårsaket av frigjøring av degraderingsprodukter, men den kan også skyldes gjenværende surfaktant fra syntesen, siden den observerte cytotoksisiteten var høyere enn det som er beskrevet i litteraturen for lignende nanopartikler.

Preface

This master's thesis marks the final part of a 5 year Master of Science program in Nanotechnology at the Norwegian University of Science and Technology. I have chosen to specialize in bionanotechnology, and the work with this thesis was performed at the Department of Physics, spring 2013, under the supervision of professor Catharina de Lange Davies.

First of all, I would like thank my supervisor, professor Catharina de Lange Davies, for giving me the opportunity to work on a project concerning nanoparticle mediated drug delivery in cancer therapy, a field of biomedical research that has interested me ever since I started my education. I want to express my gratitude for how she has shared her superior knowledge in this field with me, and for all help, guidance and encouragement she has provided throughout the semester. Further, a special thanks goes to postdoc Ýrr Mørch for always taking her time to discuss experiments and results, and as well providing invaluable insight into the nanoparticle properties and synthesis procedure. I also wish to thank postdoc Andreas Åslund, who on all occasions contribute with interesting ideas and suggestions to new strategies.

Anne Rein Hatletveit and Sidsel Sundseth, both technicians at SINTEF Materials and Chemistry, deserve recognition for synthesizing and characterizing the nanoparticles used in the experiments, and for being smiling and positive at all times. Anne has also spent her time helping me out with spectrophotometric measurements. I am also grateful for the sincere interest from Kristin Grendstad Sæterbø, and how she is always available to answer any questions I might have regarding cell and general laboratory work. Furthermore I would like to thank Astrid Bjørkøy for training and technical assistance with the confocal laser scanning microscope, ph.d student Kai M. Beckwith for help with the plate reader and Gjertrud Maurstad for assistance with the Avanti centrifuge. Last, but not least, I want to state how important fellow master student Sofie Snipstad has been in the work with this thesis. I have enjoyed and benefited from our continuous discussions on all subjects ranging from writing, experiment planning and analysis of results.

Sara Westrøm
Trondheim, June 2013

Contents

List of abbreviations

CT	Computed tomography
CLSM	Confocal laser scanning microscopy
EPR	Enhanced permeability and retention
FBS	Fetal bovine serum
FCM	Flow cytometry
FDA	U.S. Food and Drug Administration
MFI	Median fluorescence intensity
MPS	Mononuclear phagocyte system
MRI	Magnetic resonance imaging
NMR	Nuclear magnetic resonance
PBCA	Poly(butyl cyanoacrylate)
PBS	Phosphate buffered saline
PEG	Polyethylene glycol
POCA	Poly(octyl cyanoacrylate)
SDS	Sodium dodecyl sulfate
THF	Tetrahydrofuran

1 Introduction

Cancer is a group of diseases characterized by uncontrolled and abnormal cell proliferation and metastasis. None of the existing therapies (surgery, radiation and chemotherapy) have been able to prevent an increase in number of cancer deaths during the past 70 years [1], and with more than 12 million new cases occurring every year [2], cancer remains one of the world's most devastating diseases. Additionally, administration of chemotherapeutic drugs cause severe side effects in patients and can also damage healthy tissue. [3] This calls for the development of new methods for improved cancer diagnosis and treatment.

General progress in the field of nanotechnology has given a continuous increase in understanding the potential that comes from using nanoparticles in biomedical applications. [4] Nanocarriers, which can be loaded with a contrast agent [5], anticancer drug [6] or both [7], are developed to create safer and more effective therapeutic and diagnostic modalities. The nanoparticles can have unique physical and biological properties, carefully designed to overcome current limitations with molecular imaging and drug delivery to tumors. Such nanoparticle systems hold considerable promise as the next generation cancer medicine that enable early detection, delivery of targeted therapy, monitoring of therapeutic response and minimization of adverse effects. [8, 9, 10]

The work with this master's thesis has been carried out as a part of a collaboration project between NTNU, SINTEF and St. Olavs Hospital called "Multifunctional nanoparticles in cancer diagnosis and therapy". SINTEF Materials and Chemistry has developed a one-step synthesis route for poly(alkyl cyanoacrylate) nanoparticles which are intended for use as carriers of therapeutic and/or contrast agent. The novelty with these nanoparticles is their ability to stabilize microbubbles. Together with applied ultrasound, the microbubbles can function as contrast agents in ultrasound imaging, and at the same time improve drug delivery by enhancing the transport across vasculature and into cancerous tissue. The prospective goal is to achieve a multifunctional nanoparticle system that can be used for simultaneous monitoring and treatment of cancer.

To develop a nanocarrier with properties that can fulfill this goal, it is crucial to understand the interactions between nanoparticles and cells. Many pharmacological targets are located intracellularly [11], and consequently such drugs must be taken up by cancer cells for the delivery to be successful. This is possible either by endocytosis of the nanomedicine and subsequent intracellular release, or extracellular release followed by drug diffusion across the cell membrane. Both these processes will depend on interactions at the nanoparticle-cell interface. Additionally, other important features of nanoparticle systems are influenced by these interactions,

e.g. cytotoxicity and circulation times. Research suggests that the interactions at the nano-cell interface mainly are affected by the size and surface properties of the particles. [12, 13, 14] One common way of altering surface properties is to coat the nanoparticle with polyethylene glycol (PEG). [15, 16] An increased understanding on how different nanoparticle properties influence their interactions with cells can eventually result in much needed knowledge on how to design a nanocarrier with the desired characteristics.

In my project work "Investigation of cellular uptake of PBCA nanoparticles" [17], the results clearly indicated that interactions at the particle-cell interface were affecting cellular uptake of a lipophilic, fluorescent probe: nile red. It was established that the transfer of nile red from nanoparticles into cells was mainly driven by diffusion, and the process was hypothesized to stem from collisions between particles and the cell membrane. Based on this discovery, it was seen as important to learn more about how the poly(alkyl cyanoacrylate) nanoparticles are interacting with cells. Therefore, in this thesis, the effect of nanoparticle properties on cellular uptake, hydrophobic probe release and cell viability have been investigated, with emphasis on the influence of PEGylation and monomer composition. The utilized nanoparticles have been coated with PEG chains of different type and length, and prepared from two monomers with different side chain lengths: butyl- and octyl cyanoacrylate. In addition, since partition of nile red from the nanoparticles complicated the analysis of cellular uptake in the project work, nanoparticles labeled with different fluorescent markers have been tested and evaluated as a part of this study.

2 Theory

2.1 Nanoparticle applications in medicine

A wide variety of nanoparticle systems intended for use in the medical field are under development today. Nanoparticles for medical applications are defined as particles with a size between 1 and 1000 nm [18], and thereby they offer the possibility to interact with and influence cellular entities and processes at their natural scale. These biomimetic features, together with high surface to mass ratio and ease of introducing new properties or modifying already existing properties, give nanoparticle systems the potential of bringing significant advances in the prevention, diagnosis and treatment of disease. Nanoparticle systems are therefore being exploited in diverse medical applications such as imaging, drug and gene delivery, photothermal therapy and biosensors. The constant increasing interest for nanoparticles in medicine has made the need for a common term for these applications evident. Nanomedicines are thus defined as the use of nanoscale or nanostructured materials that according to their structure have unique medical effects in both diagnosis and treatment of disease. [19] Examples of nanoparticle platforms investigated for biomedical purposes include polymeric, ceramic, magnetic, solid-lipid and viral-based nanoparticles, liposomes, micelles, dendrimers and carbon nanotubes [20, 21], where some are depicted in figure 2.1.

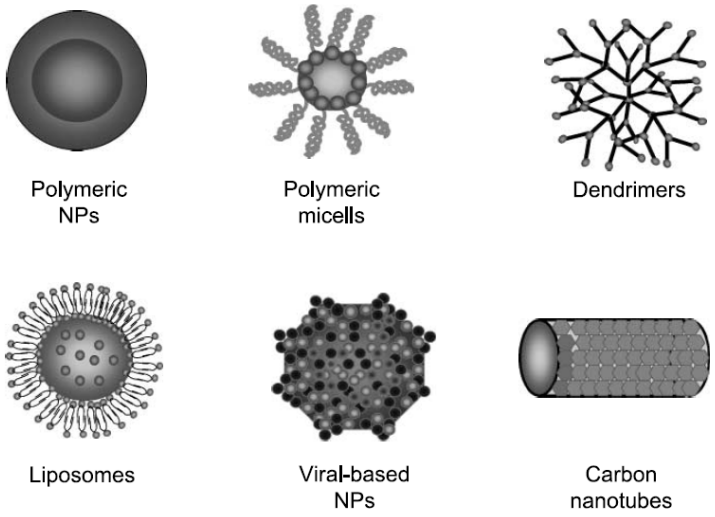

Figure 2.1: An illustration showing some nanoparticle systems commonly used in medical applications. [20]

The first generation of nanomedicines have already been approved by the U.S. Food and Drug Administration (FDA), and are available on the market. In fact, if polymer therapeutics (i.e. polymer-drug conjugates) are included, more than 40 products have completed the translation from laboratory to clinical use. [22] In table 2.1, a representative selection of FDA approved nanomedicines is given. From this overview it is worth to note that significantly more nanomedicines have entered routine clinical practice for therapeutics than for imaging.

Table 2.1: Examples of FDA approved nanomedicines. [22, 23]

Product name	**Technology**	**Indication**	**Approval**
Abelcet	Liposomal amphotericin B	Fungal infections	1995
Abraxane	Albumin-paclitaxel nanoparticles	Metastatic breast cancer	2005
Cimzia	PEGylated fragment of an anti-TNF antibody	Crohn's disease and rheumatoid arthritis	2008
Copaxone	Glutamine, Alanine, Tyrosine copolymer	Multiple sclerosis	1996
DaunoXome	Liposomal daunorubicin	HIV-associated Kaposi's sarcoma	1996
Depocyt	Liposomal cytosine arabinoside	Cancer	1999
Doxil/Caelyx	PEGylated liposomal doxorubicin	Various cancer types	1995
Emend	Nanocrystal particles	Chemotherapy related nausea and vomiting	2003
Gastromark	Silicon-coated SPIONs	MRI contrast agent	1996
MultiHance	Gadolinium-based nanoparticles	MRI contrast agent	2004
Pegasys	PEG-interferon alpha	Hepatitis B and C	2002
Visudyne	Liposomal verteporfin	Age-related macular degeneration	2000

Abbreviations: Superparamagnetic iron oxide imaging nanoparticles (SPIONs)

2.1.1 Nanoparticles as drug delivery systems

Drug delivery mediated by nanoparticles is an intriguing field of research that has captured the interest of scientists worldwide. This is illustrated by how around 75% of all scientific publications within the field of nanomedicines center around this topic. [19] The development of effective drug delivery systems that can transport and deliver a drug precisely and safely to its site of action is the motivation behind this massive research effort. A safe and targeted drug delivery can improve the performance of some traditional drugs already on the market, and furthermore contribute to the development of novel therapeutic strategies such as peptide and protein delivery, glycoprotein administration, gene therapy and RNA interference. [24]

A nanoparticle drug delivery system is made by encapsulating or attaching a therapeutic agent to a nanoparticle platform. (See figure 2.1 for examples of nanocarriers.) These systems offer potential solutions for current challenges in treating cancer, cardiovascular and neurodegenerative diseases, in addition to several other illnesses. [23] The aim with nanoparticle drug delivery systems is to administer the drug through controlled delivery, such that an optimum amount reaches the target site, resulting in increased efficacy of treatment and maximized patient compliance. In addition, these systems can provide new opportunities with drugs that were rendered useless because of high toxicity, high dosage requirements, poor solubility and short circulation times *in vivo*. Table 2.2 summarizes some of the achievable advantages with nanoparticle drug delivery systems.

Table 2.2: Advantages with nanoparticle drug delivery systems. [21, 25, 26]

- Provide targeted delivery
- Improve bioavailability
- Decrease toxic side effects
- Protect the drug from degradation
- Increase the aqueous solubility of the drug
- Reduce total body dose of drugs
- Simultaneously deliver multiple drugs
- Improve crossing of biological barriers
- Produce a prolonged release of drugs
- Offer appropriate form for all routes of administration

The most notable advances in nanoparticle mediated drug delivery have been in the field of oncology. [27] This can be illustrated by how several products in the anticancer segment have been FDA approved. Doxil®/Caelyx® and Abraxane® (see table 2.1) are two main examples of drug delivery nanocarriers with success in the clinic. The chemotherapeutic agents doxorubicin and paclitaxel are both very effective in killing cancer cells, but their use is limited when administered alone because of severe side effects. When these drugs are associated with their respective nanocarrier (doxorubicin encapsulated in liposomes and paclitaxel associated with albumin nanoparticles) patients experience lower systemic toxicity and can benefit from improved therapeutic efficacy. [28, 29, 30, 31] More details about nanomedicines in cancer therapy will follow in section 2.3.

2.1.2 Nanoparticle systems as contrast agents in imaging

For many of the same reasons that nanoparticles are utilized as drug carriers, their unique features are being exploited as contrast agents in biomedical imaging. The use of contrast agents are standard practice in such imaging since they are necessary to achieve adequate image quality. [32] Contrast agents function to enhance image contrast and improve the visibility of features that otherwise would be difficult to detect. Ultrasound, magnetic resonance imaging (MRI), X-ray and computed tomography (CT) are examples of non-invasive imaging modalities that can benefit from the development of nanoparticle contrast agents.

The prospective goal with improving existing imaging techniques by utilizing nanoparticle contrast agents, is to develop diagnostic procedures to image pathogenic processes on a molecular level. [18] Such molecular diagnostics might be essential both for early diagnosis and understanding the underlying processes of many diseases. Areas where nanoparticle contrast agents can be advantageous include imaging for guided surgery, imaging of gene expression *in vivo* to elucidate disease development, and monitoring of drug efficacy. [33] In addition, the ability to image and track the fate of a nanomedicine *in vivo* will be of great importance in the development of effective drug delivery systems.

A nanoparticle contrast agent is made by loading of a contrast enhancing agent into a nanocarrier, or the nanoparticles can function as contrast agents themselves. Table 2.3 gives some examples of nanoparticle systems utilizing different contrast mechanisms, according to which imaging modality they are intended for. Compared with conventional molecular-scale contrast agents, nanoparticle systems offer the possibility of targeting to sites of interest and increased circulation times allowing for prolonged imaging. As of today, only nanoparticle based contrast agents for MRI imaging have been approved for clinical use. (See table 2.1)

Table 2.3: Nanoparticle systems for various imaging techniques

- Gold nanoparticles as X-ray contrast agent. [34]
- Magnetic nanoparticles as MRI contrast agent. [35]
- Microbubbles with immobilized nanoparticles on the surface as ultrasound contrast agent. [36]
- Quantum dots as optical labels in fluorescence imaging. [37]
- Radiolabeled nanoparticles for positron emission tomography and single-photon emission CT. [38]

2.1.3 Multifunctional nanoparticles

The applications described above demonstrate how nanoparticle systems have great potential in prevention, detection and treatment of disease. From this knowledge, new technology combining these properties is emerging. Whereas monofunctional nanoparticle systems provide a single function, multifunctional nanoparticles are engineered to have different functionalities in one construct. Multifunctional nanoparticles that can target, monitor and treat the site of disease simultaneously are being exploited. A potential multifunctional nanoparticle system is illustrated in figure 2.2. Here, the nanoparticles are functionalized with a targeting ligand, and loaded with MRI contrast agent and therapeutic agent. The particles are thus multifunctional; they offer possibilities for targeting to a diseased site, enhanced contrast with MRI imaging and drug delivery. In addition, the nanoparticles can be immobilized on the surface of microbubbles and in this manner allow ultrasound imaging with improved contrast. By using a construct that contain both therapeutic and contrast agent, the distribution and effect of drugs can be monitored *in vivo*. Such platforms, where disease diagnosis and therapy are combined, are generally referred to as theranostic nanoparticles. [39]

A summary of the different properties it is possible to incorporate in a multifunctional nanoparticle system is given in table 2.4. Production of nanoparticle systems that contain some or all of the mentioned properties remains a challenge, and one of the limitations is the surface chemistry required. [40] Adding multiple functions on a single particle usually means additional synthesis steps and costs, and the realization of such systems is clearly dependent on advances in chemical techniques. Moreover, a multifunctional nanoparticle system will have more complex effects and behavior *in vivo*, and also greater regulatory hurdles. The trade-off between additional functionality and complexity is the subject of ongoing debate. It is

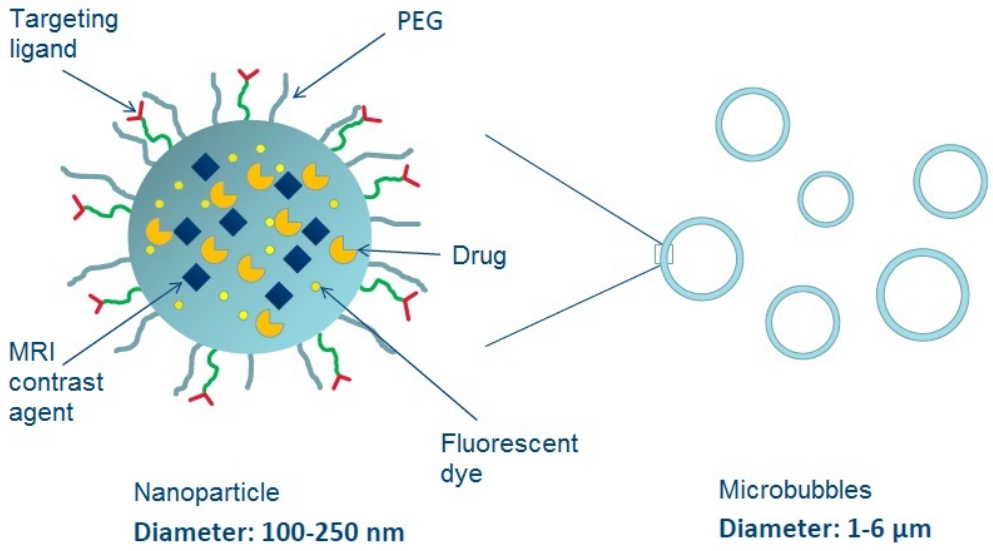

Figure 2.2: An illustration showing a potential multifunctional nanoparticle system which combines possibilities of imaging and drug delivery. The nanoparticles on the left have a targeting ligand on the surface and are incorporated with a drug and MRI contrast agent. On the right, the same nanoparticles are attached to the surface of microbubbles which can be utilized as contrast agents in ultrasound imaging. Figure adapted from Ýrr Mørch, SINTEF Materials and Chemistry.

Table 2.4: A summary of different properties it is possible to incorporate in a multifunctional nanoparticle system. [40]

Property	**Functions**
Therapeutic agent	Released to treat diseased site.
Targeting ligand	Recognizes target cells to increase efficiency and reduce toxicity of therapeutic agent.
Imaging agent	Report real-time nanoparticle distribution and monitor drug transport such that therapeutic efficacy of drugs can be evaluated.
Cell-penetrating agent	Facilitate entry of nanoparticle systems into cells. Can modify nanoparticle pharmacokinetics and biodistribution, and increase drug efficacy.
Stimulus sensitive agent	Responds to stimulus to release encapsulated agents. Controls bioavailability and reduces toxicity of drugs.

claimed that addition of targeting ligands and imaging capabilities to therapeutic nanoparticles is worth the additional complexity of synthesis, cost and regulatory hurdles. [41]

2.1.4 PEGylation of nanoparticles

Parts of this section are taken from my project work. [17]

No matter which function a nanoparticle system is intended to have, one feature will be in common; it needs to be able to maintain in the body for a long enough time to reach its site of action. A significant obstacle to the long-term circulation of nanoparticles, is clearance by the mononuclear phagocyte system (MPS). When nanoparticles are employed in the body, plasma proteins adsorb on the particle surface, targeting the carrier for elimination. Phagocytic cells in blood and tissue can then recognize the nanoparticles as foreign material, engulf them and transport them to the liver and spleen for degradation and excretion. The MPS has the ability to clear intravenously administered nanocarriers from the blood within minutes. [42] Therefore, nanoparticles developed for systemic application need to be engineered to avoid elimination by the MPS.

Unquestionably, the most successful approach to impart stealth properties on nanoparticles, is coating the particle surface with a PEG layer. PEG is a coiled, hydrophilic polyether compound that can be covalently attached, adsorbed or grafted to the surface of a nanoparticle. Addition of a PEG coating to the nanoparticle surface reduces MPS uptake and increases circulation time when compared to uncoated particles. [16] This is mainly because PEG has the lowest level of protein or cellular adsorption of any known polymer [43], thus making a nanoparticle coated with PEG unrecognizable for the plasma proteins in the blood stream. The circulation half-life of liposomes has been extended to more than 60 hours by PEGylation. [44]

The most acknowledged theory to explain why PEG improves stealth properties of nanoparticles is based on interactions between proteins and the PEGylated surfaces. When plasma proteins in the blood stream approach the particles, they will compress the surface layer of PEG chains. Upon compression, the PEG layer is forced into a higher energy conformation, which will create an opposing force. This force can completely balance and/or overpower the attractive force between the plasma proteins and the particle, resulting in less or no attachment of proteins to the surface. [45] For this process to be effective, the PEG layer must exceed a minimum thickness. The thickness can be hard to control and is therefore usually put in connection with factors like PEG chain molecular weight and surface density.

Most research indicates that a PEG chain molecular weight of 2000 Da or greater is required to achieve decreased uptake by the MPS [45], meaning this molecular weight is believed to give a PEG layer exceeding the minimum thickness needed.

Depending on the PEG density, there are two main surface conformations the PEG layer can take. If the surface coverage is low, the PEG chains will usually take on a "mushroom" formation, whereas high surface coverage leads to a "brush" configuration. The two conformations are illustrated in figure 2.3. PEG chains in a mushroom formation will on average be located close to the particle surface, while in the brush formation the chains will extend from the particle surface. A high surface density will make sure that no gaps in the PEG layer are present (occurs with too low density), but on the other hand, it will lead to restricted mobility and thus reduced steric hindrance properties of the PEG layer. Hence, theoretically, the optimal surface coverage will lie somewhere in between that of the mushroom and brush configuration. [45] It is also reported in literature that nanoparticles with an intermediate mushroom/brush configuration were most resistant to phagocytosis and activated the human complement system poorly. [46]

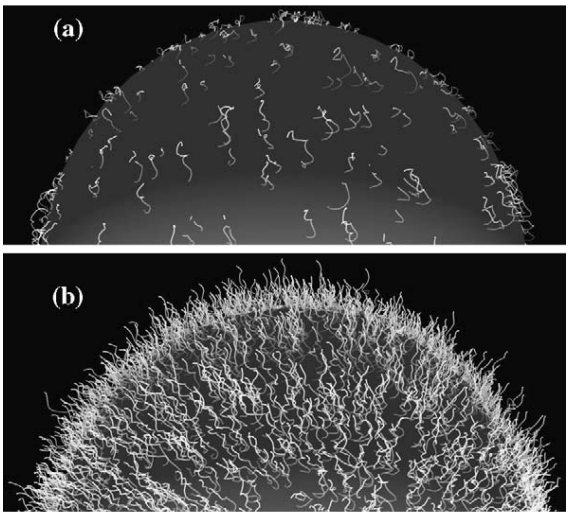

Figure 2.3: Schematic diagram showing the PEG layer conformation on a nanoparticle surface. (a) shows a nanoparticle with low density of PEG, thus resulting in a PEG layer in a "mushroom" conformation, and (b) illustrates a nanoparticle with high surface density of PEG leading to a "brush" conformation. [45]

Attention has to be made that PEGylation of nanoparticles is not exclusively positive. Nanoparticle systems are dependent on efficient delivery of their contents when they reach the target site. The PEG coating may be an obstacle in realizing desired therapeutic response by hindering delivery of therapeutic agent and/or interfering with target cell interaction. [47] The first effect has been demonstrated by showing how PEG coating of nanoparticles compromises intracellular delivery of genes. [48] In a recent article, it was observed that high PEG surface density on nanoemulsions decreased the efficacy of targeting to angiogenic tumor vasculature [49], providing evidence for the second unfavorable effect. Besides this, immune reactions to PEGylated liposomes have also been reported. [50, 51]

2.2 Polymeric nanoparticles

After being extensively studied, polymeric nanoparticles for biomedical applications are today in various stages of research. Since polymer chemistry is a versatile field, the particles can be manufactured from a wide range of polymers, both synthetic and natural in origin. The selected polymers must fulfill several requirements, like biocompatibility with tissue and cells, controlled- and sustained release properties, suitable degradation kinetics and mechanical properties and ease of processing. [52, 53] In general, synthetic polymers have the advantage of a sustained release of therapeutic agent over a period of days to several weeks when compared to natural polymers with a relatively shorter duration of release. [54] On the other hand, their application *in vivo* can be limited by the use of organic solvents and harsh conditions during preparation. Table 2.5 gives a summary of the most common polymers used in the manufacture of nanoparticles for medical purposes.

In the past decades there has been considerable interest in developing biodegradable nanoparticles for applications in the medical field. The use of biodegradable materials ensure that the polymer is degraded *in vivo* through either simple chemical reactions or enzyme-catalyzed reactions. [56] To assure that the polymer is also eliminated from the body without residual side effects, biodegradability is not enough; the polymer needs to be resorbable as well. The degradation byproducts from bioresorbable polymers can be eliminated through natural pathways, either by simple filtration or after being metabolized. [57] One class of such bioresorbable polymers is the poly(alkyl cyanoacrylates). They have been investigated for fabrication of biomedical nanoparticles for more than 20 years [58], and the interest has not decreased by seeing how poly(isohexyl cyanoacrylate) nanoparticles loaded with doxorubicin (Transdrug®) for treatment of advanced hepatocellular carcinoma reached phase III clinical trials in 2012. (Clinical trial ID: NCT01655693)

Table 2.5: An overview of the most frequently used polymers in the fabrication of nanoparticles for biomedical applications. [55]

Synthetic polymers	**Natural polymers**
Polyesters	Proteins
• Polylactides	• Albumin
• Poly(ϵ -caprolactone)	• Collagen
• Poly(phosphoesters)	Polysaccharides
• Poly(ortho esters)	• Cellulose
Polyanhydrides	• Alginate
Polyphosphazenes	• Chitosan
Poly(alkyl cyanoacrylate)	• Pullulan and dextran
	• Hyaluronic acid
	• Ulvan
	Polyhydroxyalkanoates

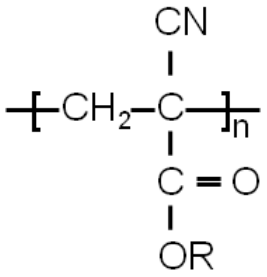

Figure 2.4: Chemical structure of poly(alkyl cyanoacrylates), where R denotes the alkyl group and n the number of repeating units.

In vivo, poly(alkyl cyanoacrylate) nanoparticles undergo surface degradation. The main pathway is by hydrolysis of the ester bond on the alkyl side chain of the polymer [59, 60], and the rate of degradation has been shown to decrease with increasing length of the alkyl side chain. [61] A representation of the chemical structure of the polymer is given in figure 2.4. Esterases from serum seem to be important for catalyzing the hydrolysis reaction [62], and the generated byproducts, alkylalcohol and poly(cyanoacrylic acid), are eliminated through kidney filtration. [63] Even if the polymer is classified as bioresorbable, it is important to note that the complete removal of polymeric material only occurs if the nanoparticles are prepared from low molecular weight polymers. [55]

2.2.1 Toxicity of biodegradable polymeric nanoparticles

The three main outcomes of cellular toxicity are cell death, genotoxicity and inflammation. Assessment of possible toxicity after exposure to polymeric nanoparticles is therefore a critical factor to consider when evaluating their potential in biomedical applications. It is believed that the toxic potential of nanoparticles are due to the chemical composition of the parent material, interactions at the nanoparticle-biological interface, or a combination of both.

To avoid adverse effects of biodegradable polymeric nanoparticles it is important to ensure that the composition of the polymer is not toxic by itself, and what cellular responses are induced by degraded particles. After administration of a nanomedicine, the intact polymeric structure will after a time start to degrade. This process results in potentially hazardous polymeric residues and degradation products of different sizes being exposed to the biological environment. Biodegraded nanoparticles may cause harm by accumulating within cells and thereby leading to intracellular changes such as disruption of organelle integrity or gene alterations. [64] The degree of toxicity is influenced by the degradation rate of the nanoparticles, which again is dependent on the composition of the particle and the biological conditions of the local environment. [65] One example is poly(alkyl cyanoacrylate) nanoparticles, where several studies have demonstrated how cytotoxicity clearly depends upon the degradation rate of the polymer. [66, 67]

Polymeric nanoparticles for medical purposes are designed to deliberately interact with cells and tissue. This pose a risk since the interactions themselves can cause adverse effects. When a nanomedicine is administered in the body, it will encounter a vast range of biological components, such as proteins, membranes, DNA and organelles, and several nano-bio interfaces are established. Interactions at the interface lead to various processes such as formation of protein coronas, particle wrapping at the cell membrane, endocytosis and intracellular biocatalysis, all which can have possible bioadverse outcomes. [13] For instance, nanoparticles taken up via some endocytic pathways may elicit an immune response. [68] The nature of the interface is influenced by nanoparticle characteristics including size, shape, surface area, surface charge and hydrophobicity, which thereby also will be determining factors affecting nanoparticle cytotoxicity.

The first step towards understanding how the body will react to administered polymeric nanoparticles will nearly always rely on *in vitro* cytotoxicity studies. In the majority of published articles investigating nanoparticle toxicity, cell viability after exposure is measured by colorimetric methods. [64] These assays detect cell death by changes in either metabolic activities or cell membrane permeability. One method that relies on the former is the alamarBlue® cell viability assay. This assay

has incorporated a growth indicator, resazurin [69], which is reduced to resorufin by innate metabolic activity, meaning that continued growth maintains a reduced environment, while inhibition of growth results in an oxidized environment. [70] Detection of this difference in redox state is possible since resazurin changes from its oxidized, non-fluorescent, blue form to its reduced form, which is fluorescent and red in color. As mentioned in the beginning of this section, the outcome of cellular toxicity may not only be cell death. To complement the nanoparticle toxicity studies described above it is also necessary to investigate possible inflammatory and genotoxic responses.

2.2.2 Preparation of polymeric nanoparticles by the miniemulsion process

Various methods for preparing polymeric nanoparticles have been developed. These methods are classified into two main categories, depending on whether the process requires a polymerization reaction or if it is achieved directly from a macromolecule or pre-formed polymer. [52] The choice of preparation process is dependent on the polymer, but also on which substances it should be loaded with, its site of action and therapy regime. [55]

One example of a highly versatile method for preparation of polymeric nanoparticles that requires a polymerization reaction, is the miniemulsion process. A miniemulsion is a relatively stable emulsion of small droplets dispersed in a continuous phase. The droplets have a narrow size distribution and are usually between 20 and 200 nm in diameter. [71] To obtain the nanodroplets, high shear forces with ultrasound or high pressure homogenization are applied on a mixture of two immiscible fluids. The size of the final miniemulsion droplets is mainly dependent on the type and amount of emulsifier used in the system. [72]

Preparation of nanoparticles with hydrophobic cores is performed by a direct miniemulsion process, where a mixture of monomer, co-stabilizer and the agent to be encapsulated is dispersed in an aqueous solution containing surfactant. Upon intense shearing of the mixture, monomer droplets stabilized by the surfactant are formed in the aqueous phase. The co-stabilizer will act as an osmotic pressure agent within the droplets and prevent them from coalescing. [73] After the miniemulsion is made, polymerization of the monomer occurs at the interface leading to formation of solid polymeric particles. One important feature with the miniemulsion process is that the droplets act as nanoreactors, such that the size and content of the resulting nanoparticles are almost identical to the droplets in the initial emulsion. The polymerization reaction can either be triggered by addition of an initiator or by initiator already present in the aqueous solution. Various types of

polymerization reactions are used, including radical, anionic, cationic and enzyme catalyzed polymerization. In figure 2.5 an overview of the miniemulsion process is shown.

The main advantage with preparation of polymeric nanoparticles by the miniemulsion method is the possibility of simultaneous encapsulation of relevant hydrophobic drugs, contrast agents and fluorescent markers in a one-step process. In addition, surface functionalities, like PEGylation and targeting ligands, can be added by co-polymerization such that further modifications are not needed. A summary of the pros and cons with the miniemulsion process is displayed in table 2.6.

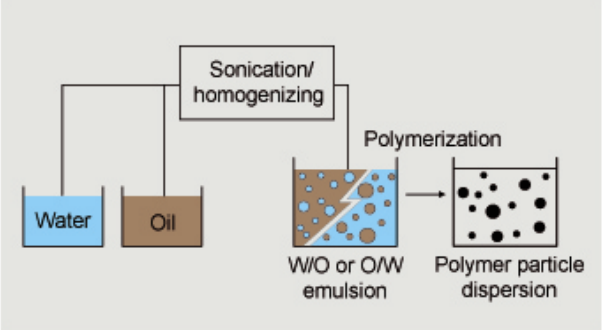

Figure 2.5: Schematics of the miniemulsion process for preparation of polymeric nanoparticles. A miniemulsion is created by applying high shear forces on a mixture of an oil and water phase, followed by the initiation of polymerization to form solid particles. Figure from Ýrr Mørch, SINTEF Materials and Chemistry.

Table 2.6: Pros and cons with preparation of polymeric nanoparticles by the miniemulsion process. Provided by Ruth Schmid, SINTEF Materials and Chemistry.

Advantages	**Disadvantages**
• One-step and low cost process • Easy up-scaling to industrial scale • Compatible with a wide range of polymers • High loading with active substance, possible to encapsulate several substances in one step • No need for further modification steps to add surface functionalization	• High shear forces necessary • Residual surfactant, monomer and/or stabilizer in the final product • Unwanted chemical reactions between active substance and monomer may occur before or during polymerization • Lack of control of molecular weight and polydispersity of the polymer

2.3 Nanomedicines in cancer therapy

Cancer treatment is one of the most important fields for research on nanomedicines, motivated by how chemotherapy is limited by systemic toxicity and poor bioavailability of drugs at the tumor site. Chemotherapeutic agents tend to have rapid degradation rates or they are quickly excreted, and because of poor distribution they often fail to localize to the tumor. [74] In fact, only 0.1% of administered anticancer drugs are able to reach the diseased area [75], resulting in remaining agent being delivered where it is not required, possibly creating adverse effects in healthy tissue.

Attempts to enhance the biodistribution of anticancer drugs, reduce free drug toxicity and favor tumor accumulation are done by designing drug delivery systems exploiting nanocarriers. [25] By associating chemotherapeutic drugs with nanocarriers, the toxic side effects can be significantly reduced when compared to free drug. Increasing the bioavailability and achieving homogeneous distribution of drugs at the tumor site still remain a major challenge. Tumor tissue and normal tissue have different physiology, giving rise to a set of transport barriers. Drug delivery to tumors is therefore compromised, and to avoid heterogeneous distribution of drugs, these physiological barriers need to be overcome. In addition, to further increase bioavailability of the drug, different strategies for targeting of nanomedicines to tumors have been evaluated.

2.3.1 Physiological barriers to drug delivery in tumor tissue

The transport of a therapeutic agent from systemic circulation to tumor cells depends on the process of vascular, transvascular and interstitial transport. In other words, a nanomedicine must first flow to different regions of the tumor through the vascular network, then cross the vessel wall and at last try to reach the target cells by penetrating the tumor interstitium. Because of differences in structure between normal and cancerous tissue, physiological barriers that limit both the rate and extent of drug delivery to target cells are introduced. The major contributions to the drug delivery barriers in tumor tissue are abnormal blood vessel network, accumulated solid stress, elevated interstitial fluid pressure and a dense interstitial structure. [76] It is important to note that these are inherent properties of the tissue, and both the existence and contribution from each might vary between cancer types.

In order for a tumor to grow beyond 1-2 mm in size, the tumor switches to an angiogenic phenotype to provide sufficient delivery of oxygen and nutrients for further growth. [77] Cancer cells therefore secrete proangiogenic factors to the sur-

rounding tissue, leading to growth of new blood vessels that connect the tumor to the body's vascular system. Since these factors are overproduced, the growth happens rapidly, resulting in an immature vasculature with a highly irregular structure and vessels that remain leaky and tortuous. The high vessel tortuosity contributes to an elevated viscous and geometric resistance, while the structure of the vessel network causes heterogeneous blood flow through the tumor. Both characteristics compromise tumor blood flow, and leave the average velocity of red blood cells up to an order of magnitude lower than in normal tissue. [78] Consequently, the abnormal blood vessel network affects the movement of nanomedicines through the vasculature and into different regions of the tumor, resulting in nonuniform drug delivery.

Solid stress in the tumor is induced when cells proliferate in an uncontrollable manner in a constricted space, and results in compression of blood and lymphatic vessels. [79, 80] When blood vessels are compressed, or even collapsed, blood flow to the tumor is restricted and may leave some regions of the tumor tissue unperfused. The presence of unperfused regions lead to a hypoxic, acidic and necrotic tumor microenvironment, which can further contribute to drug resistance and tumor progression. [76] Because of compression of lymphatic vessels, lymphatic drainage from the tissue is not working properly and fluid will accumulate in the interstitial space, causing higher interstitial fluid pressure than in normal tissue. The leaky blood vessels will further contribute to the elevated interstitial fluid pressure. Discontinuities in endothelial cells lining the vessel wall cause tumor vessels to be hyperpermeable, and more fluids and plasma macromolecules will leak into the tumor interstitium. [81] Combined with the nonfunctional lymphatic drainage, this results in an elevated interstitial fluid pressure which approaches the value of the microvascular pressure. In normal tissue, the transvascular and interstitial transport are driven by diffusion and convection. The main driving force for convective transport is the transvascular and interstitial pressure gradients. In tumor tissue these gradients will be approximately zero, leaving diffusion the main transport mechanism of nanomedicines crossing the vessel wall and penetrating the tumor interstitial space. Transvascular and interstitial transport are thereby hindered by the elevated interstitial fluid pressure, causing transport of nanomedicines to be limited by diffusion, resulting in poor distribution and short penetration range of the therapeutic agent.

The interstitial matrix is a network comprising of a variety of proteins and polysaccharides. In a tumor, where the cellular density is high and solid stress is accumulated, the interstitial matrix is compressed into a dense and tortuous network. [82] Transport of a nanoparticle system within the interstitial matrix is primarily governed by diffusion, and the movement is affected by its size together with the

viscosity of the interstitial fluid. Because diffusion is size dependent, smaller nanomedicines have an advantage when compared to larger ones, since they are less hindered by interactions with the interstitial matrix and may achieve deeper tumor penetration. In conclusion, the dense structure of the interstitial matrix causes barriers to nanomedicine movement in tumors and results in a heterogeneous distribution with nanoparticles concentrated in perivascular regions.

2.3.2 Passive targeting of nanomedicines to tumors

When delivering drugs with nanocarriers to tumors, one beneficiary aspect with tumor physiology can be found. The leaky blood vessels, with abnormally wide gaps between endothelial cells, allow extravasation of materials with a certain size, typically in the range of nanomedicines. Furthermore, solid tumors are unable to eliminate extravasated nanoparticles since the lack of functional lymphatics leads to fluid retention. The combination of these two physiological characteristics give rise to the enhanced permeability and retention (EPR) effect for macromolecules in solid tumors [84], allowing for long-circulating nanomedicines to accumulate in tumors over time. (Figure 2.6A) Since this way of guiding nanomedicines to tumors only rely on the pathophysiological state of cancerous tissue, it is generally referred to as passive targeting. Passive targeting is arguably the most important strategy for targeting nanoparticle systems to tumors. [85]

The EPR effect has proven to passively guide nanomedicines to solid tumors. In fact, the clinical success Doxil®/Caelyx® relies on passive accumulation at its target site. Despite this, it must not be disregarded that the EPR effect is a phenomenon which varies significantly from tumor model to tumor model, from patient to patient, and even within a single tumor. [86, 87] In some cases, particles as large as 200 nm are able to extravasate, whereas in others not even small molecules are able to enter the interstitium. [88] These variations are mainly caused by heterogeneities of vascular permeability; some vessel areas can have intact endothelial lining or the vascular leakiness can be compromised by the presence of a dense perivascular lining.

2.3.3 Active targeting of nanomedicines to tumor tissue

Opposed to passive targeting of nanomedicines, active targeting can be achieved by conjugating ligands to the surface of a nanocarrier that promotes binding to specific cell surface receptors expressed at the target site. Nanoparticle systems that are actively targeted to cancer cells are made with the motivation of improving target cell recognition and enhancing cellular uptake. The general idea is that

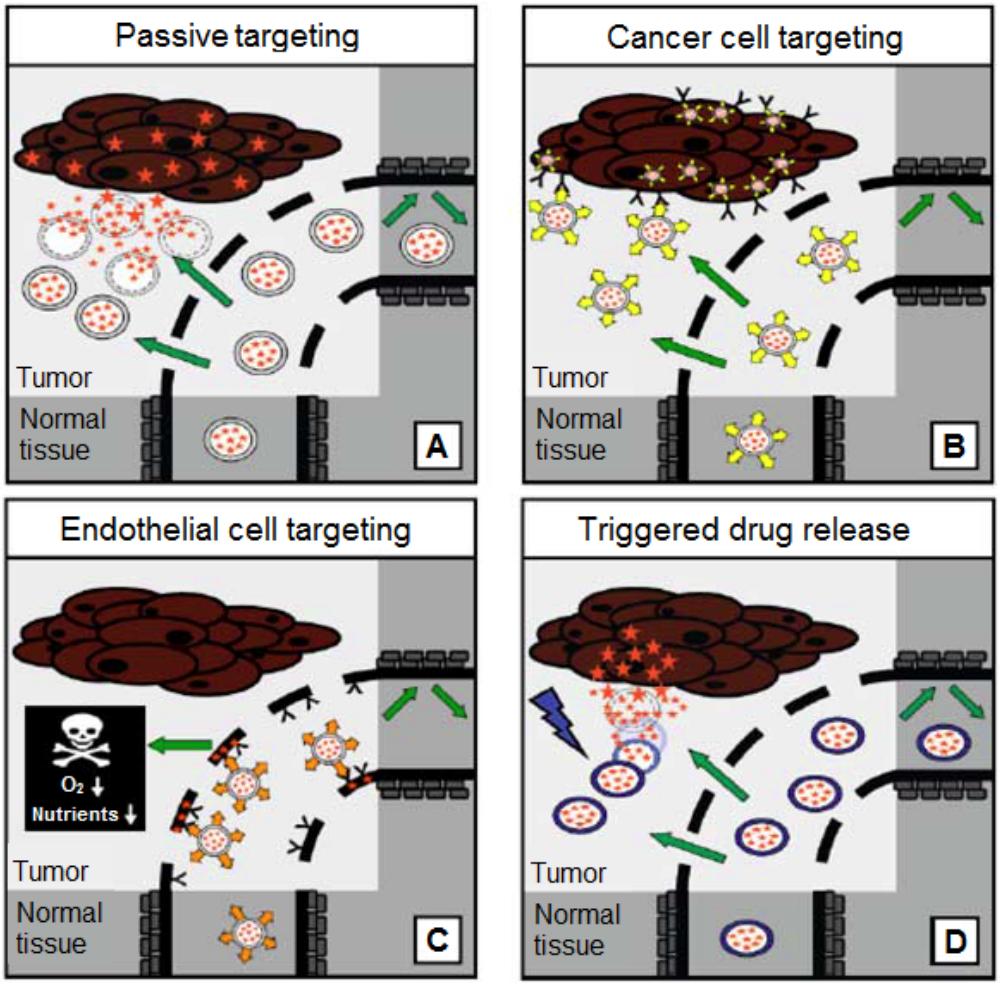

Figure 2.6: Overview of different targeting strategies for delivery of drugs to tumors. A: Passive targeting of nanomedicines to tumors relies on the enhanced permeability and retention effect. B: Active targeting to cancer cells intends to improve cellular uptake of the nanomedicine. C: Active targeting to endothelial cells aims to reduce blood supply to tumors and thereby deprive the cells from oxygen and nutrients. D: Targeting to tumors by an externally applied stimulus to trigger drug release from stimuli-sensitive nanomedicines. Figure adapted from reference [83].

the EPR effect will be responsible for tumor accumulation, while the targeting ligands increase the specificity of the nanoparticle system. (Figure 2.6B) Ideally, interactions between the ligand-bearing nanocarrier and receptors at the cell membrane will cause the nanoparticle to be internalized through the same endocytosis pathway as the ligand alone. A large variety of substances can be used as targeting ligands, including antibodies and other proteins, lipoproteins, hormones, charged molecules, and saccharides. [89] It is important that the ligand binds selectively to the desired receptor, and the target tissue should overexpress the surface marker in order to maximize specificity of the interaction.

In recent years, significant progress has been made with active targeting strategies at the preclinical level, although no actively targeted nanomedicines have been approved for clinical use, and only very few are in clinical trials. [85] The constraints on cancer cell targeted nanomedicines are believed to mainly be caused by two factors. First, after the nanomedicine has crossed the blood vessel wall, it needs to overcome additional physiological barriers before it can reach and bind tumor cells. (Barriers to interstitial transport, see section 2.3.1) Second, attachment of a targeting ligand on the surface of a nanocarrier can cause increased immunogenicity and unspecific protein adsorption, thus lowering the amount of nanomedicines passively accumulated in the tumor. As it seems today, the biggest advantage with nanomedicines actively targeted to cancer cells, over those that only rely on passive targeting, is that they are much more efficiently internalized into cells. This property can be particularly useful for drugs that need to be delivered intracellularly.

An active targeting approach that circumvents the barriers to interstitial transport, is based on active targeting to angiogenic endothelial cells rather than cancer cells themselves. [90] Such a targeting strategy aims to increase drug delivery to the tumor endothelium, thereby depriving tumors of oxygen and nutrients. (Figure 2.6C) Since nanomedicines targeted to the tumor vasculature are not dependent on extravasation and penetration through the dense interstitium, and because of their frequent encounter with their target receptors, it is claimed that endothelial cell targeted nanomedicines possess more potential for improving antitumor efficacy than cancer cell targeted nanomedicines. [88]

2.3.4 Targeting to tumors by triggered drug release from nanomedicines

One of the fastest growing areas of research on nanomedicine targeting is the design of nanocarriers that selectively release their contents upon exposure of an external stimulus. (Figure 2.6D) The idea behind such nanoparticle systems is

that when certain stimuli is applied to the pathological area from outside of the body, the properties of the nanoformulation is changed, allowing for enhanced or controlled drug release. Examples of externally provided stimuli can be heat, light, ultrasound and magnetic fields. In theory, the stimuli-responsive nanosystems hold significant clinical potential, since they are designed to only release the therapeutic agent upon application of spatially confined triggers, thereby maximizing drug release in tumor tissue and at the same time protecting healthy tissues against damage. [88] A challenge with stimuli-responsive nanomedicines is to make their formulation really specific to the external stimulus. Moreover, to provide triggered drug release, the location of the tumor must be known, meaning this strategy is not ideal for the treatment of metastases.

Ultrasound can be used in different ways for triggered drug delivery. It can release encapsulated drugs from a nanocarrier, but it can also be used to overcome existing barriers in tumor tissue by modification of the tumor microenvironment. When energy is deposited in tissue from focused ultrasound, three main biological effects occur: hyperthermia, radiation forces and acoustic cavitation. [91] The generation of heat from applied ultrasound can trigger drug release from temperature sensitive nanomedicines. [92] An example of such carriers are the temperature sensitive liposomes developed by Needham, Dewhirst and co-workers. [93] These liposomes loaded with doxorubicin (patented under the trade name ThermoDox®) are in clinical trials for different indications, where one planned study will evaluate High Intensity Focused Ultrasound in combination with ThermoDox® for treatment of prostate cancer metastases to bone. (Clinical trial ID: NCT01640847) Local heating of tissue can have additional beneficial effects; increased blood flow, vascular permeability and diffusion can facilitate both vascular and transvascular transport, resulting in enhanced tumor accumulation of nanoparticles.

Nonthermal biological effects of ultrasound can generate radiation forces that improve convection of nanomedicines and therapeutic agents within the tumor interstitium, and thereby help with overcoming the diffusion problem associated with the dense tumor interstitial matrix. The use of microbubbles as ultrasound contrast agents, either in combination with drug delivery systems or as a multifunctional system (described in section 2.1.3), may induce cavitation-based effects connected with bubble oscillations. Acoustic cavitation can act positively on the transport of drugs in a tumor, and also cause a local increase in cell membrane permeability. Microstreaming will occur around bubbles undergoing stable cavitation, which can increase the speed of convective transport of drugs by orders of magnitude compared to diffusive transport alone [94] Collapse of an oscillating bubble following inertial cavitation emits high pressure microjets to the surroundings. These microjets can inflict shear stresses on nearby cells which again will

increase membrane permeability by creating transient pores in the cell membrane, a process termed sonoporation. It has been reported that sonoporation allows for transmembrane delivery and cellular uptake of macromolecules between 10 kDa and 3 MDa. [95] To summarize, the combined biological effects of ultrasound on cancer cells, endothelial cells and the tumor interstitial matrix can potentiate localized drug delivery by facilitating vascular, transvascular and interstitial transport of nanomedicines and drugs, as wells as by aiding their entry into cells.

2.4 Cellular uptake and trafficking of nanoparticles

Nanocarriers offer unique possibilities to cross cellular barriers in order to facilitate the delivery of therapeutic agents. Various internalization pathways are available for nanoparticle uptake in mammalian cells. These processes are collectively termed endocytosis. Generally, endocytosis can be divided into two main categories: phagocytosis and pinocytosis. Phagocytosis is the uptake of particulate matter and occurs primarily in specialized cells such as macrophages and neutrophils. [96] Pinocytosis on the other hand, occurs in all cells and is the internalization of fluids and solutes. It can be divided into macropinocytosis, clathrin-dependent endocytosis, caveolae-mediated endocytosis and mechanisms independent of both clathrin and caveolae. For drug delivery to cancer cells, it is most relevant to look into the pinocytosis pathways. Figure 2.7 illustrates the different endocytosis mechanisms mentioned above.

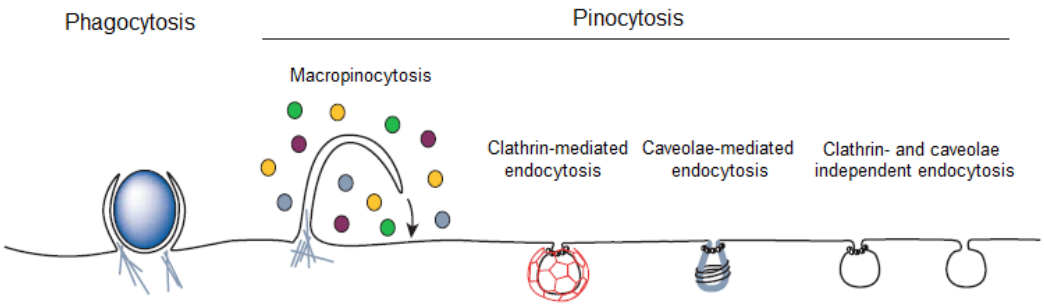

Figure 2.7: An illustration showing the principal internalization pathways in mammalian cells, divided into phagocytosis and pinocytosis. Pinocytosis is further subdivided into macropinocytosis, clathrin-dependent endocytosis, caveolae-mediated endocytosis, and other mechanisms independent on both clathrin and caveolae. Figure adapted from reference [97].

Endocytosis is a form of transport where extracellular material is taken up in an energy dependent manner. A nanoparticle located at the exterior of a cell can interact with the plasma membrane. These interactions can lead to the nanoparticle being endocytosed by the cell. First, the cargo is enclosed in membrane invaginations by infolding of the plasma membrane, followed by pinching off of a membrane bound vesicle or vacuole. Endocytic vesicles fuse with each other, or an already existing endosomal compartment to form an early endosome. In these cellular structures sorting of the cargo is carried out. The cargo can then follow different routes. [98, 99, 100] Material destined to be recycled to the extracellular space is either removed directly back to the cell surface, or pass through a recycling endosome for further processing. Trafficking between endosomes and the Golgi apparatus connects the endocytic and secretory pathways, and provide delivery of endocytosed material to various intracellular compartments. In the process of endosome maturation (the transition from early to late endosome), the pH in the compartment decreases and further fusion with endocytic vesicles is prevented. Late endosomes can fuse with or mature into a lysosome, where the content is degraded. A great portion of internalized cargo remains in the late endosomes to follow this degradation route. Figure 2.8 summarizes the major trafficking pathways for endocytosed material.

The formation of the endocytic vesicle and further intracellular trafficking differs depending on which endocytic pathway involved in the internalization process. Table 2.7 is provided to give a short summary of the vesicle morphology and implicated proteins in the different pinocytosis mechanisms.

Table 2.7: Some known characteristics with the pinocytosis pathways described in the text. Table adapted from reference [101].

Endocytosis pathway	**Morphology**	**Implicated proteins**
Macropinocytosis	Highly ruffled	Actin, Rac1
Clathrin-mediated	Vesicular	Clathrin, Dynamin, Rab5
Caveolae-mediated	Vesicular or tubovesicular	Caveolins, some evidence of dynamin dependence.
Clathrin and caveolae independent	Vesicular or tubular	Different mechanisms dependent on Arf6, flotilin, Cdc42 and RhoA respectively. Majority of pathways seem to be dynamin independent.

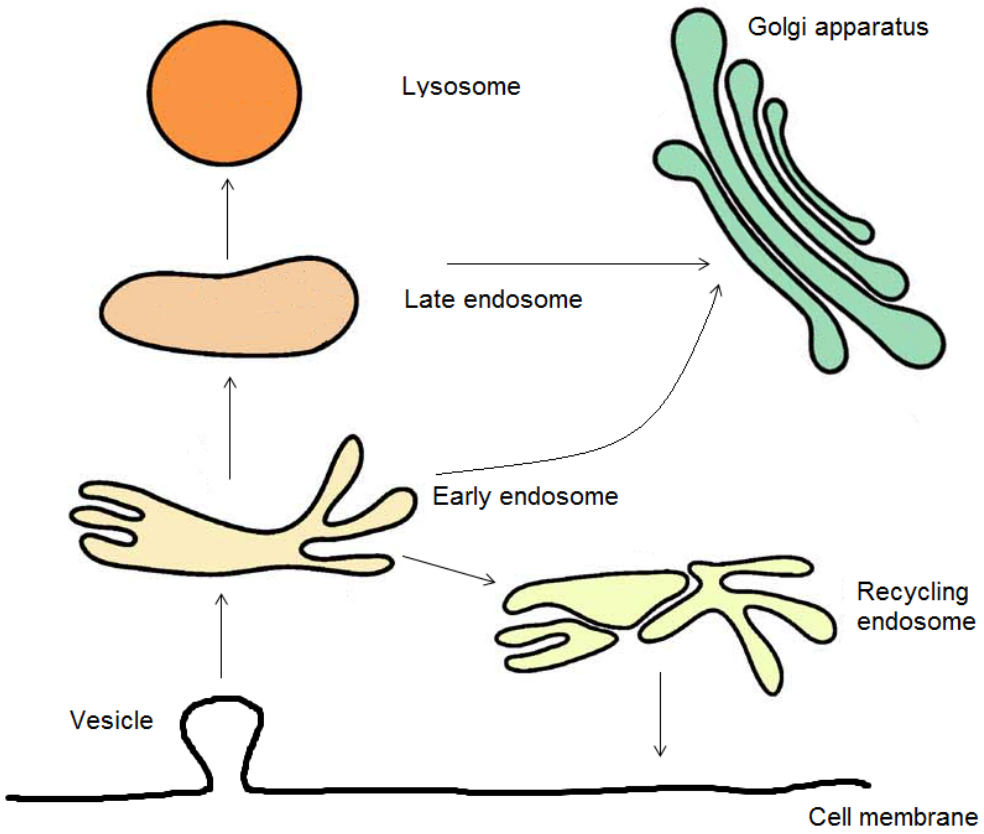

Figure 2.8: A schematic diagram of the principle organelles and pathways involved in endocytosis and intracellular transport of nanoparticles. Trafficking between endosomes and the Golgi apparatus links the pathways of endocytosis and secretion. Figure adapted from reference [98].

Nanoparticles can employ multiple pathways for cellular entry. Investigation of the cellular uptake and trafficking of nanocarriers suggests that this process is highly dependent on the particles' physicochemical characteristics. [102] Properties such as size, shape, charge and hydrophobicity are ascertained to influence the endocytosis of nanomaterials. In addition, the endocytic machinery present in a cell varies between cell types, meaning that rate and mechanism of uptake also is cell-line dependent. [103] Several review articles [14, 102, 103, 104] are available that summarize published data on nanoparticle uptake and transport in cells, but given the diversity of nanoparticles and cell types utilized in research today it is difficult to make any conclusions regarding common factors. In order to develop efficient drug delivery systems based on nanocarriers, it is necessary to increase our understanding on how they are internalized and distributed in cells, and the mentioned review articles reveal that thorough studies are needed in each situation.

2.5 Drug release from biodegradable nanoparticles

Upon arrival at the target site, a nanocarrier should deliver its contents in an efficient manner to achieve sufficient therapeutic response. Depending if the therapeutic agent is covalently bound or encapsulated within the nanoparticle, different release strategies apply. Covalent drug delivery requires direct breaking of the chemical bond between the drug and the nanocarrier, whereas non-covalently bound drugs do not require additional external stimuli to be released. [105] Since pharmacological targets often are located intracellularly [11], many drugs require uptake in cells for the delivery to be successful. This is possible either by extracellular release followed by drug diffusion across the cell membrane, or the nanocarrier must enter the cell by endocytosis before drug release. The release of therapeutic agent outside cells is more efficient when using hydrophobic drugs, since it is the partition coefficient of a molecule that determines the diffusion rate across a lipid bilayer. [106]

There are a number of possible methods for drug release from biodegradable nanoparticles: [107, 108, 109]

1. Desorption of drug bound to the surface
2. Diffusion through the nanoparticle matrix
3. Nanoparticle matrix erosion
4. A combined erosion-diffusion process

It is proposed that several of the above mentioned processes can contribute to the overall mechanism for drug release. First, a rapid initial release can stem from weakly bound or adsorbed drug on the nanoparticle surface. Then, a slower,

more controlled release can follow, which is attributed to nanoparticle degradation, diffusion of the drug through the nanoparticle matrix, or both. This means that the diffusion coefficient of the drug and the biodegradation rate of the nanoparticle are determining factors of drug release. Consequently, if diffusion of a drug is faster than matrix erosion, the mechanism of release is predominately controlled by a diffusion process.

2.5.1 Nile red properties and its release mechanisms from nanoparticles

The release and subsequent cellular uptake of a lipophilic probe can be used as a tool to study the delivery of hydrophobic drugs from nanoparticles to cells. In this project, the fluorescent probe nile red has been used for this purpose.

Nile red is a highly hydrophobic, benzophenoxazone fluorescent dye. It is intensely fluorescent in all organic solvents, but efficiently quenched in aqueous solution. Nile red has high affinity for intracellular lipid compartments [110], and depending on what it is associated with, the excitation and emission maxima can vary over a range of 60 nm. [111] The dye exhibits a blue shift of the fluorescent emission maxima which is proportional to the hydrophobicity of the environment. This means that nile red associated with more hydrophobic compounds (e.g. intracellular lipid-droplets) are more visible when cells are viewed for yellow-gold fluorescence, than when cells are viewed for red fluorescence, where a diffuse general staining of the cytoplasm (attributed to nile red associated with various cytosolic proteins) becomes more apparent.

Haynes and Cho [112] proposed that transfer of nile red from hydrophobic nanoparticles and into cells could occur through three processes:

1. By endocytosis
2. By probe dissociation from the particle and subsequent diffusion towards the cell and over the plasma membrane
3. By partition of the probe upon particle collision with the cell membrane

Endocytosis is already presented in section 2.4, so further only the diffusion-based drug delivery processes will be discussed. Both the diffusion dependent processes rely on a hydrophobic release mechanism, in which the release is initiated when the nanocarrier encounter an even more hydrophobic environment (such as a cell membrane) into which the probe can diffuse. [105] For the second mechanism, the dissociation of the probe from the particle and into the less hydrophobic environment (not favorable process) will be rate-determining, whereas the rate of the

third mechanism is determined by particle-membrane collisions. Hence, the second mechanism is believed to be much slower than the collision-induced process.

Literature has provided evidence that different nanocarriers (polymeric nanoparticles, liposomes and micelles) indeed can deliver their payloads mainly in a release- or contact-mediated manner. [113, 114, 115, 116] These results implicate that the release rate can be used to determine cellular drug content. In order for such a drug delivery system to have clinical applications, the leakage of drugs during systemic circulation must be minimized. In addition, it is important to assess how a drug prefers the nanoparticle environment versus the biological microenvironment. [105]

2.6 Flow cytometry

Flow cytometry (FCM) is a quantitative technique used for analyzing objects in the micrometer size range, such as cells. A liquid cell suspension is passed through a laser beam and scattered light and fluorescence are detected. This information can be used to obtain the physical and/or chemical characteristics of cells. Examples of some FCM applications are cell cycle analysis, immunophenotyping, viability measurements and identification of extra- or intracellular protein expression.

2.6.1 General principles of flow cytometry

As seen in figure 2.9, a flow cytometer's main parts are a flow cell, a light source, an optical system, light detectors and a data processing and operating unit. [117] The cell suspension to be analyzed is first injected into the flow cell, where the sample fluid is hydrodynamically focused into a thin stream by the surrounding sheath fluid. Further into the fluidics system, the sample stream will intersect with a laser beam placed orthogonal to the flow. The hydrodynamic focusing serves to make cells flow in a single file, such that only one cell at the time are passing the detection point. When cells in the stream pass through the sensing point, light from the laser source interacts with each individual cell to produce scattering and/or fluorescence. The generated photons hit a photodetector and this intensity pulse is translated into a voltage pulse proportional to the total number of photons that reached the detector. This voltage is then amplified by a series of linear or logarithmic amplifiers, and converted into a digital signal that can be displayed graphically by the data processing and operating unit. [117]

The optical response generated by interaction of a cell with the laser beam consists of forward scattered and side scattered light. In addition, absorption either by cellular components or by fluorochromes staining a cell, produces fluorescence

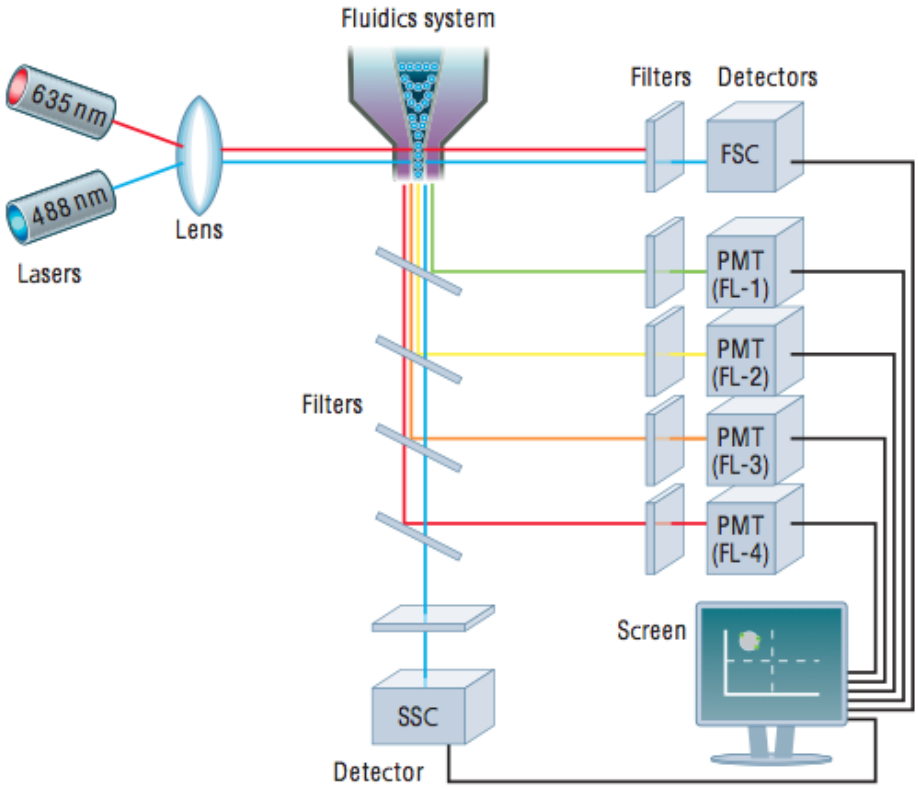

Figure 2.9: Schematic diagram showing the setup and main components of a flow cytometer. [117]

signals shifted in wavelength from that of the exciting beam. [118] These detected parameters provide information about the cells' properties. The magnitude of forward scattered, or low angle scattered light (0.5 to a few degrees), is nearly proportional to the size of a cell. Side scattered, or highly scattered light ($\sim$90°), is related to the granularity and internal structure of a cell. To measure other cellular characteristics, the cell sample can be labeled with a fluorescent molecule. Such fluorescent dyes can bind to specific molecules inside the cell or on the cell surface, thus making it possible to detect certain cellular parameters. Since every cell becomes equally illuminated at the detection point, proportionality between fluorescence intensity and the measured parameter is assured.

One of the strengths with FCM is that excitation with several lasers of different wavelengths are possible at the same time. Measurements of more than one cellular parameter can then be performed simultaneously. By combining results from light-scattering and fluorescence measurements on both stained and unstained cells, a wide range of cellular parameters can be detected. Some of the cell characteristics that can be determined are cell size, granularity of cytoplasm, cell shape, viability, autofluorescence, and in addition cell components like DNA, surface receptors and antigens. [119] Alternative techniques to measure many of these parameters exist, but the real power of FCM lies in the ability to obtain information on how the parameters are distributed and correlated in the cell population.

2.6.2 Data analysis of flow cytometry measurements

Data obtained during FCM measurements are analyzed by the flow cytometer software and presented to the user graphically. Single parameter histograms plot the fluorescence or light scatter intensity against number of cells. This gives information about the intensity distribution of a particular parameter in the cell sample. A population of cells that have high intensity of the desired property is termed a positive dataset. Figure 2.10 shows a typical histogram with a negative (autofluorescence) and positive population. To obtain further information about how the parameters are distributed in the sample, two single parameter histograms can be combined to yield a two-dimensional dot-plot.

From a single parameter histogram the software allows you to obtain the median fluorescence intensity (MFI) of the sample. The median is the fluorescence value below which 50% of the events are found, and for logarithmic data this number gives a better estimation of the central tendency of a population than the mean. [120] An observed shift in fluorescence intensity can then be quantified by reporting the relative MFI values compared to a control. The percentage of positive cells can also be estimated from the negative cell population. A marker that

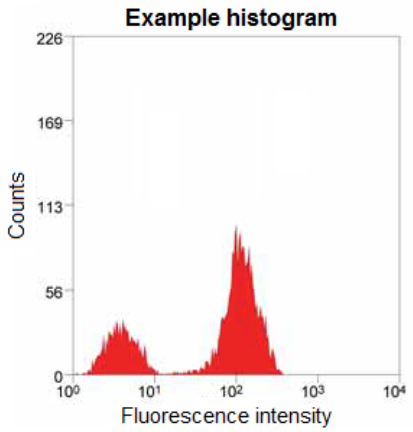

Figure 2.10: A typical single parameter histogram obtained in FCM analysis. [117] The histogram shows the fluorescence intensity of the unstained population (autofluorescence) and the stained sample. Thus, the left peak represents a negative dataset, whereas the right represents a positive. Number of events (counts) are displayed on a linear scale on the y-axis, while the x-axis represents the fluorescence intensity on a logarithmic scale.

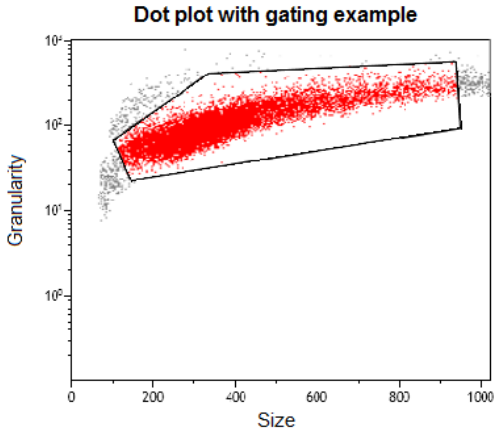

Figure 2.11: A typical dot plot of forward scatter versus side scatter obtained in a FCM analysis. The plot shows the distribution of cells in the sample based on size and granularity. A gated population is set to avoid cell debris and cell clusters. The forward scatter signal is plotted on a linear scale and the side scatter signal is plotted on a logarithmic scale.

includes a small percentage of the control sample is set, and any intensity greater than this in the stained samples are defined as positive.

An important feature with FCM data analysis is the gating option. Gating is the selection of a specific set of cells for further analysis and exclusion of data from unwanted events. For instance a dot plot with forward scatter against side scatter signal shows the distribution of cells based on size and granularity. This information can be used to make a gate to eliminate cell debris, fragments and cell clusters, such that subsequent analysis only is based on data from whole, single cells. Figure 2.11 illustrates such a gating example.

2.7 Confocal laser scanning microscopy

Confocal laser scanning microscopy (CLSM) is a technique routinely used for imaging of fluorescently labeled biological specimens. The sample is illuminated by a focused scanning laser beam, and out-of-focus light is rejected from reaching the detector by a confocal aperture. This basic principle of confocal imaging provides images with enhanced contrast compared to conventional widefield optical systems. Examples of typical information that can be obtained by investigation with CLSM is whether the fluorescent signal originates from the membrane or the cytosol of a cell, if different fluorescent signals are co-localized within the same organelle and the three-dimensional fluorescence distribution in the specimen. [121]

The confocal laser scanning microscope is an integrated system consisting of a fluorescence microscope, multiple laser light sources, a confocal scan head with optical and electronic equipment, a monitor for display, and software for acquiring, processing and analyzing images. [121] Figure 2.12 shows the optical principle of a confocal laser scanning microscope. First, a coherent laser beam is reflected by a dichromatic mirror and focused onto the sample by an objective lens. When the laser beam interacts with the specimen, fluorescent photons are generated. The fluorescent photons originating from the excited point are then collected by the same objective onto a pinhole aperture placed in front of a photodetector. This pinhole aperture is situated in the conjugate plane of the focused sample plane, thereby largely excluding fluorescence signals from objects above and below the focal plane. Consequently, all out-of-focus background is removed and only photons originating from the plane in focus will contribute to the image. The intensity of the fluorescent photons incident on the photodetector are translated into a voltage signal, and further digitalized and displayed on the monitor. Various filters and lasers can be used to obtain multichannel images such that detection of more than one fluorescent probe is possible at the same time.

To generate an entire image, the laser beam is scanned across a defined horizontal plane of the specimen in a raster pattern. In this way, CLSM allows investigation of thin optical sections within the sample. The thickness of the optical sections can be adjusted by varying the size of the pinhole aperture. Additionally, optical sections from selected depths in the sample can be scanned and collected to generate a three-dimensional image. By changing the scan speed of the laser, the contrast and quality of the image can be modified. [122] Slower scan speed gives superior image quality, but requires longer acquisition time.

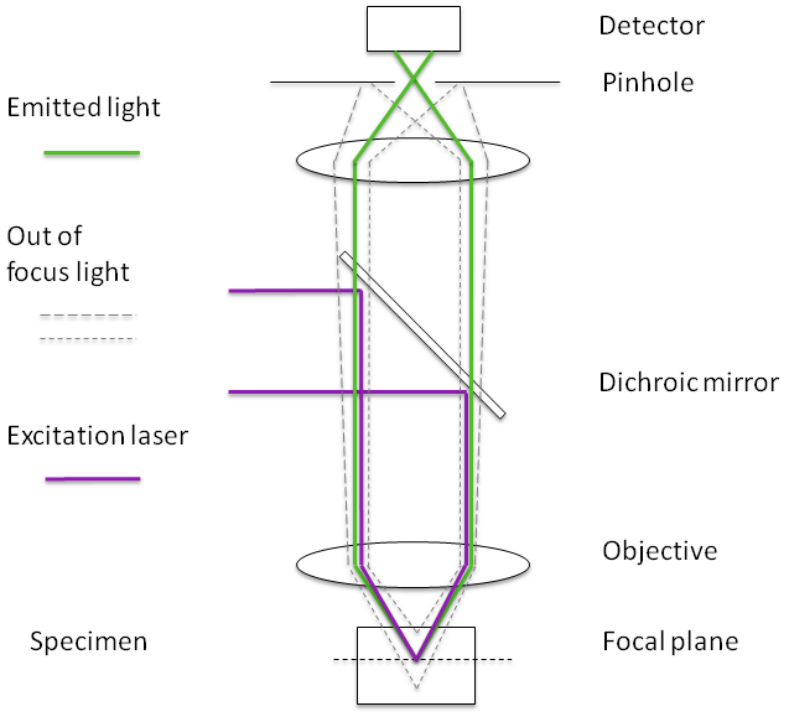

Figure 2.12: Schematic diagram showing the optical setup of a confocal laser scanning microscope.

3 Materials and Methods

3.1 Nanoparticles

Colleagues at SINTEF Materials and Chemistry have synthesized and characterized the polymeric poly(alkyl cyanoacrylate) nanoparticles used in all experiments. An overview of the physicochemical properties of all batches is displayed in table 3.1. The given size and zeta (ζ) potentials were measured by dynamic light scattering in a Malvern Zetasizer Nanoseries.

3.1.1 Synthesis of nanoparticles

The nanoparticles are produced by a direct miniemulsion process. This process involves mixture of an acidic aqueous phase containing surfactant and initiator, with an oil phase containing monomers and co-stabilizer. All batches are produced with poly(butyl cyanoacrylate) (PBCA) as the monomer, except 89 which consists of poly(octyl cyanoacrylate) (POCA). Upon sonication of the two phases, a miniemulsion is formed. The surfactant used to stabilize the emulsion is sodium dodecyl sulfate (SDS), except for particle batch 71B and 72 where TWEEN 80 is used. Anionic polymerization of the monomer droplets is initiated by addition of PEG to the emulsion, due to the presence of amine groups on the PEG chains, resulting in PEGylated nanoparticles. After polymerization, the surfactant is redundant, and is removed by dialysis in water. More details on the miniemulsion process can be found in section 2.2.2.

Batch 44 is synthesized at an earlier time than the rest, and differs at some points. It is produced with hexadecane as a co-stabilizer, whereas all other batches are produced with Miglyol 810N. In addition, the PBCA polymer is cross-linked in the particle.

3.1.2 Fluorescent labeling of nanoparticles

To be able to detect the nanoparticles in FCM and CLSM, they are labeled with a fluorescent marker. These probes are associated with the particles in various ways. Nile red and fluorescein acrylate is encapsulated in the hydrophobic core of the particle, meaning they are mixed with the oil phase when the emulsion is formed. The difference between the two fluorescein acrylate batches is that in batch 69, fluorescein acrylate was dissolved in oil approximately 12 hours before preparation since difficulties with dissolving it in the oil phase was experienced during synthesis

Table 3.1: Physicochemical properties of the nanoparticles used in the experiments.

Batch	**Polymer**	**Size** (nm)	**PDI**	**ζ-potential** (mV)	**PEG**	**Surfactant**	**Fluorochrome (w/w)**
44	PBCA	153	0.08	-19	Jeffamine M-1000	SDS	Nile red (0.02%)
66	PBCA	150	0.02	-25	Jeffamine M-1000	SDS	Fluoresceinamine (0.1%)
68	PBCA	160	0.07		Jeffamine M-1000	SDS	Fluorescein acrylate (0.6%)
69	PBCA	158	0.16	-38	Jeffamine M-1000	SDS	Fluorescein acrylate (0.6%)
71B	PBCA	409	0.36	-36	TWEEN 80	TWEEN 80	Nile red (0.1%)
72	PBCA	751	0.31	-36	TWEEN 80	TWEEN 80	Nile red (0.1%)
73	PBCA	153	0.11	-15	Jeffamine M-1000	SDS	Nile red (0.1%)
74	PBCA	684	0.27	-7	OH-PEG-NH_2	SDS	Nile red (0.1%)
75	PBCA	148	0.12	-20	Amino-PEG 750	SDS	Nile red (0.1%)
76	PBCA	140	0.12	-23	Amino-PEG 2000	SDS	Nile red (0.1%)
77	PBCA	138	0.13	-21	Amino-PEG 5000	SDS	Nile red (0.1%)
79	PBCA	189	0.33	-14	Jeffamine M-2070	SDS	Nile red (0.1%)
82	PBCA	178	0.12	-33	Jeffamine M-1000	SDS	Nile red (0.1%) and fluoresceinamine (0.1%)
83	PBCA	182	0.1	-32	Jeffamine M-1000	SDS	Nile red (0.1%) and fluoresceinamine (0.1%)
89	POCA	244	0.36	-32	Jeffamine M-1000	SDS	Nile red (0.1%)

Abbreviations: Polydispersive index (PDI)

of batch 68. Fluoresceinamine is coupled to the surface of the particle. In batch 66, the amine groups on fluoresceinamine are bound to acid groups on the particle surface. For batch 82 and 83, fluoresceinamine is coupled directly onto the surface through the amine groups, which react with the monomer and initiate polymerization. In 82, fluoresceinamine was added to the nanoemulsion before addition of PEG, whereas in 83 fluoresceinamine was added together with the PEG chains. In the dialysis process, fluorescein molecules that became redundant during synthesis will be removed. However, this does not apply for nile red, as it is hydrophobic and will not diffuse as readily into the water phase. Nanoparticle 44 is added 5 times less nile red during synthesis than the other nile red loaded particles.

Measurements show that nile red associated with poly(alkyl cyanoacrylate) particles has an excitation and emission maximum at 540 nm and 600 nm respectively. Fluorescein derivatives have a maximum absorption around 495 nm, and an emission maximum at approximately 520 nm.

3.1.3 PEGylation of nanoparticles

All the nanoparticles are PEGylated, but with chains of different composition and length. Table 3.2 displays the types of PEGs used and a comparison of their approximate molecular weights and number of ethylene oxide units per chain ($N_{EOperPEG}$). The chemical structures of all chains can be found in appendix A. TWEEN 80 serves not only to provide a hydrophilic coating of the nanoparticles, but also as a surfactant to stabilize the miniemulsion. The presence of PEG was confirmed by nuclear magnetic resonance (NMR) measurements performed by postdoc Andreas Åslund, in all batches except 68 and 79, where measurements were not performed.

Table 3.2: Summary of approximate molecular weight and number of ethylene oxide units for the different PEG chains used to coat the nanoparticles.

Name	**PEG type**	**Molecular weight** (Da)	$\mathbf{N_{EOperPEG}}$
Amino-PEG	Methoxypolyethylene glycol amine	750	16
		2000	45
		5000	114
Jeffamine	Polyetheramine	1000	19
		2000	29
OH-PEG-NH_2	Aminopolyethylene glycol	3400	77
TWEEN 80	Polyethylene sorbitol ester	1300	20

3.1.4 Estimation of average PEG chain density on the nanoparticles

Estimation of the average PEG chain density (ρ_{PEG}) on the particle surface was done from NMR measurements. The samples were centrifuged and washed before analysis, in order to remove PEG chains in the solution that was not associated with the particle surface. It was assumed that all measured PEG were on the surface of the particles, and the surface density was defined as the ratio between the total number of PEG chains (N_{PEG}) and the nanoparticle surface area (S_{NP}):

$$\rho_{PEG} = \frac{N_{PEG}}{S_{NP}} \tag{1}$$

The surface area of one nanoparticle is given simply by $S_{NP} = 4\pi r^2$, where r is the particle radius. To estimate N_{PEG} it was necessary to use the NMR data. These measurements give a ratio between the amount of PEG and polymer in the sample:

$$\text{NMR-ratio} = \frac{n_{PEG}}{n_{polymer}} \tag{2}$$

It was further assumed that this ratio also represented the relation between PEG and polymer in one nanoparticle. When placed in a magnetic field, NMR active nuclei absorb electromagnetic radiation. Since the alkyl(cyanoacrylate) monomer contains only one such nuclei, whereas a PEG chain has one per ethylene oxide unit, the NMR-ratio was divided by the number of ethylene oxide units per PEG chain ($N_{EOperPEG}$) to give:

$$\frac{\text{NMR-ratio}}{N_{EOperPEG}} = \frac{n_{EO}}{n_{NP}} \tag{3}$$

The number of mole in one nanoparticle (n_{NP}) was then estimated by assuming that the particle only consists of polymer:

$$n_{NP} = \frac{m_{NP}}{MW_{polymer}} \tag{4}$$

where the mass of one nanoparticle (m_{NP}) was calculated by assuming a particle density equal to water. Following, the number of mole ethylene oxide (n_{EO}) was resolved by using equation 3. This value was multiplied by Avogadro's number to yield the number of ethylene oxide units per particle (N_{EO}). N_{PEG} could then be estimated by dividing N_{EO} by the number of ethylene oxide units for the respective PEG chains:

$$N_{PEG} = \frac{N_{EO}}{N_{EOperPEG}} \tag{5}$$

The PEG density estimation was only done on particles coated with the linear PEG chains, i.e. Amino-PEG, Jeffamine and OH-PEG-NH_2.

From the estimated surface density data it was possible to determine the area occupied by one PEG chain on a particle:

$$A_{PEG} = \frac{S_{NP}}{N_{PEG}} \tag{6}$$

If the surface area covered by one PEG chain is assumed to be a circle, the average distance between two neighboring PEG chains (D) equals the diameter of this circle:

$$D = 2\sqrt{\frac{A_{PEG}}{\pi}} \tag{7}$$

3.1.5 Estimation of PEG surface conformation

Using the model published by de Gennes et al. [123], the PEG surface conformation was determined. If the distance between PEG chains on the surface (D) is larger than the relative polymer size, or Flory radius (R_F), all PEG chains are expected to be present in the mushroom regime, whereas with D smaller than R_F the PEG chains are found in a brush conformation. For cases where D is comparable to R_F, a so called mushroom-to-brush transition regime exists. The Flory radius of a polymer is given by:

$$R_F = aN^{3/5} \tag{8}$$

where a is the monomer length (0.35 nm for PEG [124, 125]) and N is the number of monomer units in the polymer ($N_{EOperPEG}$ for the PEG chains).

3.2 Cell cultivation

PC3 (Prostatic Adenocarcinoma) cells with American Type Culture Collection number CRL-1435 were cultured in monolayer in plastic flasks (nunc) and incubated at 37°C and 5% CO_2. The cell culture medium was Dulbecco's modified eagle medium (Gibco Invitrogen) supplemented with 10% fetal bovine serum (FBS, Sigma Aldrich). Passaging to a new flask was done when the cells were approaching confluency. First, the old growth medium was removed, followed by washing with phosphate buffered saline (PBS, Sigma). After PBS removal, trypsin/EDTA solution (0.25%/0.2%, Sigma Aldrich) was added before incubation at 37°C for 2-3 minutes, allowing the cells to detach. To stop the effect of the enzymes in the trypsin solution, growth medium was added. Following, the cell suspension was centrifuged at 1500 rpm for 5 minutes. Prior to centrifugation, a few drops of cell suspension was added to a Bürker chamber. The chamber was observed in a transmission light microscope and the cells were counted to estimate the cell

concentration. After spin down, the supernatant was discarded and the cell pellet was resuspended in medium. As a last step, an appropriate number of cells were passaged to a new flask.

3.3 Studies of nanoparticle uptake in cells with flow cytometry

FCM analyses were done to investigate the uptake of different nanoparticles in cells. For these experiments, PC3 cells were seeded in 25 cm^2 plastic flasks. In each flask, 1×10^6 cells/5 ml medium were allowed to adhere and grow for 48 hours before the experiment, or 2×10^6 cells/5 ml medium 24 hours in advance.

3.3.1 Incubation of cells with nanoparticles

On the day of the experiment, the old medium was discarded and 5 ml of nanoparticle-medium solution, with a concentration of 20 µg/ml, was added to each flask. This value was chosen since previous studies showed minimal reduction in viability of PC3 cells after addition of similar PBCA nanoparticles at this concentration. [126] Incubation was done at 37°C and 5% CO_2 for 3 hours. To assess whether the uptake was energy dependent or not, cells with nanoparticles were also incubated at 4°C. After incubation, the nanoparticle-medium solution was removed, and the cells were rinsed with 3 ml of PBS, 3 times per flask. The cells were then detached by adding 1 ml trypsin/EDTA solution and kept at 37°C for 2-3 minutes. To stop the trypsination process, 7 ml growth medium was added. The added medium was cold in order to stop the cells' metabolism before FCM analysis. Subsequently, the resulting cell suspension from one flask was transferred to 4 centrifuge tubes, 2 ml in each. 3 of these tubes were then centrifuged at 1000 rpm for 3 minutes, 1, 2 and 3 times respectively. The purpose was to assess whether more extensive washing of the samples would affect the fluorescence intensity by collecting one sample from each step in the washing procedure. One flask incubated with nanoparticles would therefore yield 4 samples for FCM analyses:

- 3 times rinsed with PBS
- 3 times rinsed with PBS, centrifuged at 1000 rpm for 3 minutes
- 3 times rinsed with PBS, centrifuged 2 times at 1000 rpm for 3 minutes
- 3 times rinsed with PBS, centrifuged 3 times at 1000 rpm for 3 minutes

Control samples with no nanoparticles added were also analyzed.

Awaiting FCM analyses, the samples were kept dark to prevent photobleaching and on ice to inhibit further energy dependent uptake. The analyses were performed as soon as sample preparation was finalized, in order to minimize possible diffusion of the fluorescent marker. Approximately 1 ml of cell suspension was transferred to each FCM tube.

3.3.2 Flow cytometry setup

Analyses of samples were performed in a Gallios flow cytometer (Beckman Coulter). A total of 10.000 cells were counted from each sample, or the data collection was aborted after analyzing the sample for 300 seconds. By plotting the forward scatter signal against the side scatter signal in a dot plot, a collection gate was established to exclude cell debris and clusters. From these events, a single parameter histogram of counts versus fluorescence intensity was obtained. Control samples were analyzed to exclude the autofluorescence contribution. In the histogram described above, when analyzing untreated cells, the peak should be within the first decade on the x-axis. All events with higher fluorescence intensity than a boundary line set to include 3% of the cells in the control sample were defined as positive.

Depending on which fluorochrome the nanoparticles were labeled with, different lasers and detectors were utilized. Nile red was excited with a green laser of wavelength 561 nm and detected through a 582 nm filter with a 15 nm band pass, and a 620 nm filter with a 30 nm band pass. Fluorescein acrylate and fluoresceinamine was excited with a blue laser of wavelength 488 nm and detected through a 525 nm filter with a 40 nm band pass.

Two different measures of positive cells were estimated from the samples:

1. The percentage of positive cells in the sample defined by the boundary line.
2. The relative amount of positive cells estimated by normalizing the MFI from the samples to the MFI from untreated cells (corresponding to the autofluorescence).

The Kaluza software from Beckman Coulter was used for data analysis, and to acquire overlays of histograms.

3.4 Investigation of intracellular nanoparticle distribution with CLSM

The intracellular distribution of nanoparticles was studied with CLSM. For these experiments, PC3 cells were grown in µ-slide 8-well plates (Ibidi, Thistle Scientific). In each well, 15.000 cells/300 µl medium were seeded 48 hours before the experiment, or 30.000 cells/300 µl medium 24 hours in advance. On the day of the experiment, the growth medium was removed, and 300 µl of nanoparticle-medium solution (20 µg/ml) was added. Incubation was done at 37°C and 5% CO_2 for the desired period of time, usually approximately 1 hour.

Observation of the samples was done in a TCS SP8 from Leica. Excitation of both nile red and fluorescein dyes was done with an argon laser with wavelength of 488 nm. The water objective used had a magnification of 63X and a numerical aperture of 1.2, and the confocal pinhole size was set to 1 airy unit. Images were taken with a frame size of 1024×1024 pixels and a scan speed of 400 Hz. To achieve maximum signal with minimal saturation and background disturbance the laser intensity and gain was adjusted to an optimal level.

To investigate whether the spectral characteristics of nile red could be exploited to distinguish between free and particle associated nile red in cells, λ-series were recorded. The sample was illuminated with the 488 nm laser, and nile red emission was detected in 11 wavelength intervals between 520 and 700 nm. Following, different regions of interest in the cells were defined, namely apparent vesicles and cytosolic regions. The intensity values from each such region were collected at every wavelength interval. These data were subsequently used to obtain the nile red emission spectra from vesicles and cytosolic regions of the cells after nanoparticle incubation. In addition, a tunable white laser was used to vary the excitation wavelength in order to measure the excitation maximum in similar regions of interest.

3.5 Quantification of nile red amount by spectrophotometry

3.5.1 Total nile red content in the particles

The total nile red content in the nanoparticles was measured to determine how it correlated with the theoretical value. By dissolving the poly(alkyl cyanoacrylate) particles in tetrahydrofuran (THF), all encapsulated nile red should in theory be released to the solution. 50 µl nanoparticle solution was added to 2 ml THF, before

the mixture was stirred on a roller. Samples were measured in a spectrophotometer both after 4 and 24 hours, to make sure all nanoparticles were properly dissolved. In addition, a nanoparticle without encapsulated nile red was added to THF, in order to rule out possible contribution from polymeric residues.

3.5.2 Nile red release from nanoparticles in cell medium

Experiments were performed to determine whether nile red was released from the nanoparticles and into cell medium. A nanoparticle-medium solution with the same concentration used for cell incubation (20 µg/ml) was added to 25 cm^2 plastic flasks and incubated at 37°C and 5% CO_2 for 3 hours. After incubation, the samples were centrifuged at 21.000 rpm (approximately 50.000g) for 1.5 hours in a Beckman Coulter Avanti J-30I. The centrifugation speed and time were chosen since it has previously been used to sediment similar PBCA nanoparticles. [127] Following centrifugation, sedimented nanoparticles were visible in the bottom of the centrifuge tubes. If free nile red was present in the original nanoparticle solution, or if parts of the fluorescent dye were released from the particles, nile red would now be found in the supernatant. The supernatants from all centrifuged solutions were collected and stored frozen until further use.

The nile red probe is efficiently quenched in aqueous solution, and therefore nile red in the supernatant cannot be measured directly in a spectrophotometer. To extract nile red from the cell medium, 1 ml of hexadecane was added to 3 ml of the collected supernatants. Pure cell medium was also added to hexadecane, in order to rule out possible contribution from components of the medium. These mixtures were let to stay overnight on a roller. Next morning, the hexadecane phases were collected for measurements.

3.5.3 Spectrophotometric measurements of nile red in the samples

A standard curve of nile red concentration versus fluorescence intensity was obtained to quantify the amount of nile red in the samples. The standard curve was generated by measuring the fluorescence intensity of solutions with known nile red concentrations, ranging from 1 to 100 ng/ml. Since two different solvents were used (hexadecane and THF), standard curves of nile red dissolved in each of these had to be measured. Following, the data set was fitted to a linear model in Excel (Microsoft Office). The line was set to begin at the origin, as zero concentration of nile red was assumed to give no fluorescence. (Any solvent contribution is excluded by using hexadecane/nile red as blank samples.)

Measurements of the samples were done in a spectrophotometer (Gemini XPS Fluorescence Microplate Reader, Molecular Devices). 200 µl solution was transferred into a white 96-well plate, before the fluorescence intensity was recorded. 2-3 parallels were measured from each concentration, and pure hexadecane/THF was used as a blank sample to correct for contributions from the solvent. For nile red dissolved in hexadecane, an excitation wavelength of 493 nm and emission wavelength of 540 nm was used. These wavelengths were chosen since they corresponded approximately to the highest point on the absorbance and emission spectra of nile red dissolved in hexadecane. From measurements of absorbance and emission spectra of nile red dissolved in THF, an excitation and emission wavelength of 527 nm and 603 nm were chosen.

The same protocol as described above was used for measuring the fluorescence intensity of samples collected from the dissolved nanoparticles and the supernatants.

3.6 Toxicity studies

The cytotoxicity of poly(alkyl cyanoacrylate) nanoparticles was measured using alamarBlue® cell viability assay from Invitrogen. (See section 2.2.1) 24 hours prior to the experiment, 20.000 cells/200 µl medium were seeded in each well of a black 96 well plate (Corning®), with flat and clear bottom.

On the day of the experiment, the growth medium from all wells was discarded. The cells were then incubated with nanoparticle-medium solutions with 10 different concentrations, increasing from 5 to 240 µg/ml, at 37°C and 5% CO_2 for 3 hours. The purpose was to examine how the cytotoxicity was affected by nanoparticle concentration, and also if it varied with different PEGylation and monomer composition. 4 replicas were used for each sample, including the control samples with no added nanoparticles. After incubation, the cells were rinsed 3 times with 200 µl cell medium per well, before each well was added 110 µl of alamarBlue® reagent diluted 10 times in medium. Subsequently, the well plates were put back into the incubator (37°C, 5% CO_2). An incubation time of 3 hours was chosen since previous toxicity studies of similar poly(alkyl cyanoacrylate) nanoparticles added to PC3 cells showed that the fluorescence intensity of alamarBlue® increased linearly with incubation time between 2 to 4 hours. [126] Blank samples containing only cell medium and alamarBlue® reagent were also prepared in order to correct for background fluorescence from the medium. To eliminate possible fluorescence contribution from phenol red, the cell medium used in the toxicity experiments did not contain this pH indicator.

The fluorescence intensity of alamarBlue® was recorded using a microplate reader

(Tecan Group Ltd.), with measurements done from the bottom with excitation and emission wavelengths of 550±9 nm and 590±20 nm respectively. Since the amount of fluorescence is proportional to the number of living cells, an estimation of the percentage of viable cells can be done with the equation below:

$$\text{Cell viability } (\%) = \frac{(FI_{NP} - FI_B)}{(FI_C - FI_B)} \times 100, \tag{9}$$

where FI_{NP}, FI_C and FI_B are the fluorescence intensity from samples with added nanoparticles, untreated controls and blank samples respectively. These data were then used to plot cell viability against nanoparticle concentration on a logarithmic axis. The resulting dose response curve was fitted using Sigmaplot to a 4-parameter logistic curve given by:

$$y = y_{min} + \frac{(y_{max} - y_{min})}{[1 + (\frac{x}{EC_{50}})^{-Hill\ slope}]}, \tag{10}$$

where EC_{50} denotes the half maximal effective concentration, the $Hill\ slope$ characterizes the slope of the curve at its midpoint, and y_{max} and y_{min} are the top and bottom of the curve respectively. y_{max} was constrained to be smaller than or equal to 100% and y_{min} larger than or equal to 0%. The goodness of the fit was determined by the coefficient of determination (R^2) and the p-value of each coefficient. P-values smaller than 0.05 were considered to indicate that the curve was a good approximation to the data points.

From the dose response curves, two measures of nanoparticle cytotoxicity were obtained:

1. The median lethal dose (LD_{50}) is defined as the concentration required to kill half of a tested population after a specified test duration. This value was determined by reading out at which concentration the 50% cell viability point intercepts with the graph.

2. The EC_{50} parameter defines the nanoparticle concentration that provokes a response midway between the baseline (y_{min}) and maximum (y_{max}) response. This value can be compared between experimental data independent on how your data are normalized, i.e. even if the baseline and maximum level of cell viability differs a lot between the tested nanoparticles.

4 Results

4.1 Estimates of PEG chain densities

An estimate of the average PEG chain density on the surface of nanoparticles coated with linear PEGs was performed by the procedure outlined in section 3.1.4. In table 4.1, the resulting estimates of PEG density (ρ_{PEG}), average area occupied by one PEG chain (A_{PEG}) and average distance between neighboring PEG chains (D) are presented.

Table 4.1: Estimated PEG surface densities (ρ_{PEG}) on the different nanoparticle batches, including approximate values for the surface area covered by one PEG chain (A_{PEG}) and the average distance between neighboring chains (D). The estimates are based on data obtained in NMR measurements.

PEG	**Batch**	$\rho_{\mathbf{PEG}}$ (nm^{-2})	$\mathbf{A_{PEG}}$ (nm^2)	**D** (nm)
Jeffamine 1000	44	0.03	36.0	6.8
	66	0.03	39.9	7.1
	69	0.04	25.5	5.7
	73	0.02	43.4	7.4
	82	0.03	31.0	6.3
	83	0.04	25.0	5.6
	89*	0.06	15.7	4.5
Amino-PEG 750	75	0.03	37.7	6.9
Amino-PEG 2000	76	0.01	114.4	12.1
Amino-PEG 5000	77	0.003	401.5	22.6
OH-PEG-NH_2 3400	74	0.02	57.3	8.5

*Particle produced from POCA.

All particle batches PEGylated with Jeffamine 1000 have comparable PEG density values, except the POCA particle which has a twice as high PEG density on the surface. Various amounts of PEG per gram oil phase are used during synthesis of the different particles, giving no indication that the amount of PEG added influence the PEG density. The results suggest that a change in particle composition from PBCA to POCA can be of significance for the achievable PEG density.

The Amino-PEGylated nanoparticles have an evident decrease in PEG density with increasing PEG chain length, meaning the average distance between neighboring PEG chains are significantly larger for the long PEG chain than for the short. The same number of PEG chains, i.e. equal amounts of mole PEG was

added during synthesis of the particles, suggesting that longer PEG chains result in lower surface density. Particle batch 74, coated with OH-PEG-NH_2, has a twice as high surface density as the particle coated with a PEG chain of similar length (batch 76), possibly because both the hydroxyl and the amino group can react with the monomer.

4.1.1 Expected PEG surface conformation

All particle batches were expected to have their PEG chains in a mushroom conformation. (See table 4.2) In other words, the relative polymer size, or Flory radius (R_F), of all PEG chains were smaller than the average distance between two neighboring PEGs on the surface. This implies that all utilized particles have relatively low PEG surface density, independent of the number of PEG chains attached to the surface and the PEG chain molecular weight.

Table 4.2: The Flory radius (R_F) of the different PEG chains, and the expected PEG surface conformations on all nanoparticle batches.

PEG	**R_F** (nm)	**Batch**	**PEG conformation**
Jeffamine 1000	2.1	44	Mushroom
		66	Mushroom
		69	Mushroom
		73	Mushroom
		82	Mushroom
		83	Mushroom
		89*	Mushroom
Amino-PEG 750	1.9	75	Mushroom
Amino-PEG 2000	3.4	76	Mushroom
Amino-PEG 5000	6.0	77	Mushroom
OH-PEG-NH_2 3400	4.7	74	Mushroom

*Particle produced from POCA.

4.1.2 Correlation between PEG chain density and ζ-potential

The correlation between PEG density and ζ-potential for the particles are not as expected. Rather counterintuitive, the plot in figure 4.1 shows that particles with the most positive ζ-potentials have PEG densities in the lower range of the estimated values. This relation holds even if the fluorescein labeled particles are disregarded, in case association with fluorescein alters the surface properties in comparison with nile red loaded particles. The result suggests that an increase in ζ-potential cannot directly be taken as an indication on higher PEG density on the surface, exemplified by how the particle with the highest PEG density (the POCA particle), also has one of the most negative ζ-potentials measured.

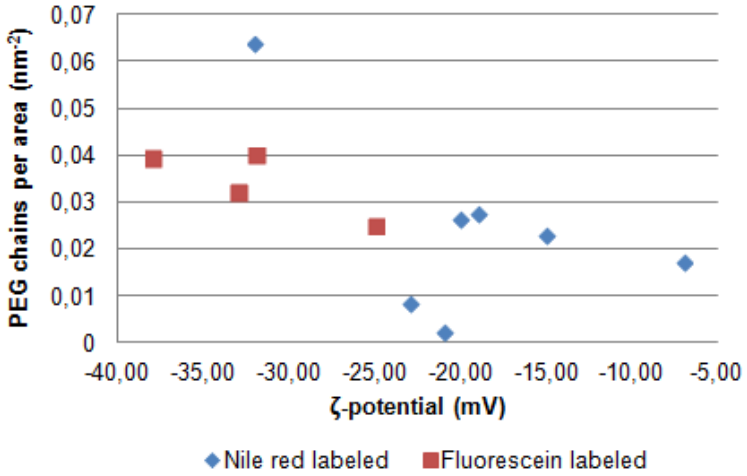

Figure 4.1: Correlation between measured ζ-potential and estimated density of PEG chains on the particle surface. The data points are labeled according to the fluorescent label of the nanoparticles: nile red (blue) and fluorescein (red). The y-axis represents PEG density expressed as number of PEG chains per nm^2, and the x-axis displays the ζ-potential in mV.

4.2 Cellular uptake of fluorescein-labeled nanoparticles

Experiments performed in the project thesis showed that nile red could be dissociated from the nanoparticles. New batches labeled with fluorescein dyes were therefore prepared to determine whether the fluorescent marker remained associated with the particles after washing of the samples and if the cellular uptake was energy dependent or not.

4.2.1 Cellular uptake of fluorescein acrylate nanoparticles

After experiments performed with fluorescein acrylate nanoparticles it was found that the labeling protocol was not satisfactory. Figure 4.2 shows overlay histograms from FCM analyses of cells incubated with particles with encapsulated fluorescein acrylate. The results after testing with particle 68 indicate that fluorescein acrylate can dissociate from the nanoparticles, since the fluorescence intensity from the samples does not differ between cells incubated at 4°C and 37°C (Figure 4.2a), suggesting energy independent uptake based on diffusion of the fluorescent marker into cells rather than endocytosis of the particles. It is also probable that small amounts of fluorescein acrylate remained associated with the particles after synthesis, since the MFI only was about 3 times higher than that of the control samples, corresponding to a very slight increase. After incubation with particle 69 (Figure 4.2b) it is not possible to discriminate between cells incubated with particles and untreated cells, giving no indication on either endocytosis of nanoparticles or diffusion of fluorescein acrylate into cells. This result can be explained with a high degree of fluorescein acrylate leakage during dialysis, meaning very little fluorescein acrylate remained in the core of the particle after synthesis.

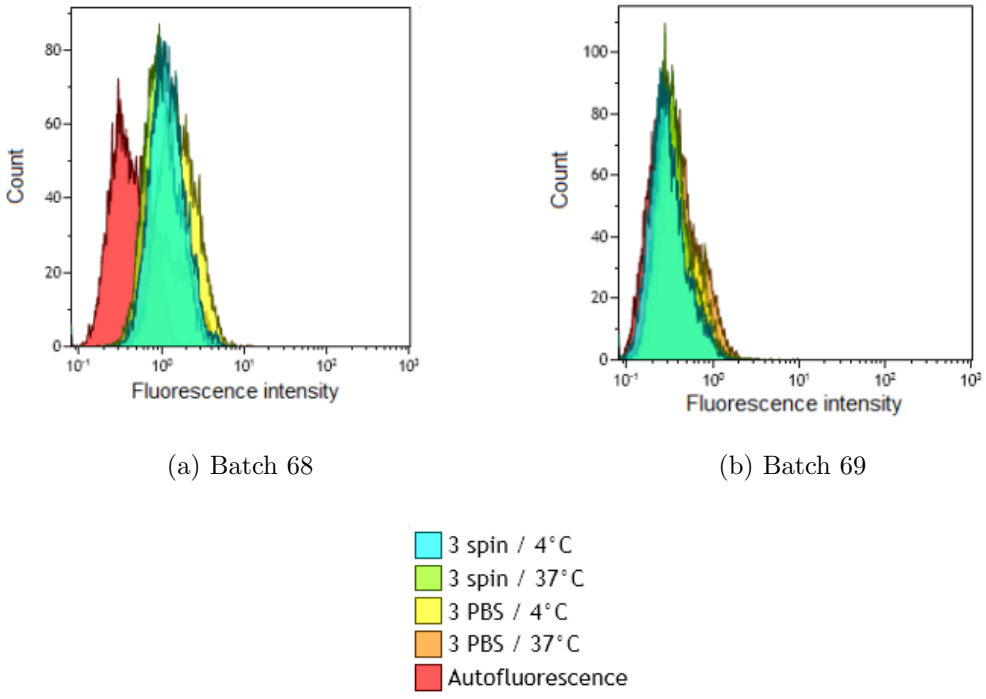

(a) Batch 68

(b) Batch 69

Figure 4.2: Overlay histograms obtained in FCM analyses of PC3 cells incubated with fluorescein acrylate labeled nanoparticles for 3 hours at 37°C and 4°C respectively. The fluorescence intensity is shown both after 3 times rinsing with PBS, and after additional 3 times centrifugation.

4.2.2 Cellular uptake of fluoresceinamine nanoparticles

None of the procedures for labeling nanoparticles with fluoresceinamine was found to be optimal. Figure 4.3 shows overlay histograms from FCM analyses of cells incubated with particles that had fluoresceinamine coupled to the surface. The first testing of particle batch 66 gave promising results since the cellular uptake seemed to be energy dependent. (Histogram shown in appendix figure B.1) Still, the MFI of cells incubated with nanoparticles was only about twice as high as the untreated cells, meaning very little fluoresceinamine was associated with the particle after synthesis. Therefore, the particle batch was modified by adding 10 times more fluoresceinamine, with the resulting overlay histogram presented in figure 4.3a. From the histogram, this particle looks like an ideal candidate for further studies. The cellular uptake is clearly energy dependent and does not diminish with more extensive washing of the samples. Unfortunately, after attaching more fluoresceinamine to the surface, the particles became very unstable and suffered from severe problems with aggregation. This was observed in the CLSM, when cells appeared all black, but big, bright spots of fluorescence could be observed on the cell membrane and in the surrounding medium after particle incubation. (Figure B.2 in appendix.) Aggregation of the particles was also confirmed by dynamic light scattering measurements; after modification the size increased from 150 nm to 2.8 μm.

After experiments performed with batch 82 and 83, both particles were found to have non-detectable amounts of fluoresceinamine coupled to the surface, i.e. similar results were obtained as with the fluorescein acrylate labeled particle batch 69. It was not possible to distinguish between untreated cells and cells incubated with nanoparticles (see figure 4.3b and 4.3c), indicating neither endocytosis of nanoparticles nor diffusion of fluoresceinamine into cells. This can be explained with observations done during synthesis: The amine group on fluoresceinamine was supposed to be coupled directly onto the surface of the particle by initiating the polymerization, but instead the reaction was too rapid and destabilized the miniemulsion, leading to separate, solid lumps of fluoresceinamine and little or nothing remaining on the particle surface.

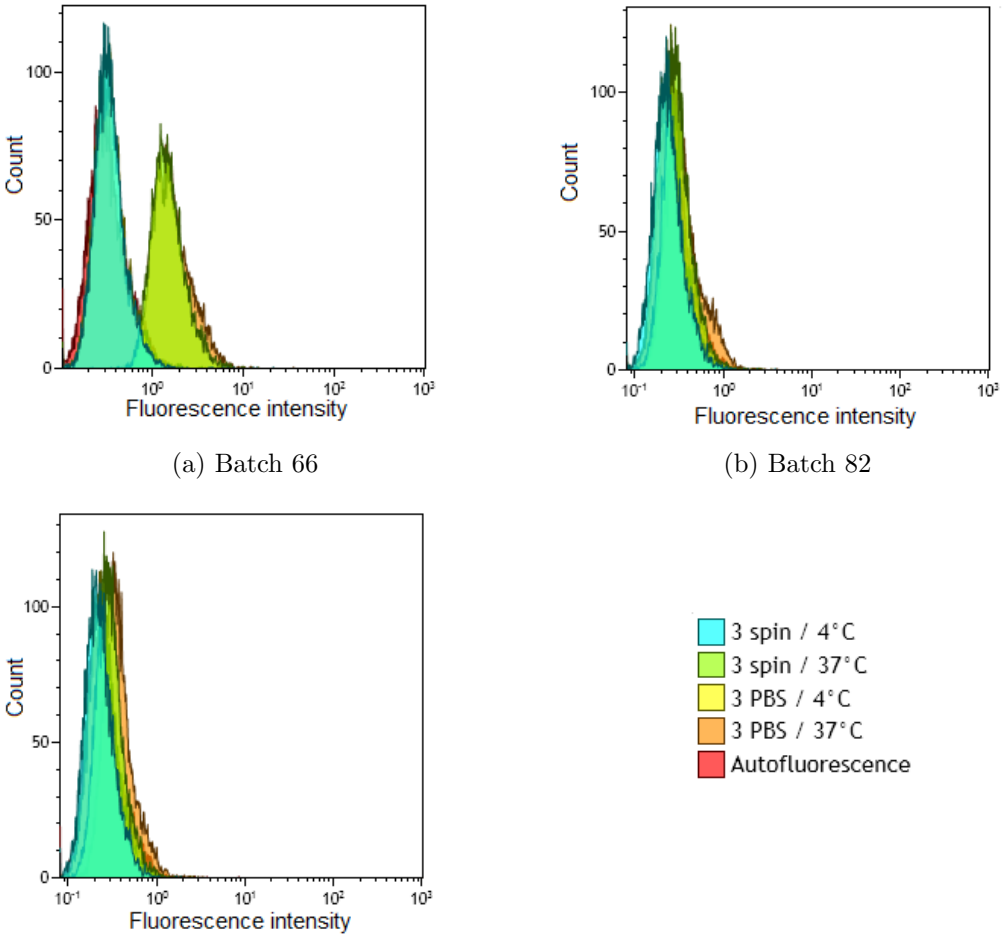

(a) Batch 66

(b) Batch 82

(c) Batch 83

Figure 4.3: Overlay histograms obtained in FCM analyses of PC3 cells incubated with the fluoresceinamine labeled nanoparticles for 3 hours at 37°C and 4°C. Batch 66 is modified from the original by attaching 10 times more fluoresceinamine to the particle surface. The fluorescence intensity is shown both after 3 times rinsing with PBS, and after additional 3 times centrifugation.

4.3 Effects of washing on nile red positive cells

Washing reduces the amount of nile red fluorescence from the samples. This phenomenon was first discovered in the project thesis, and further confirmed by experiments done in this work. Figure 4.4 demonstrates how the MFI of cells after incubation with various nanoparticles for 3 hours is influenced by the different steps of washing, and with a representative histogram presented in figure 4.5. The trend of decreasing fluorescence intensity with more extensive washing is valid for all the nile red labeled nanoparticle batches tested.

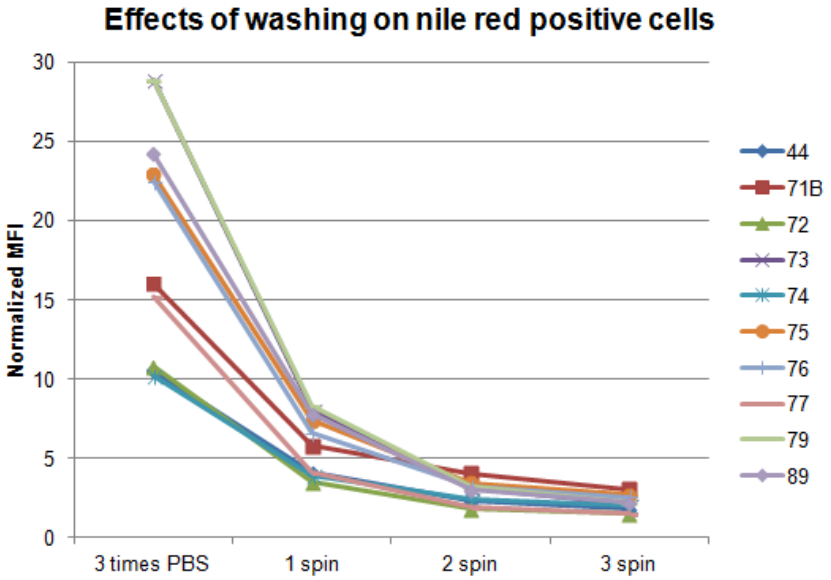

Figure 4.4: PC3 cells positive for nile red after 3 hours incubation with all nile red labeled nanoparticles. The MFI normalized to the MFI of untreated cells is plotted as a function of the different steps of washing: 3 times rinsing with PBS, 1, 2 and 3 times spin down.

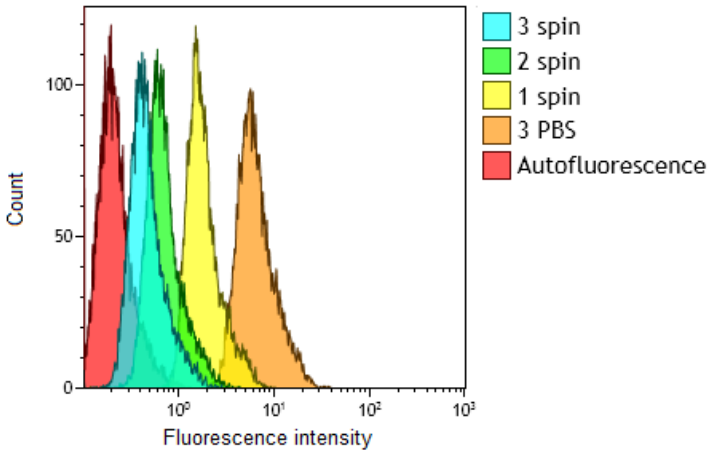

Figure 4.5: Overlay histogram obtained in FCM analysis of PC3 cells incubated with nanoparticle batch 73 for 3 hours at 37°C. The fluorescence intensity is shown after all steps of washing: 3 times rinsing with PBS, 1, 2 and 3 spin downs, and is representative for the trend observed with all other nile red labeled nanoparticle batches.

4.4 Cellular uptake of nile red loaded nanoparticles

To investigate whether the cellular uptake of nanoparticles with encapsulated nile red was dependent on different particle properties, some candidates were chosen for further comparison. The particle batches 71B, 72 and 74 were eliminated because they were found to be relatively unstable and had much bigger sizes (from approximately 400 to 800 nm) than what was desired. Batch 82 and 83 were also left out since they were labeled with fluoresceinamine in addition to nile red, something which could affect the surface properties of the particles. The remaining particle batches (44, 73, 75, 76, 77, 79 and 89) were classified according to their PEGylation: Jeffamine or Amino-PEG. Only these 7 particles are further investigated in the thesis, and to make it easier for the reader, the particle batches will from now on be referred to according to their properties. They are given names on the form: B/O-JF/AMXXXX; the first letter representing monomer composition (B for butyl and O for octyl), the PEG chain type after the hyphen (JF for Jeffamine and AM for Amino-PEG), and at last the PEG chain length as molecular weight. Particle batch 44 (B-JF1000-Hex) is distinguished from 73 by (B-JF1000) by adding "Hex" to the name to account for the use of hexadecane and not Miglyol as co-stabilizer.

In all FCM experiments, nile red fluorescence was detected in two channels. Both channels showed similar fluorescence patterns, but since the intensity was strongest in the 620 nm filter, only data from this spectral interval are presented in the following sections. A comparison of the fluorescence intensity from the two channels are given in appendix C.

4.4.1 Cellular uptake of Jeffamine PEGylated nanoparticles

Nile red is transferred to a high degree into PC3 cells from Jeffamine PEGylated nanoparticles. In figure 4.6, a comparison of the cellular uptake after 3 hours incubation with the Jeffamine PEGylated particles is presented, and overlay histograms are given in figure 4.7. The particles differ a bit in how much nile red they are able to deliver to cells (demonstrated by differences in normalized MFI after 3 times rinsing with PBS), although here it is important to note that B-JF1000-Hex has 5 times less nile red encapsulated, such that the fluorescence intensity values resulting from this particle are not directly comparable to the others. An increase in PEG chain length from 1000 to 2000 Da (compare B-JF1000 and B-JF2000) gave no difference in cellular uptake, whereas the POCA particles (O-JF1000) seem to have a slightly lower ability to deliver nile red to cells than its PBCA counterpart (B-JF1000).

The process of nile red transfer is mainly energy independent, since incubation with nanoparticles give comparable cellular uptake at 37°C and 4°C. Slightly more nile red is transferred to cells at 37°C, but after washing the amount of nile red fluorescence is reduced to values close to that of the control samples, indicating no or very little energy dependent uptake. The nile red fluorescence intensity is reduced by similar amounts from cells incubated at both temperatures. This is observed in the overlay histograms (figure 4.7), where the histogram peaks, although initially located at different intensity values, are shifted by similar amounts to lower intensity with washing.

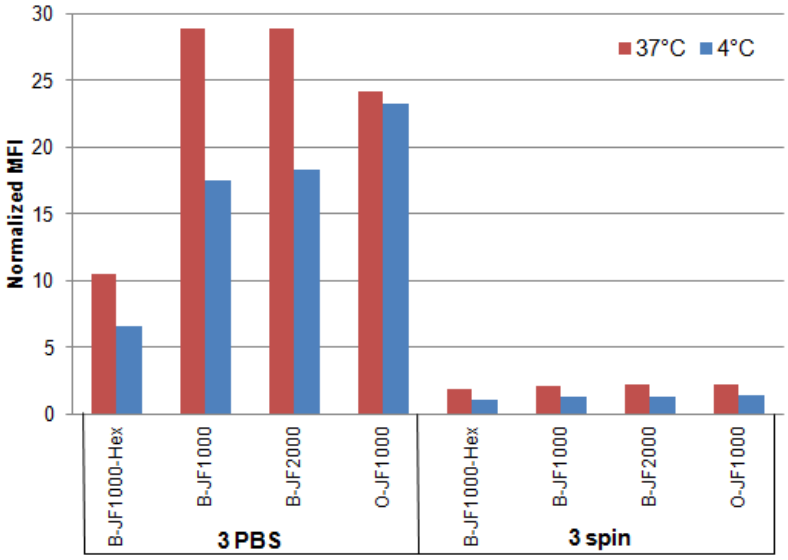

(a) Nile red MFI after Jeffamine nanoparticle incubation

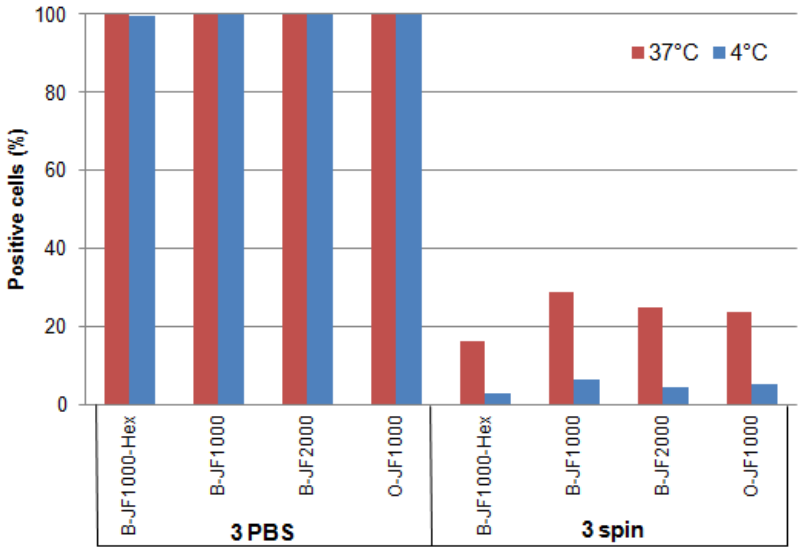

(b) Nile red positive cells after Jeffamine nanoparticle incubation

Figure 4.6: PC3 cells positive for nile red after 3 hours incubation at 37°C (red bars) and 4°C (blue bars) with Jeffamine PEGylated nanoparticles. The MFI normalized to the MFI of control samples is presented in (a) and the percentage of positive cells in (b). All data are shown both after 3 times rinsing with PBS (left side of the chart), and after additional 3 times centrifugation (right side of the chart).

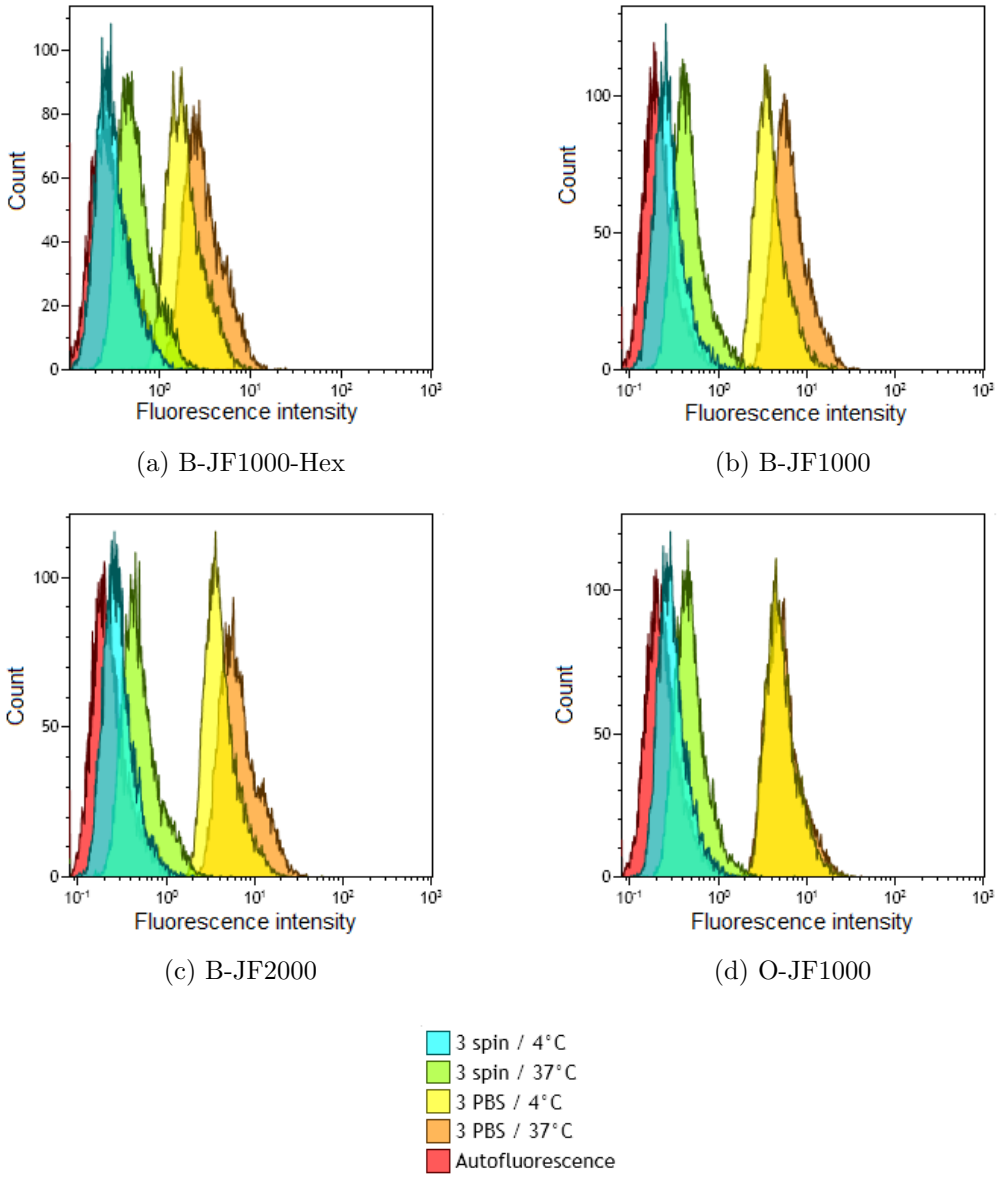

(a) B-JF1000-Hex

(b) B-JF1000

(c) B-JF2000

(d) O-JF1000

Figure 4.7: Overlay histograms obtained in FCM analysis of PC3 cells incubated with Jeffamine PEGylated nanoparticles for 3 hours at 37°C and 4°C. The fluorescence intensity is shown both after 3 times rinsing with PBS, and after additional 3 times centrifugation.

4.4.2 Cellular uptake of Amino-PEGylated nanoparticles

Amino-PEGylated nanoparticles are able to deliver high amounts of nile red to PC3 cells, just like the Jeffamine PEGylated. Figure 4.8 shows a comparison of cellular uptake after 3 hours incubation with the Amino-PEGylated nanoparticles, and overlay histograms are given in figure 4.9. A decrease in cellular uptake with increasing PEG chain length is observed (decreasing normalized MFI from B-AM750 to B-AM5000 after 3 times rinsing with PBS, figure 4.8a) After additional 3 times centrifugation, this trend is no longer visible, since all MFI values are diminished down to a level comparable to that of the control samples.

The transfer of nile red into cells is relatively independent of temperature. More nile red is delivered to cells at 37°C, but after washing the fluorescence intensity is considerably reduced, indicating no or little energy dependent uptake. The difference in cellular uptake at 37°C and 4°C is more prominent when examining the percentage of positive cells (figure 4.8b), although it is not the case for cells incubated with B-AM5000. Washing reduces the nile red fluorescence intensity by similar amounts from cells incubated at both temperatures. This is observed in the overlay histograms (Figure 4.9), where the histogram peaks, although initially located at different intensity values, are shifted by similar amounts to lower intensity with washing.

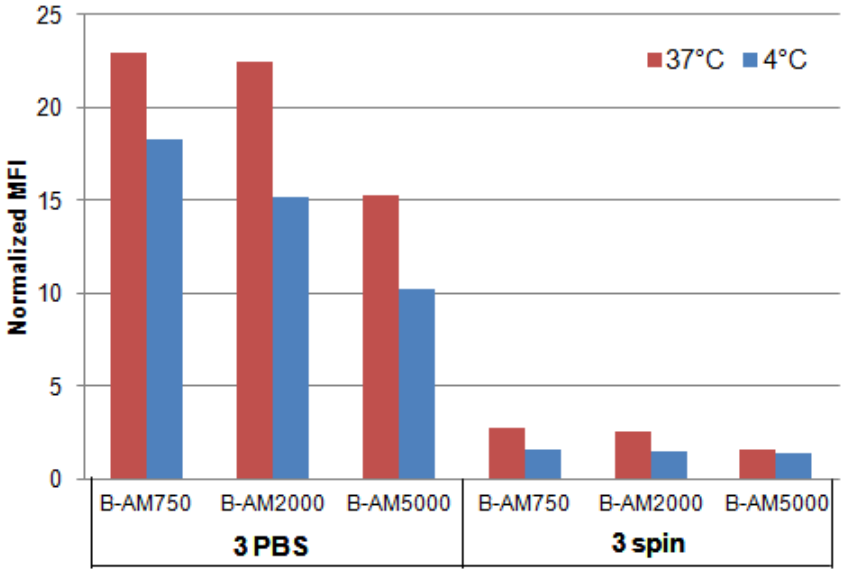

(a) Nile red MFI after Amino-PEG nanoparticle incubation

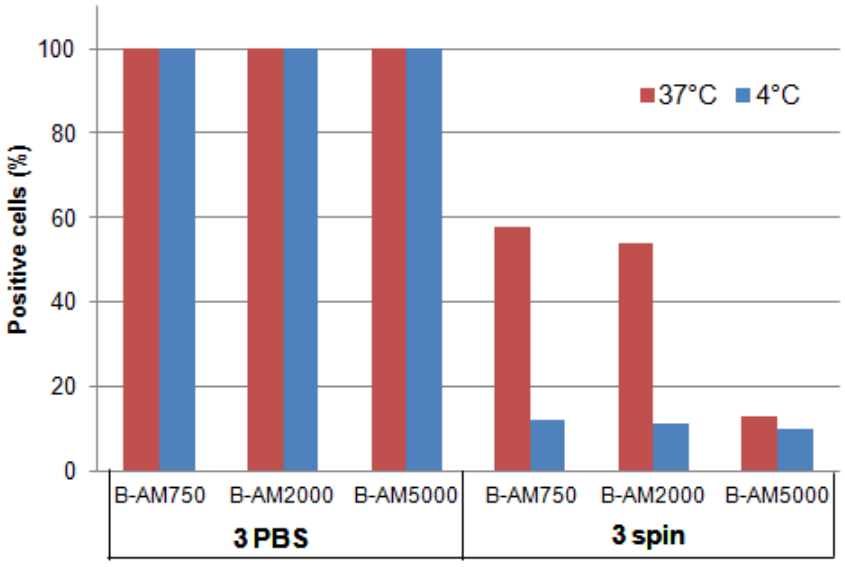

(b) Nile red positive cells after Amino-PEG nanoparticle incubation

Figure 4.8: PC3 cells positive for nile red after 3 hours incubation at 37°C (red bars) and 4°C (blue bars) with Amino-PEGylated nanoparticles. The MFI normalized to the MFI of control samples is presented in (a) and the percentage of positive cells in (b). All data are shown both after 3 times rinsing with PBS (left side of the chart), and after additional 3 times centrifugation (right side of the chart).

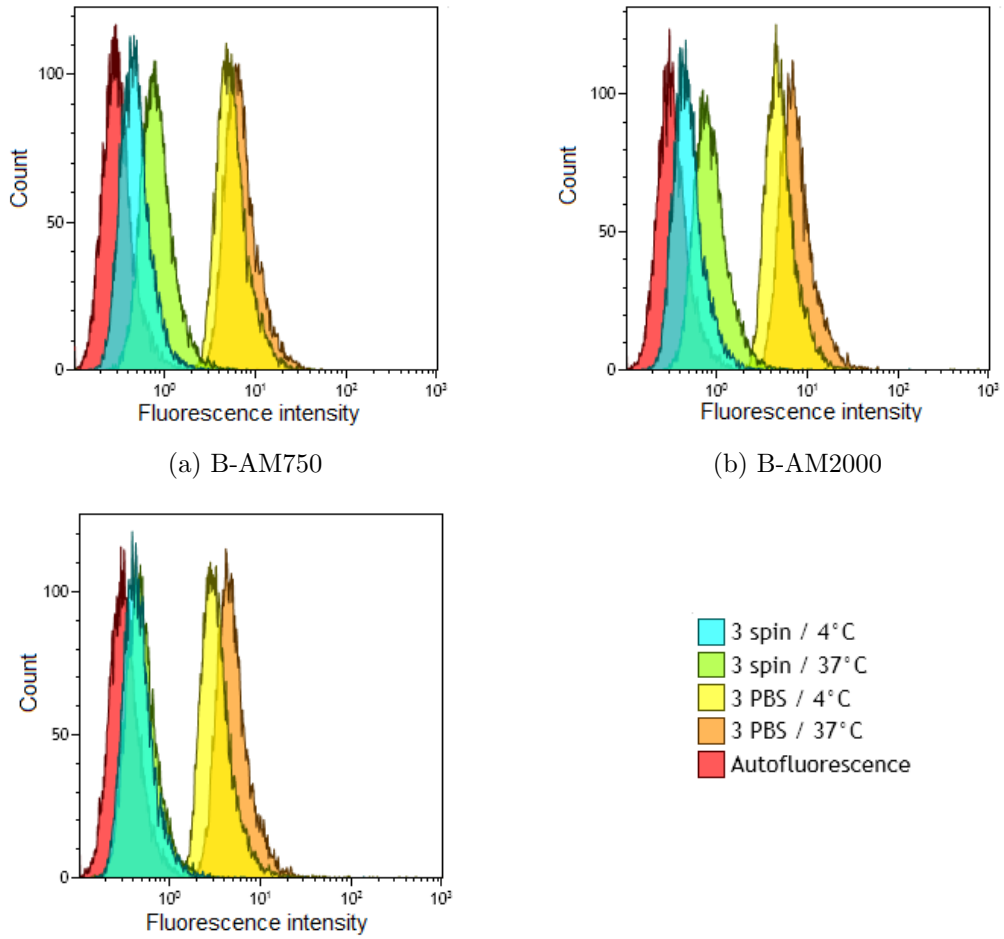

(a) B-AM750

(b) B-AM2000

(c) B-AM5000

Figure 4.9: Overlay histograms obtained in FCM analysis of PC3 cells incubated with Amino-PEGylated nanoparticles for 3 hours at 37°C and 4°C. The fluorescence intensity is shown both after 3 times rinsing with PBS, and after additional 3 times centrifugation.

4.5 Intracellular distribution of nile red after nanoparticle incubation

To complement the uptake studies, CLSM images were taken to examine the intracellular distribution of nile red after nanoparticle incubation. One image, taken after incubation with B-JF1000-Hex, is shown in figure 4.10. From this image, there is no doubt that the fluorescence is intracellular in origin, and no evidence of surface bound particles was found in any of the experiments. Nile red fluorescence was seen both as a diffuse staining of the entire cell cytoplasm and as localized, brighter spots. Not all cells showed as distinct and high-intensity spots as the two cells showed in this figure, and the number of spots also varied between cells within one sample. The presence of localized spots can indicate nanoparticles in vesicles after endocytosis, but it can also be free nile red staining lipid compartments in the cells. Further CLSM studies were therefore performed to see if the spectral characteristics of nile red could be used to distinguish between free and particle associated nile red.

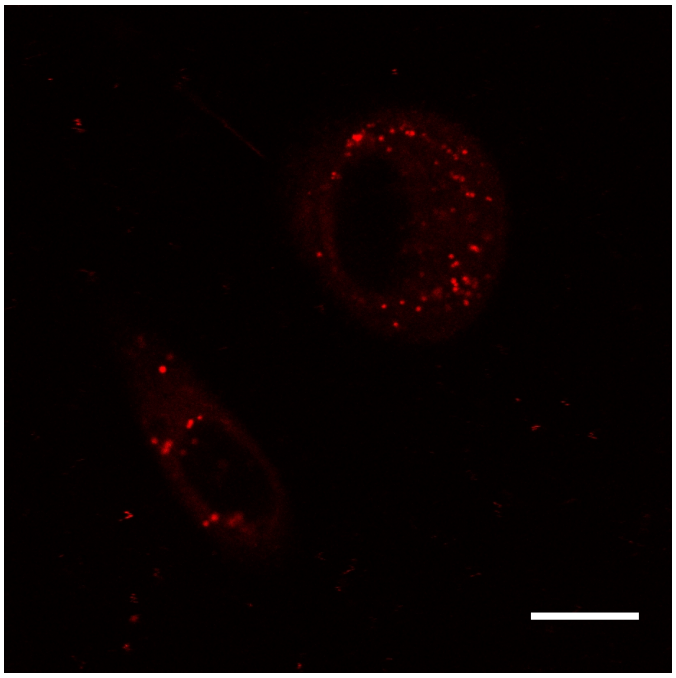

Figure 4.10: CLSM image of PC3 cells incubated with B-JF1000-Hex. Nile red fluorescence is depicted in red. The scale bar is 15 μm.

4.5.1 Spectral analysis of nile red

λ-series were recorded in the CLSM to determine whether the nile red emission spectrum varied between areas in the cytosol and what appeared as vesicles in the imaged cells. The spectral analysis of cells incubated with nanoparticles suggested that nile red in localized spots is bound to more hydrophobic compounds than in the diffuse staining of the cytosol. Figure 4.11b shows a representative CLSM image after incubation with B-JF1000-Hex for approximately 1 hour, where examples of both a cytosolic and vesicular region of interest are given. The resulting emission spectra obtained from these regions are displayed in figure 4.11a, where a nanoparticle spectrum measured in a spectrophotometer is added for comparative purposes as well. The measured emission maximum of the vesicle and cytosol spectrum is at 584 and 616 nm respectively. This indicates that nile red in vesicles is bound to more hydrophobic compounds than in the cytosol. The nanoparticle spectrum has an emission maximum at approximately 595 nm, closer to the vesicle peak than the cytosolic peak.

A similar study was done after 1 hour incubation with particle B-JF1000, with results presented in figure 4.12. The measured emission maxima were the same as for particle B-JF1000-Hex, but the spectrum from the vesicle region is wider and with a less defined peak. When the sample was examined in the CLSM, the vesicles appeared less visible than in images of cells incubated with B-JF1000-Hex, which made it more difficult to define accurate vesicular regions of interest. This may have caused the broadening of the spectrum towards higher wavelengths, since areas in the cytosol may have contributed in the collected intensity values. In general, the process of defining vesicular regions of interest was complicated by vesicle movement during recording of the λ-series. Despite this, the results confirmed that nile red in localized spots is associated with more hydrophobic compounds than in the cytosol.

Another finding confirmed nile red association with different compounds in vesicles and cytosol. Recorded excitation/emission scans in the CLSM gave maximum intensity at approximately 525/585 nm and 555/625 nm for vesicular and cytosolic areas in the cells respectively. These results correspond with those previously presented in that the emission maximum from the cytosol spectrum is shifted towards higher wavelengths when compared to the vesicle spectrum.

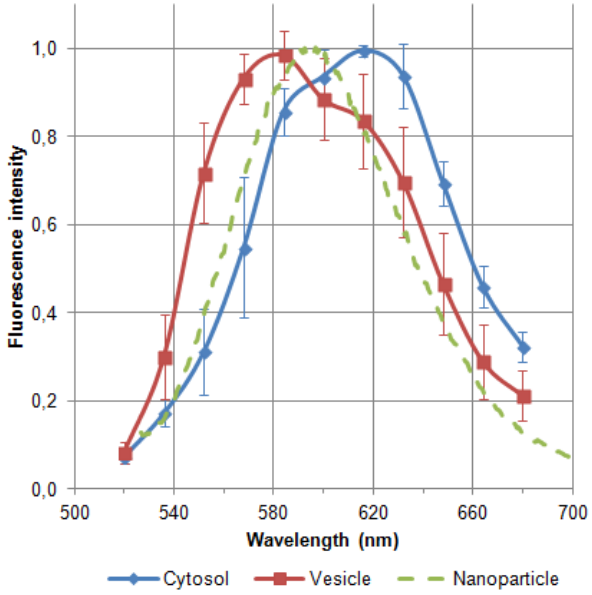

(a)

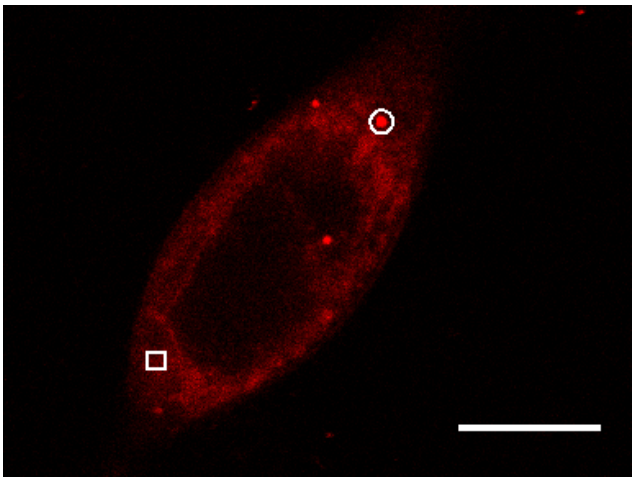

(b)

Figure 4.11: Different nile red emission spectra after excitation with a 488 nm laser are displayed in figure (a). The nanoparticle spectrum (dotted line) is measured in a spectrophotometer, whereas the spectra from cytosolic and vesicle associated nile red are obtained by recording λ-series in the CLSM. The plotted fluorescence intensity values are averages from 23 vesicular and 12 cytosolic regions from several cells with the corresponding standard deviations plotted as error bars. An illustration of a vesicular (circle) and cytosolic region (square) is given in (b), where a representative CLSM image is shown after approximately 1 hour incubation with nanoparticle B-JF1000-Hex. Nile red fluorescence is depicted in red, and the scale bar is 10 µm.

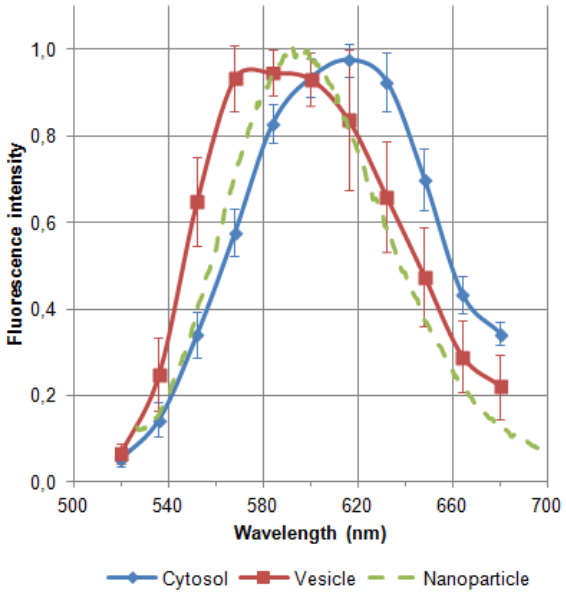

(a)

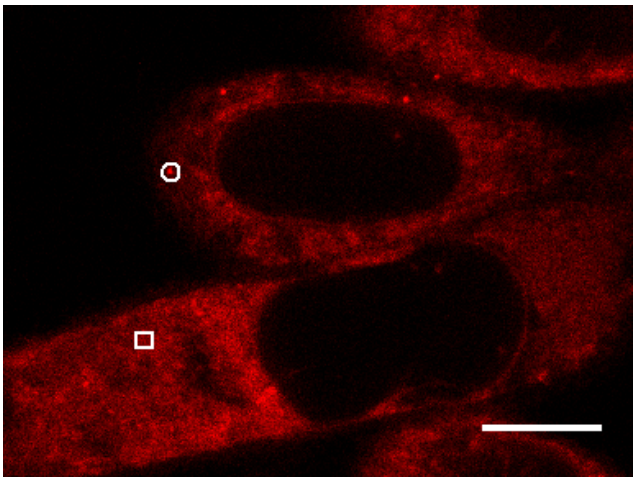

(b)

Figure 4.12: Different nile red emission spectra after excitation with a 488 nm laser are displayed in figure (a). The nanoparticle spectrum (dotted line) is measured in a spectrophotometer, whereas the spectra from cytosolic and vesicle associated nile red are obtained by recording λ-series in the CLSM. The plotted fluorescence intensity values are averages from 14 vesicular and 14 cytosolic regions from several cells with the corresponding standard deviations plotted as error bars. An illustration of a vesicular (circle) and cytosolic region (square) is given in (b), where a representative CLSM image is shown after approximately 1 hour incubation with nanoparticle B-JF1000. Nile red fluorescence is depicted in red, and the scale bar is 10 µm.

4.6 Spectrophotometric measurements of nile red

Spectrophotometric measurements on samples from the 7 particle batches chosen for further studies gave an estimate of the total nile red content in the particles, and the amount of nile red released to cell medium from nanoparticles after 3 hours. The values are presented in table 4.3, and the standard curves used for determining the amount of nile red in the samples are given in appendix D.

Table 4.3: An overview of the theoretical and measured nile red content in 20 µg/ml nanoparticles, as well as the amount of nile red released from this concentration of nanoparticles into cell medium after 3 hours. The relative release in percent (ratio of released amount to the total content in the particles) is also presented.

Batch	**Theoretical content** (ng/ml)	**Measured content** (ng/ml)	**Released to cell medium** (ng/ml)	**Relative release** (%)
B-JF1000-Hex	4	6.2	2.8	44.3
B-JF1000	20	25.1	13.7	54.5
B-JF2000	20	25.1	11.7	46.4
O-JF1000	20	20.3	14.2	69.6
B-AM750	20	33.2	14.6	44.0
B-AM2000	20	36.0	17.2	47.7
B-AM5000	20	20.4	9.5	46.5

4.6.1 Total nile red content in the nanoparticles

The measured total nile red content in the particles varies between batches, but all values are comparable or higher than the theoretical values. This shows that even if equal amounts of nile red were added during synthesis, the actual amount encapsulated can still differ. Measurements were done both 4 and 24 hours after the particles were added to THF (data only shown for 24 hours), with no or only a slight increase in detected amount of nile red, suggesting the particles were completely dissolved in THF after 24 hours. Altogether, it is plausible to believe that the resulting values give a reasonable measure on the total content in the particles, and at least it seems like the estimate is not too low.

4.6.2 Nile red release from the nanoparticles

A rather high amount of nile red was released from the nanoparticles to cell medium after 3 hours. The amount of released nile red varied from batch to batch, but when related to the actual amount present in the particles, the relative release (the ratio of released amount to the total content in the particles) is fairly equal between the majority of the batches. Altogether, the results suggest that the nanoparticles loose around 45% of their associated nile red marker after 3 hours in cell medium, except B-JF1000 and O-JF1000 which loose even more, approximately 55% and 70% respectively.

4.7 Toxicity of poly(alkyl cyanoacrylate) nanoparticles

The cytotoxic effect of the 7 nanoparticle batches chosen for further testing was investigated by the alamarBlue® cell viability assay. Table 4.4 gives a comparison of the EC_{50} and LD_{50} values estimated after 3 hours of nanoparticle exposure. The cell viability data after toxicity studies of the POCA particle (O-JF1000) do not form a bottom plateau (which would define y_{min}), and fitting of a dose response curve was not possible. Hence, the EC_{50} value from this particle is omitted in the table.

Table 4.4: A summary of the obtained EC_{50} and LD_{50} values after testing the toxicity of different nanoparticle batches in PC3 cells.

PEG	**Batch**	**EC_{50}** (µg/ml)	**LD_{50}** (µg/ml)
Jeffamine	B-JF1000-Hex	26.8	29.1
	B-JF1000	34.1	34.2
	B-JF2000	32.3	32.9
	O-JF1000		>240
Amino-PEG	B-AM750	27.2	29.2
	B-AM2000	30.5	32.0
	B-AM5000	53.7	57.2

4.7.1 Toxicity of Jeffamine PEGylated nanoparticles

The POCA based nanoparticle O-JF1000 is significantly less cytotoxic than its PBCA counterparts (B-JF1000-Hex, B-JF1000, B-JF2000). Within 3 hours of nanoparticle exposure, the cell viability after incubation with O-JF1000 does not

decrease lower than approximately 70% in the range of concentrations tested, whereas around 10% of cell survival is seen with the 3 other particles in the same interval. This is shown in figure 4.13 where the dose response curves after alamarBlue® measurements of Jeffamine PEGylated nanoparticles are presented. The reduced cytotoxicity of O-JF1000 is ascertained to stem from the change in monomer composition, since all other physicochemical characteristics are comparable to particle B-JF1000. (See table 3.1 for a comparison.)

After 3 hours exposure, PC3 cells can tolerate at least 8 times higher concentration of POCA nanoparticles than PBCA particles. This is evident since the LD_{50} value of O-JF1000 is assumed to be larger than 240 µg/ml, whereas the corresponding PBCA particles have LD_{50} values ∼30 µg/ml. The fitted curves from testing with particle B-JF1000-Hex, B-JF1000 and B-JF2000 have R^2 values larger than 0.9812 and p-values for all coefficients smaller than 0.0095, indicating that the curves, and hence also the LD_{50} values, are a good approximation to the data.

The Jeffamine PEGylated PBCA particles showed comparable cytotoxicity in PC3 cells; all had a steep decrease in cell viability around 20 µg/ml and only small variations in the LD_{50} and EC_{50} values between them. An increase in PEG chain length from molecular weight of 1000 to 2000 Da, between batch B-JF1000 and B-JF2000, does not seem to influence the toxicity. When comparing B-JF1000-Hex and B-JF1000, it is not possible to determine whether the kind of co-stabilizer used (hexadecane vs. miglyol) and cross-linking of the PBCA polymer in the particle affect the cytotoxicity. A large variation between experiments was experienced when B-JF1000-Hex was tested. Because of this, even though B-JF1000-Hex come up as slightly more toxic from the EC_{50} and LD_{50} values, the difference is small compared to the standard deviations in this concentration interval, and no conclusion regarding the effect of co-stabilizer and polymer cross-linking on particle cytotoxicity can be given.

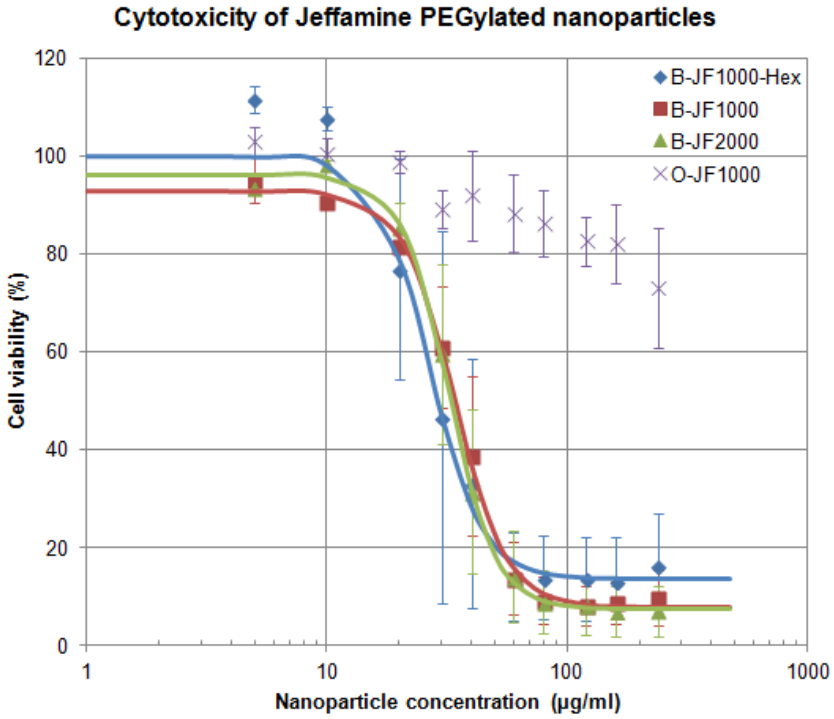

Figure 4.13: Cytotoxicity of Jeffamine PEGylated nanoparticles after 3 hours exposure, measured by the alamarBlue® assay. The obtained data are averages of 2 independent experiments, with the corresponding standard deviations plotted as error bars. The y-axis represents cell viability expressed as a % of control samples without added nanoparticles, and the x-axis displays increasing nanoparticle concentrations on a logarithmic scale. The solid drawn lines are fitted dose response curves, while the markers represent the averaged data points from the alamarBlue® measurements. All fitted curves have R^2 values larger than 0.9812 and p-values for all coefficients smaller than 0.0095.

4.7.2 Toxicity of Amino-PEGylated nanoparticles

An Amino-PEG chain length of 5000 Da reduces the cytotoxicity in PC3 cells compared to particles with shorter PEG chains. As can be seen from the dose response curves in figure 4.14, after 3 hours exposure, the particle with the longest PEG chain, B-AM5000, is the least cytotoxic of the Amino-PEGylated nanoparticles. The reduced cytotoxicity of B-AM5000 is ascertained to stem from the increase in PEG chain length, since all other physicochemical characteristics are comparable to particles B-AM750 and B-AM2000. (See table 3.1)

The LD_{50} and EC_{50} values suggest that PC3 cells can tolerate approximately 1.8 times higher concentration of B-AM5000 than of particles with shorter PEG chains. All fitted curves have R^2 values larger than 0.9875 and p-values for all coefficients smaller than 0.0276, indicating that the curves, and hence also the LD_{50} and EC_{50} values, are a good approximation to the data.

The toxicity of B-AM750 and B-AM2000 in PC3 cells was comparable, with only a slight difference in LD_{50} and EC_{50} values, indicating that an increase in PEG chain length from molecular weight of 750 to 2000 Da does not influence the cytotoxicity. This corresponds with results for Jeffamine PEGylated particles presented in the previous section, where no difference in toxicity between particles with chain lengths increasing from 1000 to 2000 Da was observed. Since B-AM5000 with a PEG chain length of 5000 Da was less cytotoxic, the results altogether suggest that a higher molecular weight than 2000 Da is needed to see a decrease in cytotoxicity after 3 hours exposure to PBCA nanoparticles.

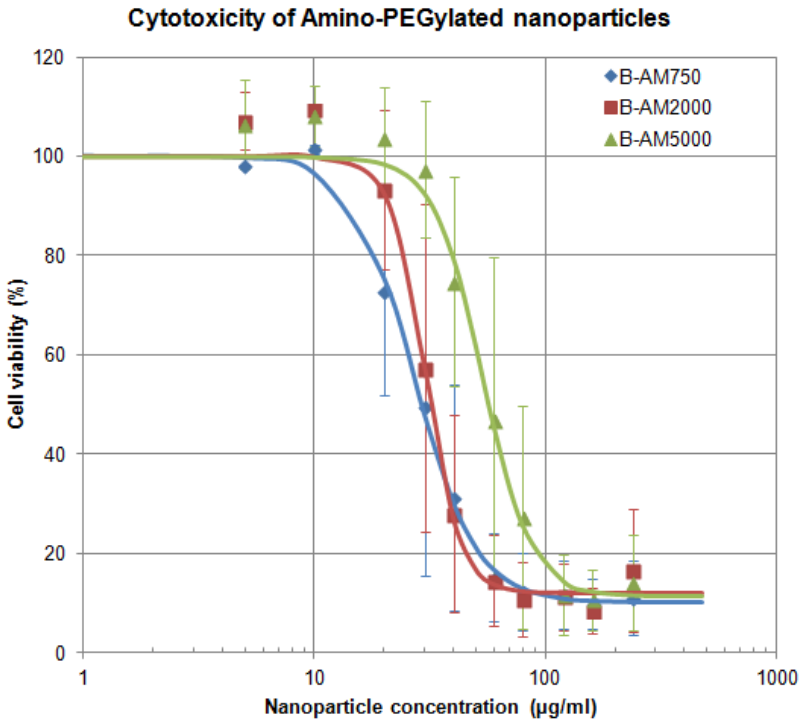

Figure 4.14: Cytotoxicity of Amino-PEGylated nanoparticles after 3 hours exposure, measured by the alamarBlue® assay. The obtained data are averages of 2 independent experiments, with the corresponding standard deviations plotted as error bars. The y-axis represents cell viability expressed as a % of control samples without added nanoparticles, and the x-axis displays increasing nanoparticle concentrations on a logarithmic scale. The solid drawn lines are fitted dose response curves, while the markers represent the averaged data points from the alamarBlue® measurements. All fitted curves have R^2 values larger than 0.9875 and p-values for all coefficients smaller than 0.0276.

5 Discussion

The goal of the current project has been to investigate what effect different PEGylation and monomer composition of poly(alkyl cyanoacrylate) nanoparticles had on cellular uptake, hydrophobic probe release and cell viability. In this section I will discuss my main findings, before finally making some general considerations about the significance of the results for further work with the nanoparticles.

5.1 PEG densities on the nanoparticles

All particles used have their PEG chains in a mushroom formation, independent of PEG type, number of PEGs attached and the PEG chain molecular weight, implying low PEG surface densities on all batches. The PEG densities of particles coated with chains of equal length were shown not to depend on the amount of PEG added during synthesis, indicating that addition of more PEG not will increase the density further, and that a change in either PEG type or the protocol for preparing the particles are necessary to achieve higher PEG density. Peracchia et al. have e.g. reported that the pH of the polymerization medium influences the amount of PEG attached to the surface of poly(isobutyl cyanoacrylate) nanoparticles. [128]

There is not an abundance of articles reporting on PEG chains per area on the surface of polymeric nanoparticles to compare the estimated values with. Some studies estimate PEG density from the amount of PEG added during synthesis (e.g. in references [129, 130, 131]), which is clearly not a valid assumption for particles prepared by the miniemulsion process used in this project. There are still a few examples where quantitative analysis of PEG chain density on polymeric particles has been performed. Wu et al. estimated a density of $\sim$1.5 chains per nm^2 on PBCA nanoparticles prepared by the miniemulsion method with a TWEEN 80 PEG [132], which is approximately 5 times higher than what was achieved with the Jeffamine 1000 PEGylated PBCA particles. This indicates that the choice of a linear or branched PEG can influence the PEG surface density. Peracchia and colleagues calculated a density of 0.7 chains/nm^2 on the surface of poly(isobutyl cyanoacrylate) nanoparticles, with a relatively long PEG (5000 Da) [133], corresponding to a density at least a factor 100 larger than what was estimated for the B-AM5000 batch. Other authors have also reported on significantly higher PEG densities than what have been estimated here. The area occupied by one PEG chain on the surface have been found to be: 15 nm^2 for a PEG 5000 chain attached to polylactide nanoparticles [134], 35 nm^2 for a PEG 7500 chain on polystyrene nanospheres [135] and 9.3 nm^2 on relatively bigger latex spheres (6 μm) [136]. Higher PEG densities have also been demonstrated on different carriers, such as

gold nanoparticles [137], altogether suggesting a relatively low PEG density on the particles used in this project compared to what is possible.

An effective shielding of the particle surface with a PEG coat is of importance to obtain sufficient circulation times *in vivo*. [15, 16, 45] Further studies to investigate whether the PEG layer present on the particles reduce plasma protein adsorption, and thereby complement activation and uptake by the MPS, need to be performed. Before that, the theoretical model published by Jeon and co-workers [138, 139] can give some indications to whether a higher surface coverage is necessary or not. For PEG chains attached to a planar hydrophobic surface, the model predicts that optimal protein repulsion occurs with long PEG chains and high surface density. [138] It was also calculated that an average distance between neighboring PEG chains of ∼1-1.5 nm is ideal for resisting adsorption of proteins ranging from 2-8 nm in size. [139] The estimated values for the distance between PEG chains found in this work are at least 4 times higher than the values predicted from the model, suggesting that a higher PEG surface density is necessary to achieve optimal protein repulsion. The model has also been shown to be in agreement with experimental results. [130, 140]

Influence of PEG chain length

A clear reduction in PEG density with chain length was found. This can be explained by already attached PEG chains on the surface that induce a steric repulsion of the PEG remaining in the solution, resulting in less PEG chains able to come close enough to the particle surface to react with the monomer. The repulsive force will increase in strength with PEG chain length, thereby explaining the gradual decrease in PEG density seen between particles coated with Amino-PEG 750, 2000 and 5000. Corroborating with my results, Wu and colleagues also found that the PEG density on PBCA particles decreased when the length of the PEG chain increased. [132]

Even if an evident decrease in PEG density is observed with longer PEG chains, this does not directly imply that the surface coverage is poorer. A longer PEG chain has a larger Flory radius, meaning it occupies more area on the surface compared to a smaller PEG. In other words, fewer long PEG chains are needed to cover the same surface area of a particle. This can be exemplified by comparing the Amino-PEGylated particles: By relating the total area occupied by the PEG chains ($\pi R_F^2 \times N_{PEG}$) to the surface area of the particle, a relative surface coverage of ∼30% was obtained for all 3 particles, regardless of their difference in PEG density. Altogether, this shows that comparing PEG densities is useful when particles are PEGylated with chains of equal length, but if the chain lengths are different, also

the polymer size must be taken into account in order to say something about the surface coverage provided by the PEG chains.

A longer PEG chain will, even if present in the mushroom regime, extend further out from the surface than a shorter PEG chain, creating a "thicker" PEG layer, as illustrated in figure 5.1. The effect of a thicker PEG layer should not be disregarded, as it is believed to be a determining factor in how effective the PEG coat is at reducing protein adsorption. [45, 138] (See section 2.1.4) If you compare particles with their PEG chains present in the same conformation, this means that a particle surface can be equally well or even better protected with a long PEG chain present in lower density as with a shorter chain present in higher density.

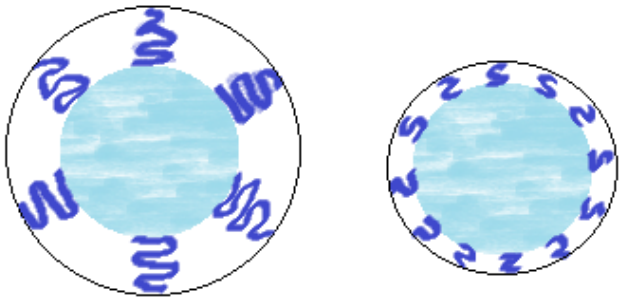

Figure 5.1: An illustration showing two nanoparticles PEGylated with a long (left) and short (right) PEG chain. The longest PEG chain extends further out from the surface than the short, increasing the relative "thickness" of the PEG layer, indicated with the black circle.

Correlation between PEG density and ζ-potential

The ζ-potential is often used as an indicator on the degree of PEG covering the surface of poly(alkyl cyanoacrylate) nanoparticles, by assuming that more nonionic PEG chains attached to the surface will shield the negatively charged surface groups better, resulting in a more positive ζ-potential. This seems like a reasonable assumption, and it has indeed been demonstrated that addition of more PEG during synthesis yield higher ζ-potentials. [133, 141, 142] From my results, this expected correlation was not observed, suggesting that one has to be cautious with using the ζ-potential to directly interpret PEG surface density.

One possible explanation to the discrepancy is inconsistencies in the ζ-potential measurements, as it has been observed in our lab that the measured values can vary according to the concentration of nanoparticles in the sample. Other experimental errors can also influence the result, since the estimated PEG densities do not have very large variations between them. Moreover, the shielding of the negative surface groups might not be as efficient as in theory, because of low coverage on the particle surface, with PEG chains in the mushroom conformation. A surface layer, containing residues from components used in the synthesis that are not removed by dialysis, have been observed after particle preparation. Nile red, unpolymerized monomer and possibly also PEG chains and surfactants, can associate with the hydrophobic particle surface if they are redundant in the solution. That some PEG is present in this surface layer, or elsewhere in the particle solution, is confirmed by the NMR analyses, since less PEG was detected after centrifugation of the particle samples. The presence of this surface layer might somehow contribute to the counterintuitive correlation between ζ-potential and PEG density, if it shields or otherwise interferes with the measured surface charge on the particles.

5.2 Cellular uptake of nanoparticles

No definite proof of nanoparticle internalization in PC3 cells has been found in this study. Evaluation of nile red loaded nanoparticle uptake was complicated by probe dissociation from the particles, which has also been reported previously in the literature. [113, 114] The results suggest that detected nile red fluorescence after nanoparticle incubation stems from free nile red staining intracellular compartments rather than particle associated nile red, based on observations regarding reduction in fluorescence intensity after washing, temperature dependence of uptake and spectral analysis of intracellular nile red. It is also supported by how previous studies with pharmacological inhibition of endocytosis did not decrease the amount of nile red positive cells. [17]

Effects of washing on nile red fluorescence intensity

After washing, the fluorescence intensity from all samples was considerably reduced, in most cases showing values comparable to the control samples. Previously performed experiments confirmed the effect of washing on nile red positive cells with CLSM imaging as well. [17] If cells had internalized nanoparticles, it is very unlikely that particles in vesicles could be washed out of the cells during spin down, especially when considering centrifugation of cell samples to be common practice. Rather, the most probable explanation is efflux of nile red from cells, when nile

red containing medium is replaced by nile red free medium during the washing procedure, caused by a concentration gradient across the cell membrane. In line with this, Xu. et al. were able to detect a decrease in intracellular nile red fluorescence during CLSM imaging, when nanoparticle-medium solution was replaced with particle free medium. [113] The reduction in nile red fluorescence with more extensive washing indicates that detected nile red is free and not encapsulated in particles.

Temperature dependence of cellular uptake

A slight temperature dependence on cellular uptake of nile was observed. All nanoparticle batches tested were able to deliver more nile red to cells at 37°C compared to 4°C. After washing, the MFI from cells incubated with nanoparticles and untreated cells were comparable at 37°C and 4°C, whereas a more prominent difference was observed in the percentage of positive cells for some of the particle batches. At first glance, this might indicate energy dependent uptake, but it can also be a consequence of more delivered free nile red at 37°C. When cells have taken up more nile red it follows that more extensive washing is required to efflux the same amount of nile red from the cells. In light of the other results, the latter explanation is more plausible.

Spectral analysis of intracellular nile red

Spectral analysis of intracellular nile red clearly showed that the fluorescent probe is associated with different compounds in cytosol and in what appeared as localized brighter spots. The emission maximum shifted towards higher wavelengths in cytosol compared to the spots, indicating nile red bound to less hydrophobic compounds in this area of the cells. [110, 111]

The fluorescence from vesicular regions was hypothesized to stem from nanoparticles in endocytic vesicles or free nile red staining lipid compounds. From the spectral analysis of intracellular nile red, the emission spectrum from the vesicular regions overlap with the nanoparticle emission spectrum, and therefore do not exclude the possibility for detected nile red fluorescence in localized spots to be nanoparticles in endocytic vesicles. Despite this, if the result from the spectral analysis is seen in connection with the cellular uptake studies and the high estimated nile red release from particles, it is more probable that the bright spots observed in CLSM images are caused by free nile red that has diffused into cytosol and subsequently stained lipid compartments. Free nile red will fluoresce intensely in the presence of phospholipid vesicles [111], like endo- and lysosomes. Master

student Sofie Snipstad demonstrated no co-localization of nile red with early endosomes [143], whereas Brown et al. have shown high nile red affinity for lysosomes and other lipid droplets. [144], altogether suggesting a higher probability for free nile red to stain lysosomes than early endosomes. Further studies (for instance to investigate co-localization with lysosomes) must be performed in order to shed more light on which intracellular compounds and membranes nile red has highest affinity for.

Does endocytosis of poly(alkyl cyanoacrylate) nanoparticles occur?

Even if endocytosed nanoparticles cannot be detected, it does not exclude the possibility that particles are being internalized. The nanoparticles have a high nile red release relative to the total content in the particles, and the transfer of nile red into cells is seemingly enhanced by a contact mediated mechanism [112, 113, 114, 143], suggesting an even higher release of nile red in the presence of cells. Surface bound nanoparticles, or particles dispersed in the surrounding cell medium, were rarely observed during CLSM imaging, in support of this theory. If the majority of nile red is dissociated from the nanoparticles after 3 hours, there is no way to determine where the particles are located and confirm the presence of possible internalized particles with FCM and CLSM.

Because of the reasons outlined above, it has not been possible to assess if cellular uptake of nanoparticles occurred or not. This concluded my project work as well [17], and the findings in this thesis show that the alterations in PEGylation done in this study did not reduce nile red release enough for detection of particles to be possible, probably caused by the low PEG surface density on all batches. Alternative labeling with fluorescein dyes was tried out, but unfortunately none of the labeling procedures were satisfactory. There were different problems with the batches, but mainly the challenge was to attach proper amounts of fluorescein dye to the particles. Recently, a protocol for synthesizing rhodamine tagged PBCA nanoparticles, inspired by the work of Brambilla et al. [145] is showing promise in our lab.

In light of what other authors have reported, there is reason to believe that poly(alkyl cyanoacrylate) nanoparticles are internalized in cells [141, 145, 146, 147, 148], it has just not been possible to detect it with the nile red loaded nanoparticles used in this study. Recent experiments with the rhodamine tagged PBCA nanoparticles mentioned above are corroborative, they indicate internalization as well. It is known that PEG density and conformation can influence cellular uptake [141, 146, 147], and this will be interesting to investigate further with these "new" nanoparticles.

5.3 Nile red release from the nanoparticles

It was found that the nile red marker could dissociate from the nanoparticles and into cell medium. Nile red leakage from different nanocarriers has also been reported previously in the literature by several authors. [113, 114, 149, 150, 151] The poly(alkyl cyanoacrylate) nanoparticles loose 45% or more of their encapsulated nile red after 3 hours in cell medium. This corresponds well with how Xu et al. found the relative nile red release from poly(D,L-lactide-co-glycolide) nanoparticles after 3 hours in PBS with added FBS to be between 50 and 75% [114], and also with the work of Delmas and colleagues, which showed approximately 40% nile red release from lipid nanoparticles after 5 hours. [151] Furthermore, the results clearly demonstrate the ineptness of nile red as a nanoparticle marker for use in flow cytometric and confocal microscopy analyses.

A denser PEG layer on the surface was hypothesized to reduce nile red release from the particles. From my results, neither an increase in PEG chain length nor density, decreased the release to any extent. An explanation to why the hypothesis did not hold can be that all particles in general had a low PEG surface density, with the chains in a mushroom configuration, which did not provide a dense enough hydrophilic layer to prevent nile red release, as illustrated in figure 5.2. High PEG density and long chains has been found to slow down hydrophobic drug release from poly(L-lactic acid) nanospheres [152], and PEG-poly(hexadecyl cyanoacrylate) niosomes with higher PEG density released a hydrophobic drug slower than those with lower density. [153] The drug release rate from poly(ethyl cyanoacrylate) nanoparticles in human plasma decreased with increasing PEG chain length [154], which also was true for the release rate from lipid nanocarriers. [155] Altogether, this suggests that it is possible to decrease probe release from nanoparticles, both by achieving a higher PEG density to force the chains into a brush conformation, and by attaching longer PEGs to the surface.

Mechanism of hydrophobic probe release from the nanoparticles

Nile red can be seen as a model drug, in order to propose a mechanism for the release of hydrophobic probes from poly(alkyl cyanoacrylate) nanoparticles. It is demonstrated that nile red ends up intracellularly after nanoparticle incubation, and it is thus a relevant system to look into for drug delivery purposes. In literature it is claimed that drug release from biodegradable nanoparticles occur through various processes: [107, 108, 109]

1. Desorption of drug bound to the surface
2. Diffusion through the nanoparticle matrix

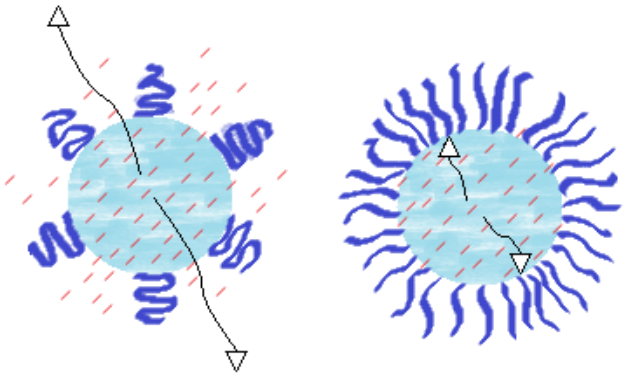

Figure 5.2: An illustration showing two nanoparticles with encapsulated nile red with their PEG chains in a mushroom (left) and brush (right) conformation. At low grafting density nile red is able to escape "through" the PEG layer, whereas at high PEG surface density nile red remains trapped in the core of the particle.

3. Nanoparticle matrix erosion
4. A combined erosion-diffusion process

The release profiles from poly(alkyl cyanoacrylate) nanoparticles found in the literature usually have two phases: An initial, rapid release and a second, slower, more controlled release. [141, 154, 156, 157, 158, 159] There is evidence of an initial burst release from the nanoparticles because of rapid nile red uptake in cells. [17, 143] This is believed to be due to nile red located in a residual surface layer or close to the surface of the particles. Initially, it was hypothesized that the particles were so hydrophobic that nile red would prefer to remain in the particle core, rather than diffusing out in the aqueous cell medium. Experimental evidence has shown that this is not the case, since nile red could be released to the surrounding solution in the presence of FBS, both demonstrated in this work and in studies of Xu et al. [114] and Klymchenko et al. [149], suggesting the existence of serum proteins with domains of equal or higher hydrophobicity as the nanoparticles. Moreover, Klymchenko and colleagues showed that nile red release from nanoemulsions is a very rapid process; dye leakage was detected already after 3 minutes [149], supporting the theory of an initial burst release.

Further, there is evidence for a sustained release, since after 3 hours, approximately 50% of the nile red marker is still remaining in the particles. The cellular uptake of nile red in cells after nanoparticle incubation has also been found to increase with time. [143] This second phase of drug release is usually attributed to probe

diffusion across the polymer matrix, polymer erosion or both. After dispersion in cell medium, the particle size has been shown to increase [160], suggesting a rapid protein adsorption on the surface and/or swelling caused by water seeping into the particles. A consequence of swelling is that the environment surrounding encapsulated nile red will be less hydrophobic, providing an explanation to why it is also favorable for nile red further away from the surface to dissociate from the particles. When the nile red surroundings become more hydrophilic, enhanced nile red diffusion to the particle surface can occur. At the surface, nile red can associate with hydrophobic parts of adsorbed proteins or other dispersed components, which can further mediate nile red transfer into the solution. Polymer erosion can also result in nile red being released from the nanoparticles, both because nile red present in the surface eroding layers are liberated, and since partially hydrolyzed polymers become more hydrophilic, and for the same reasons as outlined above, this reduction in hydrophobicity of the nile red surroundings can contribute to transfer nile red into the medium. The POCA particle did not transfer significantly less nile red into cells, or reduced the release to cell medium compared to the PBCA particles, altogether suggesting that the drug release during the first 3 hours is governed by diffusion of nile red through the polymer matrix rather than polymer erosion. Master student Andreas Bøe has established that neither the PBCA nor POCA particles degraded to a large extent in cell medium after 4 hours [160], supporting this theory.

Contribution from a contact-mediated mechanism?

As stated in the introduction of this thesis, there is evidence suggesting that nanoparticle collisions with the cell membrane contribute to the transfer of nile red into cells. A thorough study performed by master student Sofie Snipstad [143], confirms that a contact based mechanism plays a dominant role in the delivery of nile red to cells from PBCA nanoparticles. This can further increase our understanding of the release mechanism from the nanoparticles. It provides an additional explanation for the rapid uptake in cells, and also why more nile red is delivered at 37°C compared to 4°C. Moreover, and maybe even more important in the context of this thesis, is the fact that it can explain the difference between the particle batches in their ability to deliver nile red to cells. The particle coated with the longest PEG chain, and as previously outlined also with the thickest PEG layer, transferred a significantly lower amount of nile red into cells than the rest of the particles. This is not caused by reduced nile red release to cell medium, since the relative release was comparable to the other batches. If collisions between particles and the cell membrane enhance nile red transfer, the decreased nile red delivery can be caused by a higher steric repulsion effect leading to fewer collisions.

This is a promising discovery, since it indicates that the drug release profile of the nanoparticles can be modified by alterations in PEGylation.

5.4 Cytotoxicity of poly(alkyl cyanoacrylate) nanoparticles

In vitro experiments showed that toxicity in the PC3 cell line after exposure to poly(alkyl cyanoacrylate) nanoparticles was largely dependent on the length of the alkyl side chain in the polymer; the POCA particles were significantly less toxic than their PBCA counterparts. All nanoparticles exhibited a dose response toxicity, which is believed to be caused by release of degradation products, either intra- or extracellularly. Literature tends to conclude that the toxicity mainly stems from extracellular release of degradation products [66, 67], with particles adhering to the cell membrane contributing more than those dispersed in solution. [67] There is also reason to believe that remaining surfactant after synthesis induce toxicity, as the measured cytotoxicity in general was higher than what is reported in literature for similar nanoparticles. [67, 141, 142, 161, 165, 166]

Effect of monomer composition on cytotoxicity

Reduced toxicity of POCA nanoparticles compared to PBCA particles is corroborated by how several studies have found poly(alkyl cyanoacrylate) nanoparticles with shorter alkyl side chains to be more cytotoxic than those with longer side chains. [66, 67, 161, 162] This effect of monomer composition is attributed to a slower release of degradation products. The length of the alkyl side chain determines the rate of poly(cyanoacrylate) degradation [61], and hence the liberation of degradation products is expected to increase with decreasing side chain length. Nanoparticles dispersed in cell medium will degrade to an alcohol and a poly(cyanoacrylic acid), possibly accelerated by presence of esterases in FBS. [61, 62] These byproducts can cause cytotoxicity, both by formation of formaldehyde and/or by diffusion of the alcohol into cells. Master student Andreas Bøe has shown that POCA nanoparticles in cell medium degrade much slower than PBCA particles. [160] Therefore, the concentration of degradation products surrounding cells will be much lower after incubation with POCA particles, resulting in reduced toxicity compared to PBCA particles. An explanation to why byproducts from the degradation of this bioresorbable polymer cause toxicity is provided by Lherm et al. They found that degradation products had no effect on cell viability in an equal concentration to where nanoparticles exhibited a distinct cytotoxicity [67], and explained it by differences in cellular distribution of the degradation

products: byproducts in solution become evenly distributed in the cell medium, whereas nanoparticles can adhere to cell membranes and thereby cause high local concentrations of degradation products.

Cytotoxicity can be caused by degradation of internalized nanoparticles, and not only extracellular release of degradation products. Endocytosed particles will reside in the acidic environment of endosomes and/or lysosomes, which can affect the polymer degradation rate. At pH 4, the degradation of the nanoparticles utilized in this project was negligible during the same period of time used for the toxicity studies. [160] Despite this pH being more acidic than what is found in both early endosomes (pH∼6) and lysosomes (pH∼5) [163], it still establishes that lower pH slows down polymer degradation. On the other hand, several enzymes are released in the lysosomes, which possibly can catalyze the hydrolysis reaction of poly(alkyl cyanoacrylates). More experiments are needed in order to determine how the trade-off between these two effects influence the degradation rate of particles in lysosomes, but it is plausible to believe that the relative difference in degradation rate between polymers with different alkyl side chain length still holds. This means that cytotoxicity also can be caused by internalized nanoparticles, since the POCA nanoparticles would degrade slower and release less degradation products than the PBCA particles in endocytic vesicles as well.

Influence of surfactant on cytotoxicity

The surfactant used for emulsification of the particles during synthesis can influence cytotoxicity. [66, 126] Surfactants are capable of disrupting cell membranes and thereby induce toxicity and lysis of cells. [164] There is a rather large discrepancy between the concentrations where PBCA nanoparticles exhibited cytotoxicity in this study, and what I have reviewed in the literature; an effect it is plausible to attribute to residual surfactant from the synthesis. Kreuter et al. found the LD_{50} value for PBCA nanoparticles in hepatocytes to be 400 µg/ml [161], and a LD_{50} value of 100 µg/ml was obtained by Kusonwiriyawong et al. in dendritic cells [165], a significantly higher tolerance than what was observed with the PBCA particles used in this work. (LD_{50} values between 30 and 55 µg/ml) Zhang et al. concluded that PEGylated PBCA particles were cytocompatible with human hepatoma cells at concentrations below 200 µg/ml after 4 hours exposure [142], and concentrations up to 50 µg/ml PBCA particles have been shown not to reduce cell viability in 3 other human hepatocellular cancer cell lines. [166] At a concentration of 100 µg/ml no cell mortality was seen in both L929 fibroblasts after 3 hours exposure [67] and in a breast cancer cell line [141], contrasting the sharp decrease in cell viability seen between 20 and 30 µg/ml in this study. Although

different cell lines have been used in the above mentioned studies, and an effect of cell type on cytotoxicity cannot be disregarded, it is more plausible to attribute the large discrepancy between my results and what is reported in literature to the surfactant, SDS. In previous studies of PBCA nanoparticles prepared by the same synthesis procedure as in this work, cytotoxicity in PC3 cells was found to be dependent on the type of surfactant; particles prepared with SDS were more toxic than when TWEEN 80 was used as an emulsifier. [126] An influence of the surfactant on the cytotoxicity is not contrasted by the reduced toxicity caused by longer alkyl side chain in the polymer: The PBCA particles erode faster than the POCA particles, and consequently they have a higher rate of surfactant release.

Influence of PEG chain length on cytotoxicity

The nanoparticle coated with the longest PEG chain (5000 Da) exhibited the lowest toxicity amongst the PBCA particles, most probably caused by a stronger steric repulsion effect between the particles and the cell membrane, resulting in less particle adherence and thus lower local concentrations of degradation products at the cell membrane. Other factors might also contribute to a slower release of degradation products. Since the poly(alkyl cyanoacrylate) nanoparticles undergo surface degradation, a thick PEG layer might shield the particle surface better from the surrounding cell medium than a thinner PEG layer, reducing the rate of polymer degradation. Nucleophilic groups that initiate hydrolysis of the polymer or enzymes can have difficulties in coming close enough to the particle surface because of steric hindrance provided by the long PEG chains. The mobility of the degradation products can also be restricted by the long PEGs and thereby slowing down the release.

Endocytosis of nanoparticles can provide an alternative explanation to why particles with the thickest PEG layer were less cytotoxic compared to particles coated with shorter PEG chains. Increasing degree of PEGylation can decrease the cellular uptake of nanoparticles [146, 141, 167] by reducing the interaction between particles and cells due to the hydrophilic stealth coat. [168] If the cytotoxicity is caused by endocytosed nanoparticles, a smaller number of internalized particles would reduce toxicity.

Relevance of *in vitro* cytotoxicity studies

To summarize, it can be stated that somewhat higher cytotoxicity than expected was observed after exposure to the nanoparticles, probably due to an influence of residual surfactant from the synthesis. In evaluating the significance of these results for using the particles as carriers of contrast or therapeutic agent, it has to be stressed that *in vitro* studies cannot be directly related to *in vivo* toxicity. The ratio of nanoparticles to cells during *in vitro* experiments is significantly higher than after *in vivo* administration. Moreover, if nanoparticle degradation products are responsible for the cytotoxicity of poly(alkyl cyanoacrylate) nanoparticles, under dynamic *in vivo* conditions these products can be eliminated from the nanoparticle location to a greater extent than in static *in vitro* experiments, thereby reducing the time of exposure of degradation products to cells and possibly minimizing adverse effects.

5.5 General considerations for further work

In light of all presented results in this thesis, lastly, I will try to make some general considerations on what can be learned from this work in order to optimize the poly(alkyl cyanoacrylate) nanoparticles for use as a drug delivery system and which properties it is important to improve.

For the function of the proposed nanocarrier, my results suggest that the particles have a too low PEG density both to obtain sufficient circulation times and to minimize drug leakage during circulation. It should therefore be prioritized to improve the PEG density on the particles, as this feature is essential for the particles' functionality *in vivo*. Higher PEG densities have been reported on PBCA particles prepared by the miniemulsion process [132], implicating that it is indeed possible to achieve, either by changing the protocol for synthesis or the utilized PEG type. There are also positive implications for the function of the nanoparticles from this study. An important barrier for efficient drug delivery from endocytosed nanomedicines is that the drug must be able to escape from endocytic vesicles. The proposed mechanism of drug transfer from the nanoparticles and into cells does not rely on endocytosis, and may therefore provide a promising method for intracellular drug delivery. For this to be a good strategy, a high release of drug during systemic circulation should be prevented. It is hypothesized that a denser PEG coating with chains in a brush conformation, can increase the nanoparticles' stability. The clinical relevance of the system has been demonstrated by showing that more nile red is delivered to cells when it is encapsulated in the nanoparticles compared to when administered alone. [143]

Safety of the proposed delivery system should be a main concern. Poly(alkyl cyanoacrylate) nanoparticles should degrade slowly enough to prevent high local concentrations of degradation products occurring and release degradation products at a rate which they can be metabolized without causing acute toxic effects. [67] From the *in vitro* toxicity studies, the POCA particles seem like the best candidate in this aspect. On the other hand, almost no degradation of POCA particles was detected in blood serum, even after three weeks [160], which on further reflection suggests that this polymer has a too slow degradation rate to be clinically relevant. (You do not want nanocarriers left in the blood stream more than three weeks after administration.) Instead of choosing POCA as the composition of the nanocarrier, my recommendation is rather to work on finding an alternative surfactant to SDS, to see if this will reduce the toxic effects caused by the PBCA nanoparticles. As higher tolerance of PBCA particles are frequently reported in the literature [67, 141, 142, 161, 165, 166], there is reason to believe that this strategy can work. For multiple dosing, the use of a faster degrading polymer is also more suitable to avoid polymer overloading of the cells. *In vivo* studies are needed in order to get a more relevant picture of the toxicity. If the PBCA particles exhibit too high toxicity in animals, and no alternative surfactant can be found, it is possible to try an intermediate chain length, like isohexyl. Poly(isohexyl nanoparticles) have made it to phase III clinical trials (Clinical trial ID: NCT01655693), implying that the polymer is biocompatible.

Another lesson learned from this study is that the PEG chain length, and thereby the relative PEG layer thickness, is an important factor to consider. The results suggest that coating of the particle with a longer PEG chain can provide similar, or even better protected surfaces, than with a shorter PEG chain present in a higher density. This is of significance, because the fewer PEG chains that can be used to achieve the same effect the better, as the amount of non-biodegradable PEGs is minimized. It has been demonstrated in this work that an increase in PEG layer thickness reduce toxicity and modify the delivery of nile red to cells, further confirming the significance of the PEG layer for nanoparticle function.

6 Conclusion

This study has investigated the effect of particle PEGylation and monomer composition on cellular uptake, nile red release and cytotoxicity. The estimated values for PEG chain density revealed low PEG surface coverage on all utilized particles, hence making it difficult to make any general conclusions about the effect of the PEG layer, since all PEG chains were present in the mushroom conformation, independent on number of PEGs attached and the molecular weight of the PEG used. Nevertheless, it was established that the alterations in PEGylation done in this study were not sufficient to reduce the nile red release from the particles enough for detection of endocytosis to be possible, probably caused by the low PEG surface density on all particles. It was also demonstrated that 45% or more of the encapsulated nile red marker is released to cell medium after 3 hours. This result suggests that a higher PEG surface coverage is needed in order to minimize release of hydrophobic drugs from the particles during circulation. Further studies are needed to determine if it is also necessary to increase the PEG density for preventing activation of complement and uptake by the MPS. As the PEG density for chains of equal length was shown not to depend on the amount added during synthesis, the results clearly imply that a different strategy than addition of more PEG is needed to achieve a denser PEG layer. It is also recommended that longer PEG chains are used, since these chains give a relatively thicker PEG layer. This is especially important if it turns out difficult to achieve higher PEG densities, as my results indicate that longer PEG chains can provide similar shielding of a surface as a shorter chain, even when present in lower densities.

Through experiments conducted it is clear that monomer composition had a significant influence on the cytotoxicity after nanoparticle exposure. The POCA particles with the longest alkyl side chain were considerably less cytotoxic than the PBCA particles, implicating that the release of degradation products is responsible for the induced toxicity. A contribution from residual surfactant should also be taken into consideration, as the observed cytotoxicity in general was higher than what is reported for similar nanoparticles in the literature. It should therefore be worked with finding an alternative surfactant to SDS, which functions equally well in synthesis, but induce less toxicity in cells.

References

[1] K. H. Bae, H. J. Chung, and T. G. Park. Nanomaterials for cancer therapy and imaging. *Mol. Cells*, 31:295–302, 2011.

[2] B. Boyle and B. Levin. *World Cancer Report 2008*. International Agency for Research on Cancer, 2008.

[3] B. A. Chabner and D. L. Longo. *Cancer chemotherapy and biotherapy: principles and practice*. LWW, 2011.

[4] D. Peer, J. M. Karp, S. Hong, O. C. Farokhzad, R. Margalit, and R. Langer. Nanocarriers as an emerging platform for cancer therapy. *Nat. Nanotechnol.*, 2:751–760, 2007.

[5] S. Hak, H. M. Sanders, P. Agrawal, S. Langereis, H. Grull, H. M. Keizer, F. Arena, E. Terreno, G. J. Strijkers, and K. Nicolay. A high relaxivity Gd(III)DOTA-DSPE-based liposomal contrast agent for magnetic resonance imaging. *Eur. J. Pharm. Biopharm.*, 72:397–404, 2009.

[6] E. Miele, G. P. Spinelli, E. Miele, F. Tomao, and S. Tomao. Albumin-bound formulation of paclitaxel (Abraxane ABI-007) in the treatment of breast cancer. *Int. J. Nanomedicine*, 4:99–105, 2009.

[7] C. Grange, S. Geninatti-Crich, G. Esposito, D. Alberti, L. Tei, B. Bussolati, S. Aime, and G. Camussi. Combined delivery and magnetic resonance imaging of neural cell adhesion molecule-targeted doxorubicin-containing liposomes in experimentally induced Kaposi's sarcoma. *Cancer Res.*, 70:2180–2190, 2010.

[8] Y. Liu, H. Miyoshi, and M. Nakamura. Nanomedicine for drug delivery and imaging: a promising avenue for cancer therapy and diagnosis using targeted functional nanoparticles. *Int. J. Cancer*, 120:2527–2537, 2007.

[9] B. Sumer and J. Gao. Theranostic nanomedicine for cancer. *Nanomedicine*, 3:137–140, 2008.

[10] J. Xie, S. Lee, and X. Chen. Nanoparticle-based theranostic agents. *Adv. Drug Deliv. Rev.*, 62:1064–1079, 2010.

[11] M. J. Lind. Principles of cytotoxic chemotherapy. *Medicine*, 36:19–23, 2008.

[12] A. Verma and F. Stellacci. Effect of surface properties on nanoparticle-cell interactions. *Small*, 6:12–21, 2010.

[13] A. E. Nel, L. Madler, D. Velegol, T. Xia, E. M. Hoek, P. Somasundaran, F. Klaessig, V. Castranova, and M. Thompson. Understanding biophysicochemical interactions at the nano-bio interface. *Nat. Mater.*, 8:543–557, 2009.

[14] V. Mailänder and K. Landfester. Interaction of nanoparticles with cells. *Biomacromolecules*, 10:2379–2400, 2009.

[15] J. V. Jokerst, T. Lobovkina, R. N. Zare, and S. S. Gambhir. Nanoparticle PEGylation for imaging and therapy. *Nanomedicine*, 6:715–728, 2011.

[16] L. E. van Vlerken, T. K. Vyas, and M. M. Amiji. Poly(ethylene glycol)-modified nanocarriers for tumor-targeted and intracellular delivery. *Pharm. Res.*, 24:1405–1414, 2007.

[17] S. Westrøm. Investigation of cellular uptake of PBCA nanoparticles. Project work, Norwegian University of Science and Technology, 2012.

[18] V. Wagner, B. Hüsing, S. Gaisser, and A. K. Bock. Nanomedicine: Drivers for development and possible impacts. JRC Scientific and Technical Report 46744, European Commision's Joint Research Centre, 2006.

[19] V. Wagner, A. Dullaart, A. K. Bock, and A. Zweck. The emerging nanomedicine landscape. *Nat. Biotechnol.*, 24:1211–1217, 2006.

[20] K. Cho, X. Wang, S. Nie, Z. G. Chen, and D. M. Shin. Therapeutic nanoparticles for drug delivery in cancer. *Clin. Cancer Res.*, 14:1310–1316, 2008.

[21] S. Parveen, R. Misra, and S. K. Sahoo. Nanoparticles: a boon to drug delivery, therapeutics, diagnostics and imaging. *Nanomedicine*, 8:147–166, 2012.

[22] R. Duncan and R. Gaspar. Nanomedicine(s) under the microscope. *Mol. Pharm.*, 8:2101–2141, 2011.

[23] C. L. Ventola. The nanomedicine revolution: Part 2: Current and Future Clinical Applications. *P T*, 37:582–591, 2012.

[24] G. Orive, R. M. Hernandez, A. Rodriguez Gascon, A. Dominguez-Gil, and J. L. Pedraz. Drug delivery in biotechnology: present and future. *Curr. Opin. Biotechnol.*, 14:659–664, 2003.

[25] T. M. Allen and P. R. Cullis. Drug delivery systems: entering the mainstream. *Science*, 303:1818–1822, 2004.

[26] N. Kamaly, Z. Xiao, P. M. Valencia, A. F. Radovic-Moreno, and O. C. Farokhzad. Targeted polymeric therapeutic nanoparticles: design, development and clinical translation. *Chem. Soc. Rev.*, 41:2971–3010, 2012.

[27] G. Ledet and T. K. Mandal. Nanomedicine: Emerging therapeutics for the 21st century. *US pharm*, 37:7–11, 2012.

[28] D. W. Northfelt, B. J. Dezube, J. A. Thommes, B. J. Miller, M. A. Fischl, A. Friedman-Kien, L. D. Kaplan, C. Du Mond, R. D. Mamelok, and D. H. Henry. Pegylated-liposomal doxorubicin versus doxorubicin, bleomycin, and vincristine in the treatment of AIDS-related Kaposi's sarcoma: results of a randomized phase III clinical trial. *J. Clin. Oncol.*, 16:2445–2451, 1998.

[29] A. N. Gordon, J. T. Fleagle, D. Guthrie, D. E. Parkin, M. E. Gore, and A. J. Lacave. Recurrent epithelial ovarian carcinoma: a randomized phase III study of pegylated liposomal doxorubicin versus topotecan. *J. Clin. Oncol.*, 19:3312–3322, 2001.

[30] W. J. Gradishar, S. Tjulandin, N. Davidson, H. Shaw, N. Desai, P. Bhar, M. Hawkins, and J. O'Shaughnessy. Phase III trial of nanoparticle albumin-bound paclitaxel compared with polyethylated castor oil-based paclitaxel in women with breast cancer. *J. Clin. Oncol.*, 23:7794–7803, 2005.

[31] M. C. Pinder and N. K. Ibrahim. Nanoparticle albumin-bound paclitaxel for treatment of metastatic breast cancer. *Drugs Today*, 42:599–604, 2006.

[32] L. Smith, Z. Kuncic, K. Ostrikov, and S. Kumar. Nanoparticles in cancer imaging and therapy. *J. Nanomater.*, 2012.

[33] M. A. Hahn, A. K. Singh, P. Sharma, S. C. Brown, and B. M. Moudgil. Nanoparticles as contrast agents for in-vivo bioimaging: current status and future perspectives. *Anal. Bioanal. Chem.*, 399:3–27, 2011.

[34] J. F. Hainfeld, D. N. Slatkin, T. M. Focella, and H. M. Smilowitz. Gold nanoparticles: a new X-ray contrast agent. *Brit. J. Radiol.*, 79:248–253, 2006.

[35] C. Fang and M. Zhang. Multifunctional magnetic nanoparticles for medical imaging applications. *J. Mater. Chem.*, 19:6258–6266, 2009.

[36] S. Fokong, B. Theek, Z. Wu, P. Koczera, L. Appold, S. Jorge, U. Resch-Genger, M. van Zandvoort, G. Storm, F. Kiessling, and T. Lammers. Image-guided, targeted and triggered drug delivery to tumors using polymer-based microbubbles. *J. Control. Release*, 163:75–81, 2012.

[37] B. A. Kairdolf, A. M. Smith, T. D. Stokes, M. D. Wang, A. N. Young, and S. Nie. Semiconductor Quantum Dots for Bioimaging and Biodiagnostic Applications. *Annu. Rev. Anal. Chem.*, 2013.

[38] G. Ting, C. H. Chang, and H. E. Wang. Cancer nanotargeted radiopharmaceuticals for tumor imaging and therapy. *Anticancer Res.*, 29:4107–4118, 2009.

[39] F. Kiessling, S. Fokong, P. Koczera, W. Lederle, and T. Lammers. Ultrasound microbubbles for molecular diagnosis, therapy, and theranostics. *J. Nucl. Med.*, 53:345–348, 2012.

[40] N. Sanvicens and M. P. Marco. Multifunctional nanoparticles–properties and prospects for their use in human medicine. *Trends Biotechnol.*, 26:425–433, 2008.

[41] Z. Cheng, A. Al Zaki, J. Z. Hui, V. R. Muzykantov, and A. Tsourkas. Multifunctional nanoparticles: cost versus benefit of adding targeting and imaging capabilities. *Science*, 338:903–910, 2012.

[42] R. Gref, Y. Minamitake, M. T. Peracchia, V. Trubetskoy, V. Torchilin, and R. Langer. Biodegradable long-circulating polymeric nanospheres. *Science*, 263:1600–1603, 1994.

[43] S. M. Ryan, G. Mantovani, X. Wang, D. M. Haddleton, and D. J. Brayden. Advances in PEGylation of important biotech molecules: delivery aspects. *Expert Opin. Drug Deliv.*, 5:371–383, 2008.

[44] A. Gabizon, H. Shmeeda, and T. Grenader. Pharmacological basis of pegylated liposomal doxorubicin: impact on cancer therapy. *Eur. J. Pharm. Sci.*, 45:388–398, 2012.

[45] D. E. Owens and N. A. Peppas. Opsonization, biodistribution, and pharmacokinetics of polymeric nanoparticles. *Int. J. Pharm.*, 307:93–102, 2006.

[46] S. M. Moghimi and J. Szebeni. Stealth liposomes and long circulating nanoparticles: critical issues in pharmacokinetics, opsonization and protein-binding properties. *Prog. Lipid Res.*, 42:463–478, 2003.

[47] B. Romberg, W. E. Hennink, and G. Storm. Sheddable coatings for long-circulating nanoparticles. *Pharm. Res.*, 25:55–71, 2008.

[48] H. Hatakeyama, H. Akita, and H. Harashima. A multifunctional envelope type nano device (MEND) for gene delivery to tumours based on the EPR effect: a strategy for overcoming the PEG dilemma. *Adv. Drug Deliv. Rev.*, 63:152–160, 2011.

[49] S. Hak, E. Helgesen, H. H. Hektoen, E. M. Huuse, P. A. Jarzyna, W. J. Mulder, O. Haraldseth, and C. d. L. Davies. The effect of nanoparticle polyethylene glycol surface density on ligand-directed tumor targeting studied in vivo by dual modality imaging. *ACS Nano*, 6:5648–5658, 2012.

[50] A. Judge, K. McClintock, J. R. Phelps, and I. MacLachlan. Hypersensitivity and loss of disease site targeting caused by antibody responses to PEGylated liposomes. *Mol. Ther.*, 13:328–337, 2006.

[51] T. Ishida, X. Wang, T. Shimizu, K. Nawata, and H. Kiwada. PEGylated liposomes elicit an anti-PEG IgM response in a T cell-independent manner. *J. Control. Release*, 122:349–355, 2007.

[52] C. Pinto Reis, R. J. Neufeld, A. J. Ribeiro, and F. Veiga. Nanoencapsulation I. Methods for preparation of drug-loaded polymeric nanoparticles. *Nanomedicine*, 2:8–21, 2006.

[53] R. A. Jain. The manufacturing techniques of various drug loaded biodegradable poly(lactide-co-glycolide) (PLGA) devices. *Biomaterials*, 21:2475–2490, 2000.

[54] S. Parveen and S. K. Sahoo. Polymeric nanoparticles for cancer therapy. *J. Drug Target.*, 16:108–123, 2008.

[55] F. Chiellini, A. M. Piras, C. Errico, and E. Chiellini. Micro/nanostructured polymeric systems for biomedical and pharmaceutical applications. *Nanomedicine*, 3:367–393, 2008.

[56] N. Wang and X. S. Wu. Synthesis, characterization, biodegradation, and drug delivery application of biodegradable lactic/glycolic acid oligomers: Part II. Biodegradation and drug delivery application. *J. Biomater. Sci. Polym. Ed.*, 9:75–87, 1997.

[57] M. Vert, S. M. Li, G. Spenlehauer, and P. Guerin. Bioresorbability and biocompatibility of aliphatic polyesters. *J. Mater. Sci. Mater. Med.*, 3:432–446, 1992.

[58] J. Kattan, J. P. Droz, P. Couvreur, J. P. Marino, A. Boutan-Laroze, P. Rougier, P. Brault, H. Vranckx, J. M. Grognet, and X. Morge. Phase I clinical trial and pharmacokinetic evaluation of doxorubicin carried by polyisohexylcyanoacrylate nanoparticles. *Invest. New Drugs*, 10:191–199, 1992.

[59] V. Lenaerts, P. Couvreur, D. Christiaens-Leyh, E. Joiris, M. Roland, B. Rollman, and P. Speiser. Degradation of poly (isobutyl cyanoacrylate) nanoparticles. *Biomaterials*, 5:65–68, 1984.

[60] L. Vansnick, P. Couvreur, D. Christiaens-Leyh, and M. Roland. Molecular weights of free and drug-loaded nanoparticles. *Pharmaceutical Research*, 2:36–41, 1985.

[61] R. H. Müller, C. Lherm, J. Herbort, and P. Couvreur. In vitro model for the degradation of alkylcyanoacrylate nanoparticles. *Biomaterials*, 11:590–595, 1990.

[62] D. Scherer, J. R. Robinson, and J. Kreuter. Influence of enzymes on the stability of polybutylcyanoacrylate nanoparticles. *Int . J. Pharm.*, 101:165–168, 1994.

[63] C. Vauthier, C. Dubernet, E. Fattal, H. Pinto-Alphandary, and P. Couvreur. Poly(alkylcyanoacrylates) as biodegradable materials for biomedical applications. *Adv. Drug Deliv. Rev.*, 55:519–548, 2003.

[64] N. Lewinski, V. Colvin, and R. Drezek. Cytotoxicity of nanoparticles. *Small*, 4:26–49, 2008.

[65] E. Igarashi. Factors affecting toxicity and efficacy of polymeric nanomedicines. *Toxicol. Appl. Pharmacol.*, 229:121–134, 2008.

[66] E. M. Gipps, P. Groscurth, J. Kreuter, and P. P. Speiser. The effects of polyalkylcyanoacrylate nanoparticles on human normal and malignant mesenchymal cells in vitro. *Int . J. Pharm.*, 40:23–31, 1987.

[67] C. Lherm, R. H. Müller, F. Puisieux, and P. Couvreur. Alkylcyanoacrylate drug carriers: II. Cytotoxicity of cyanoacrylate nanoparticles with different alkyl chain length. *Int . J. Pharm.*, 84:13–22, 1992.

[68] M. A. Dobrovolskaia and S. E. McNeil. Immunological properties of engineered nanomaterials. *Nat. Nanotechnol.*, 2:469–478, 2007.

[69] J. O'Brien, I. Wilson, T. Orton, and F. Pognan. Investigation of the Alamar Blue (resazurin) fluorescent dye for the assessment of mammalian cell cytotoxicity. *Eur. J. Biochem.*, 267:5421–5426, 2000.

[70] M. V: Lancaster and R. D. Fields. Antibiotic and cytotoxic drug susceptibility assays using resazurin and poising agents. *Biotechnol. Adv.*, 15:193, 1997.

[71] C. Vauthier and K. Bouchemal. Methods for the preparation and manufacture of polymeric nanoparticles. *Pharm. Res.*, 26:1025–1058, 2009.

[72] K. Landfester, A. Musyanovych, and V. Mailänder. From polymeric particles to multifunctional nanocapsules for biomedical applications using the miniemulsion process. *J. Polym. Sci. A Polym. Chem.*, 48:493–515, 2009.

[73] K. Landfester and V. Mailänder. Nanocapsules with specific targeting and release properties using miniemulsion polymerization. *Expert Opin. Drug Deliv.*, 10:593–609, 2013.

[74] T. Lammers. Nanomedicine on the move: from monotherapeutic regimens to combination therapies. *Expert Rev. Clin. Pharmacol.*, 5:105–108, 2012.

[75] R. M. Crist, J. H. Grossman, A. K. Patri, S. T. Stern, M. A. Dobrovolskaia, P. P. Adiseshaiah, J. D. Clogston, and S. E. McNeil. Common pitfalls in nanotechnology: lessons learned from NCI's Nanotechnology Characterization Laboratory. *Integr. Biol.*, 5:66–73, 2013.

[76] V. P. Chauhan, T. Stylianopoulos, Y. Boucher, and R. K. Jain. Delivery of molecular and nanoscale medicine to tumors: transport barriers and strategies. *Annu. Rev. Chem. Biomol. Eng.*, 2:281–298, 2011.

[77] G. N. Naumov, L. A. Akslen, and J. Folkman. Role of angiogenesis in human tumor dormancy: animal models of the angiogenic switch. *Cell Cycle*, 5:1779–1787, 2006.

[78] R. K. Jain. Determinants of tumor blood flow: a review. *Cancer Res.*, 48:2641–2658, 1988.

[79] T. P. Padera, B. R. Stoll, J. B. Tooredman, D. Capen, E. di Tomaso, and R. K. Jain. Pathology: cancer cells compress intratumour vessels. *Nature*, 427:695, 2004.

[80] A. J. Leu, D. A. Berk, A. Lymboussaki, K. Alitalo, and R. K. Jain. Absence of functional lymphatics within a murine sarcoma: a molecular and functional evaluation. *Cancer Res.*, 60:4324–4327, 2000.

[81] H. Hashizume, P. Baluk, S. Morikawa, J. W. McLean, G. Thurston, S. Roberge, R. K. Jain, and D. M. McDonald. Openings between defective endothelial cells explain tumor vessel leakiness. *Am. J. Pathol.*, 156:1363–1380, 2000.

[82] V. P. Chauhan, R. M. Lanning, B. Diop-Frimpong, W. Mok, E. B. Brown, T. P. Padera, Y. Boucher, and R. K. Jain. Multiscale measurements distinguish cellular and interstitial hindrances to diffusion in vivo. *Biophys. J.*, 97:330–336, 2009.

[83] T. Lammers, W. E. Hennink, and G. Storm. Tumour-targeted nanomedicines: principles and practice. *Br. J. Cancer*, 99:392–397, 2008.

[84] H. Maeda, J. Wu, T. Sawa, Y. Matsumura, and K. Hori. Tumor vascular permeability and the EPR effect in macromolecular therapeutics: a review. *J. Control. Release*, 65:271–284, 2000.

[85] S. Kunjachan, J. Jayapaul, M. E. Mertens, G. Storm, F. Kiessling, and T. Lammers. Theranostic systems and strategies for monitoring nanomedicine mediated drug targeting. *Curr. Pharm. Biotechnol.*, 13:609–622, 2012.

[86] R. K. Jain and T. Stylianopoulos. Delivering nanomedicine to solid tumors. *Nat. Rev. Clin. Oncol.*, 7:653–664, 2010.

[87] Y. H. Bae and K. Park. Targeted drug delivery to tumors: myths, reality and possibility. *J. Control. Release*, 153:198–205, 2011.

[88] T. Lammers, F. Kiessling, W. E. Hennink, and G. Storm. Drug targeting to tumors: principles, pitfalls and (pre-) clinical progress. *J. Control. Release*, 161:175–187, 2012.

[89] V. P. Torchilin. Drug targeting. *Eur. J. Pharm. Sci.*, 11 Suppl 2:81–91, 2000.

[90] D. Neri and R. Bicknell. Tumour vascular targeting. *Nat. Rev. Cancer*, 5:436–446, 2005.

[91] V. Frenkel. Ultrasound mediated delivery of drugs and genes to solid tumors. *Adv. Drug Deliv. Rev.*, 60:1193–1208, 2008.

[92] J. P. May and S. D. Li. Hyperthermia-induced drug targeting. *Expert Opin. Drug Deliv.*, 10:511–527, 2013.

[93] G. R. Anyarambhatla and D. Needham. Enhancement of the phase transition permeability of DPPC liposomes by incorporation of MPPC: A new temperature-sensitive liposome for use with mild hyperthermia. *Journal of Liposome Research*, 9:491–506, 1999.

[94] W. G. Pitt, G. A. Husseini, and B. J. Staples. Ultrasonic drug delivery - a general review. *Expert Opin. Drug Deliv.*, 1:37–56, 2004.

[95] A. Delalande, S. Kotopoulis, T. Rovers, C. Pichon, and M. Postema. Sonoporation at a low mechanical index. *Bubble Science, Engineering & Technology*, 3:3–12, 2011.

[96] A. Aderem and D. M. Underhill. Mechanisms of phagocytosis in macrophages. *Annu. Rev. Immunol.*, 17:593–623, 1999.

[97] S. D. Conner and S. L. Schmid. Regulated portals of entry into the cell. *Nature*, 422:37–44, 2003.

[98] P. Watson, A. T. Jones, and D. J. Stephens. Intracellular trafficking pathways and drug delivery: fluorescence imaging of living and fixed cells. *Adv. Drug Deliv. Rev.*, 57:43–61, 2005.

[99] J. Gruenberg. The endocytic pathway: a mosaic of domains. *Nat. Rev. Mol. Cell Biol.*, 2:721–730, 2001.

[100] T. Iversen, T. Skotland, and K. Sandvig. Endocytosis and intracellular transport of nanoparticles: Present knowledge and need for future studies. *Nano Today*, 6:176–185, 2011.

[101] G. J. Doherty and H. T. McMahon. Mechanisms of endocytosis. *Annu. Rev. Biochem.*, 78:857–902, 2009.

[102] H. Hillaireau and P. Couvreur. Nanocarriers' entry into the cell: relevance to drug delivery. *Cell. Mol. Life Sci.*, 66:2873–2896, 2009.

[103] G. Sahay, D. Y. Alakhova, and A. V. Kabanov. Endocytosis of nanomedicines. *J. Control. Release*, 145:182–195, 2010.

[104] I. Canton and G. Battaglia. Endocytosis at the nanoscale. *Chem. Soc. Rev.*, 41:2718–2739, 2012.

[105] T. L. Doane and C. Burda. The unique role of nanoparticles in nanomedicine: imaging, drug delivery and therapy. *Chem. Soc. Rev.*, 41:2885–2911, 2012.

[106] H. Lodish, A. Berk, SL. Zipursky, P. Matsudaira, D. Baltimore, and J. Darnell. *Molecular Cell Biology.* W. H. Freeman, 2000.

[107] K. Ringe, C. M. Walz, and B. A. Sabel. Nanoparticle drug delivery to the brain. *Encyclopedia of nanoscience and nanotechnology*, 7:91–104, 2004.

[108] A. Kumari, S. K. Yadav, and S. C. Yadav. Biodegradable polymeric nanoparticles based drug delivery systems. *Colloids Surf. B Biointerfaces*, 75:1–18, 2010.

[109] K. S. Soppimath, T. M. Aminabhavi, A. R. Kulkarni, and W. E. Rudzinski. Biodegradable polymeric nanoparticles as drug delivery devices. *J. Control. Release*, 70:1–20, 2001.

[110] P. Greenspan, E. P. Mayer, and S. D. Fowler. Nile red: a selective fluorescent stain for intracellular lipid droplets. *J. Cell Biol.*, 100:965–973, 1985.

[111] P. Greenspan and S. D. Fowler. Spectrofluorometric studies of the lipid probe, nile red. *J. Lipid Res.*, 26:781–789, 1985.

[112] L. C. Haynes and M. J. Cho. Mechanism of Nile red transfer from o/w emulsions as carriers for passive drug targeting to peritoneal macrophages in vitro. *Int . J. Pharm.*, 45:169 – 177, 1988.

[113] P. Xu, E. Gullotti, L. Tong, C. Highley, D. Errabelli, T. Hasan, J. Cheng, D. Kohane, and Y. Teo. Intracellular drug delivery of poly(lactic-co-glycolicacid) nanoparticles revisited. *Mol. Pharm.*, 6:190–201, 2009.

[114] P. Pietzonka, B. Rothen-Rutishauser, P. Langguth, H. Wunderli-Allenspach, E. Walter, and H. P. Merkle. Transfer of lipophilic markers from PLGA and polystyrene nanoparticles to caco-2 monolayers mimics particle uptake. *Pharm. Res.*, 19:595–601, 2002.

[115] X. Sun, F. Li, Y. Wang, and W. Liang. Cellular uptake and elimination of lipophilic drug delivered by nanocarriers. *Pharmazie*, 65:737–742, 2010.

[116] H. Chen, S. Kim, L. Li, S. Wang, K. Park, and J. X. Cheng. Release of hydrophobic molecules from polymer micelles into cell membranes revealed by Forster resonance energy transfer imaging. *Proc. Natl. Acad. Sci. U.S.A.*, 105:6596–6601, 2008.

[117] M. Rahman. Introduction to Flow Cytometry, 2006.

[118] P.N. Prasad. *Introduction to Biophotonics*. John Wiley & Sons, 2003.

[119] M. Rieseberg, C. Kasper, K. F. Reardon, and T. Scheper. Flow cytometry in biotechnology. *Appl. Microbiol. Biotechnol.*, 56:350–360, 2001.

[120] S. Basu, H. M. Campbell, B. N. Dittel, and A. Ray. Purification of specific cell population by fluorescence activated cell sorting (FACS). *J. Vis. Exp.*, 2010.

[121] D.B. Murphy and M.W. Davidson. *Fundamentals of Light Microscopy and Electronic Imaging*. John Wiley & Sons, 2012.

[122] J. Pawley. *Handbook of Biological Confocal Microscopy*. Language of science. Springer, 2006.

[123] P. G. De Gennes. Polymers at an interface; a simplified view. *Adv. Colloid Interface Sci.*, 27:189–209, 1987.

[124] A. K. Kenworthy, K. Hristova, D. Needham, and T. J. McIntosh. Range and magnitude of the steric pressure between bilayers containing phospholipids with covalently attached poly(ethylene glycol). *Biophys. J.*, 68:1921–1936, 1995.

[125] P. L. Hansen, J. A. Cohen, R. Podgornik, and V. A. Parsegian. Osmotic properties of poly(ethylene glycols): quantitative features of brush and bulk scaling laws. *Biophys. J.*, 84:350–355, 2003.

[126] M. Afadzi. *Delivery of Encapsulated Drugs to Cancer Cells and Tissue: The Impact of Ultrasound*. PhD thesis, Norwegian University of Science and Technology, 2013.

[127] C. O. Sullivan and C. Birkinshaw. In vitro degradation of insulin-loaded poly (n-butylcyanoacrylate) nanoparticles. *Biomaterials*, 25:4375–4382, 2004.

[128] M. T. Peracchia, C. Vauthier, F. Puisieux, and P. Couvreur. Development of sterically stabilized poly(isobutyl 2-cyanoacrylate) nanoparticles by chemical coupling of poly(ethylene glycol). *J. Biomed. Mater. Res.*, 34:317–326, 1997.

[129] V. C. Mosqueira, P. Legrand, R. Gref, B. Heurtault, M. Appel, and G. Barratt. Interactions between a macrophage cell line (J774A1) and surface-modified poly (D,L-lactide) nanocapsules bearing poly(ethylene glycol). *J. Drug Target.*, 7:65–78, 1999.

[130] R. Gref, M. Luck, P. Quellec, M. Marchand, E. Dellacherie, S. Harnisch, T. Blunk, and R. H. Muller. 'Stealth' corona-core nanoparticles surface modified by polyethylene glycol (PEG): influences of the corona (PEG chain length and surface density) and of the core composition on phagocytic uptake and plasma protein adsorption. *Colloids Surf. B Biointerfaces*, 18:301–313, 2000.

[131] V. C. Mosqueira, P. Legrand, J. L. Morgat, M. Vert, E. Mysiakine, R. Gref, J. P. Devissaguet, and G. Barratt. Biodistribution of long-circulating PEG-grafted nanocapsules in mice: effects of PEG chain length and density. *Pharm. Res.*, 18:1411–1419, 2001.

[132] M. Wu, E. Dellacherie, A. Durand, and E. Marie. Poly(n-butyl cyanoacrylate) nanoparticles via miniemulsion polymerization. 2. PEG-based surfactants. *Colloids Surf. B Biointerfaces*, 69:147–151, 2009.

[133] M. T. Peracchia, C. Vauthier, C. Passirani, P. Couvreur, and D. Labarre. Complement consumption by poly(ethylene glycol) in different conformations chemically coupled to poly(isobutyl 2-cyanoacrylate) nanoparticles. *Life Sci.*, 61:749–761, 1997.

[134] T. Riley, C. R. Heald, S. Stolnik, M. C. Garnett, L. Illum, S. S. Davis, S. M. King, R. K. Heenan, S. C. Purkiss, R. J. Barlow, et al. Core-shell structure of PLA-PEG nanoparticles used for drug delivery. *Langmuir*, 19:8428–8435, 2003.

[135] T. Matsuya, S. Tashiro, N. Hoshino, N. Shibata, Y. Nagasaki, and K. Kataoka. A core-shell-type fluorescent nanosphere possessing reactive poly(ethylene glycol) tethered chains on the surface for zeptomole detection of protein in time-resolved fluorometric immunoassay. *Anal. Chem.*, 75:6124–6132, 2003.

[136] S. J. Budijono, B. Russ, W. Saad, D. H. Adamson, and R. K. Prudhomme. Block copolymer surface coverage on nanoparticles. *Colloids Surf. A Physicochemical and Engineering Aspects*, 360:105–110, 2010.

[137] C. D. Walkey, J. B. Olsen, H. Guo, A. Emili, and W. C. Chan. Nanoparticle size and surface chemistry determine serum protein adsorption and macrophage uptake. *J. Am. Chem. Soc.*, 134:2139–2147, 2012.

[138] S. I. Jeon, J. H. Lee, J. D. Andrade, and P. G. De Gennes. Protein-surface interactions in the presence of polyethylene oxide: I. Simplified theory. *J. Colloid Interf. Sci.*, 142:149–158, 1991.

[139] S. I. Jeon and J. D. Andrade. Protein-surface interactions in the presence of polyethylene oxide: Ii. Effect of protein size. *J. Colloid Interf. Sci.*, 142:159–166, 1991.

[140] M. Vittaz, D. Bazile, G. Spenlehauer, T. Verrecchia, M. Veillard, F. Puisieux, and D. Labarre. Effect of PEO surface density on long-circulating PLA-PEO nanoparticles which are very low complement activators. *Biomaterials*, 17:1575–1581, 1996.

[141] K. R. Chaudhari, M. Ukawala, A. S. Manjappa, A. Kumar, P. K. Mundada, A. K. Mishra, R. Mathur, J. Monkkonen, and R. S. Murthy. Opsonization, biodistribution, cellular uptake and apoptosis study of PEGylated PBCA nanoparticle as potential drug delivery carrier. *Pharm. Res.*, 29:53–68, 2012.

[142] Y. Zhang, S. Zhu, L. Yin, F. Qian, C. Tang, and C. Yin. Preparation, characterization and biocompatibility of poly(ethylene glycol)-poly(n-butyl cyanoacrylate) nanocapsules with oil core via miniemulsion polymerization. *Eur. Polym. J.*, 44:1654–1661, 2008.

[143] S. Snipstad. Delivery mechanisms of hydrophobic drugs to cells from polymeric nanoparticles. Master's thesis, Norwegian University of Science and Technology, 2013.

[144] W. J. Brown, T. R. Sullivan, and P. Greenspan. Nile red staining of lysosomal phospholipid inclusions. *Histochemistry*, 97:349–354, 1992.

[145] D. Brambilla, J. Nicolas, B. Le Droumaguet, K. Andrieux, V. Marsaud, P. O. Couraud, and P. Couvreur. Design of fluorescently tagged poly(alkyl cyanoacrylate) nanoparticles for human brain endothelial cell imaging. *Chem. Commun.*, 46:2602–2604, 2010.

[146] C. K. Weiss, M. R. Lorenz, K. Landfester, and V. Mailänder. Cellular uptake behavior of unfunctionalized and functionalized PBCA particles prepared in a miniemulsion. *Macromol. Biosci.*, 7:883–896, 2007.

[147] H. R. Kim, K. Andrieux, S. Gil, M. Taverna, H. Chacun, D. Desmaele, F. Taran, D. Georgin, and P. Couvreur. Translocation of poly(ethylene glycol-co-hexadecyl)cyanoacrylate nanoparticles into rat brain endothelial cells: role of apolipoproteins in receptor-mediated endocytosis. *Biomacromolecules*, 8:793–799, 2007.

[148] K. R. Chaudhari, A. Kumar, V. K. M. Khandelwal, A. K. Mishra, J. Monkkonen, and R. S. R. Murthy. Targeting efficiency and biodistribution of zoledronate conjugated docetaxel loaded pegylated pbca nanoparticles for bone metastasis. *Adv. Func. Mat.*, 22:4101–4114, 2012.

[149] A. S. Klymchenko, E. Roger, N. Anton, H. Anton, I. Shulov, J. Vermot, Y. Mely, and T. F. Vandamme. Highly lipophilic fluorescent dyes in nano-emulsions: towards bright non-leaking nano-droplets. *RSC Advances*, 2:11876–11886, 2012.

[150] J. C. Leroux, P. Gravel, L. Balant, B. Volet, B. M. Anner, E. Allemann, E. Doelker, and R. Gurny. Internalization of poly(D,L-lactic acid) nanoparticles by isolated human leukocytes and analysis of plasma proteins adsorbed onto the particles. *J. Biomed. Mater. Res.*, 28:471–481, 1994.

[151] T. Delmas, A. Fraichard, P. Bayle, I. Texier, M. Bardet, J. Baudry, J. Bibette, and A. Couffin. Encapsulation and release behavior from lipid nanoparticles: Model study with nile red fluorophore. *J. Colloid Sci. Biotechnol.*, 1:16–25, 2012.

[152] M. T. Peracchia, R. Gref, Y. Minamitake, A. Domb, N. Lotan, and R. Langer. PEG-coated nanospheres from amphiphilic diblock and multiblock copolymers: investigation of their drug encapsulation and release characteristics. *J. Control. Release*, 46:223–231, 1997.

[153] B. Shi, C. Fang, and Y. Pei. Stealth PEG-PHDCA niosomes: effects of chain length of PEG and particle size on niosomes surface properties, in vitro drug

release, phagocytic uptake, in vivo pharmacokinetics and antitumor activity. *J. Pharm. Sci.*, 95:1873–1887, 2006.

[154] G. Fontana, M. Licciardi, S. Mansueto, D. Schillaci, and G. Giammona. Amoxicillin-loaded polyethylcyanoacrylate nanoparticles: influence of PEG coating on the particle size, drug release rate and phagocytic uptake. *Biomaterials*, 22:2857–2865, 2001.

[155] X. Zhang, Y. Gan, L. Gan, S. Nie, and W. Pan. PEGylated nanostructured lipid carriers loaded with 10-hydroxycamptothecin: an efficient carrier with enhanced anti-tumour effects against lung cancer. *J. Pharm. Pharmacol.*, 60:1077–1087, 2008.

[156] C. Y. Huang, C. M. Chen, and Y. D. Lee. Synthesis of high loading and encapsulation efficient paclitaxel-loaded poly(n-butyl cyanoacrylate) nanoparticles via miniemulsion. *Int. J. Pharm.*, 338:267–275, 2007.

[157] F. Ren, R. Chen, Y. Wang, Y. Sun, Y. Jiang, and G. Li. Paclitaxel-loaded poly(n-butylcyanoacrylate) nanoparticle delivery system to overcome multidrug resistance in ovarian cancer. *Pharm. Res.*, 28:897–906, 2011.

[158] L. Illum, M. A. Khan, E. Mak, and S. S. Davis. Evaluation of carrier capacity and release characteristics for poly (butyl 2-cyanoacrylate) nanoparticles. *Int. J. Pharm.*, 30:17–28, 1986.

[159] J. L. Arias, V. Gallardo, M. A. Ruiz, and A. V. Delgado. Ftorafur loading and controlled release from poly(ethyl-2-cyanoacrylate) and poly(butylcyanoacrylate) nanospheres. *Int. J. Pharm.*, 337:282–290, 2007.

[160] A. G. Bøe. Degradation of PBCA and POCA nanoparticles. Master's thesis, Norwegian University of Science and Technology, 2013.

[161] J. Kreuter, C. G. Wilson, J. R. Fry, P. Paterson, and J. H. Ratcliffe. Toxicity and association of polycyanoacrylate nanoparticles with hepatocytes. *J. Microencapsul.*, 1:253–257, 1984.

[162] C. Kubiak, P. Couvreur, L. Manil, and B. Clausse. Increased cytotoxicity of nanoparticle-carried Adriamycin in vitro and potentiation by verapamil and amiodarone. *Biomaterials*, 10:553–556, 1989.

[163] W. M. Becker, L. J. Kleinsmith, J. Hardin, and G. P. Bertoni. *The World of the Cell*. Pearson/Benjamin Cummings, Seventh edition, 2009.

[164] M. Aranzazu Partearroyo, H. Ostolaza, F. M. Goni, and E. Barbera-Guillem. Surfactant-induced cell toxicity and cell lysis. A study using B16 melanoma cells. *Biochem. Pharmacol.*, 40:1323–1328, 1990.

[165] C. Kusonwiriyawong, V. Lipipun, Q. Zhang, and G. C. Ritthidej. Poly (α-butyl cyanoacrylate) nanoparticles for intracellular delivery of protein: Physicochemical properties, cytotoxicity study and cellular uptake in dendritic cells. *J. Control. Release*, 132:e6–e8, 2008.

[166] J. Duan, Y. Zhang, S. Han, Y. Chen, B. Li, M. Liao, W. Chen, X. Deng, J. Zhao, and B. Huang. Synthesis and in vitro/in vivo anti-cancer evaluation of curcumin-loaded chitosan/poly(butyl cyanoacrylate) nanoparticles. *Int. J. Pharm.*, 400:211–220, 2010.

[167] S. Zhu, M. Hong, G. Tang, L. Qian, J. Lin, Y. Jiang, and Y. Pei. Partly PEGylated polyamidoamine dendrimer for tumor-selective targeting of doxorubicin: the effects of PEGylation degree and drug conjugation style. *Biomaterials*, 31:1360–1371, 2010.

[168] M. R. Hamblin, J. L. Miller, I. Rizvi, H. G. Loew, and T. Hasan. PEGylation of charged polymer-photosensitiser conjugates: effects on photodynamic efficacy. *Br. J. Cancer*, 89:937–943, 2003.

A PEG chemical structures

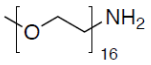

Amino-PEG 750
Molecular Weight: 735.90

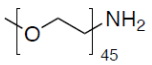

Amino-PEG 2000
Molecular Weight: 2013.42

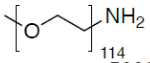

Amino-PEG 5000
Molecular Weight: 5053.05

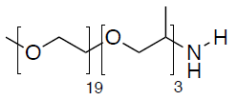

Jeffamine M-1000
Molecular Weight: 1042.29

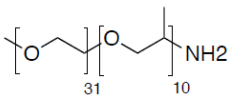

Jeffamine M-2070
Molecular Weight: 1977.48

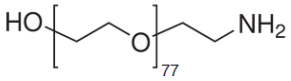

OH-PEG-NH2 3400
Molecular Weight: 3423.10

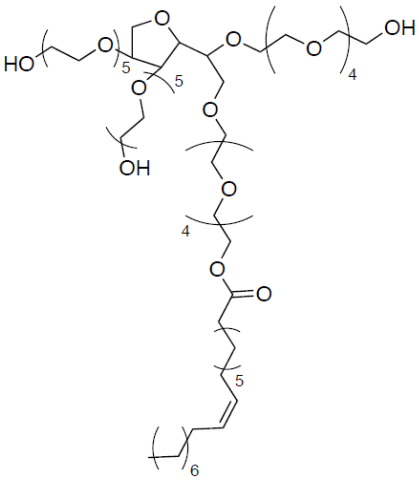

TWEEN 80

B Supporting figures for experiments with fluoresceinamine particle batch 66

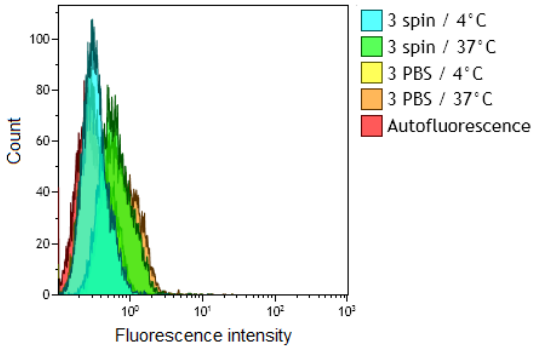

Figure B.1: Overlay histogram obtained in FCM analyses of PC3 cells incubated with fluoresceinamine labeled nanoparticle batch 66 for 3 hours at 37°C and 4°C. The fluorescence intensity is shown both after 3 times rinsing with PBS, and after additional 3 times centrifugation.

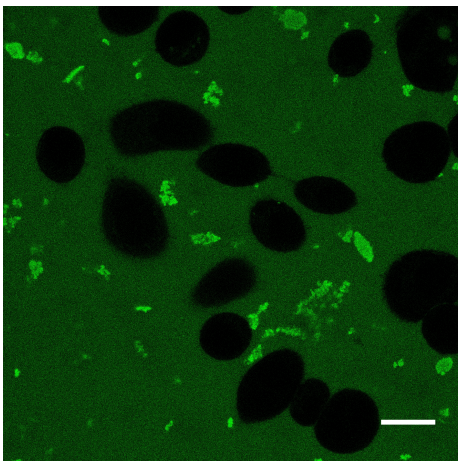

Figure B.2: CLSM image of PC3 cells after addition of the modified nanoparticle batch 66. Fluoresceinamine fluorescence is depicted in green, and the scale bar is 20 µm.

C Nile red fluorescence from different spectral intervals in FCM

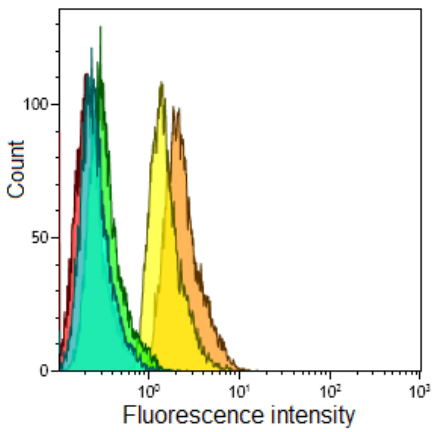

(a) Nile red fluorescence intensity detected in a 582 nm filter with 15 nm band pass.

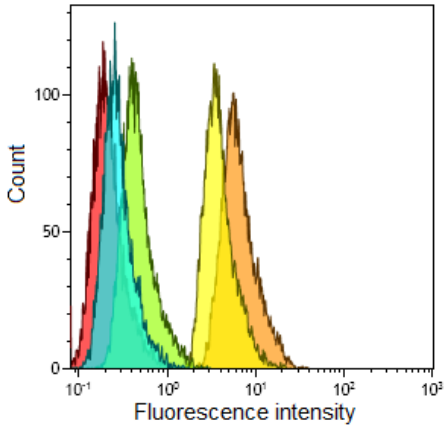

(b) Nile red fluorescence intensity detected in a 620 nm filter with 30 nm band pass.

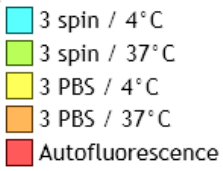

Figure C.1: Overlay histograms obtained in FCM analyses of PC3 cells incubated with nile red labeled nanoparticle batch 73 for 3 hours at 37°C and 4°C respectively. The fluorescence intensity is detected in two channels, both after 3 times rinsing with PBS, and after additional 3 times centrifugation. Both channels show similar fluorescence patterns, but higher intensity is detected in the 620 nm filter. What is shown here was representative for all the nile red labeled nanoparticles.

D Standard curves from spectrophotometric measurements

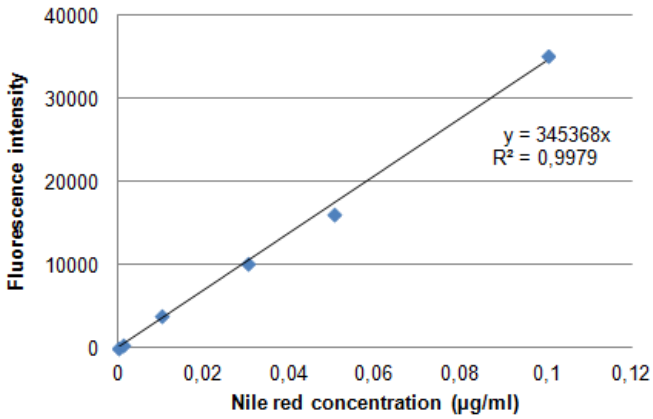

(a) Standard curve for nile red dissolved in hexadecane

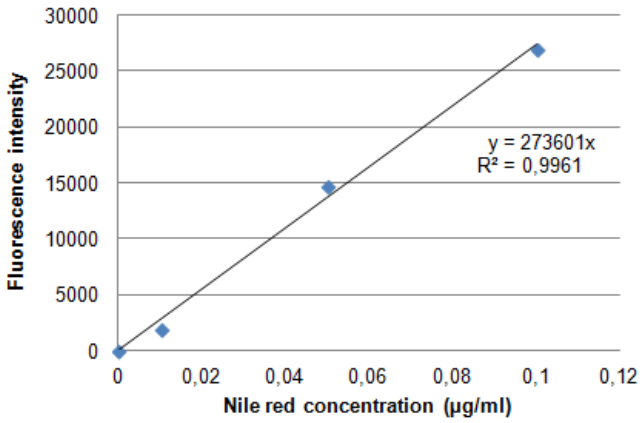

(b) Standard curve for nile red dissolved in THF

Figure D.1: Standard curves of nile red concentration versus fluorescence intensity, obtained in spectrophotometric measurements of nile red dissolved in hexadecane (a) and THF (b).